Virtual liver biopsy for chronic liver disease monitoring by using mpMRI-based radiomic

Jiqing Huang

N°d'ordre NNT : 2023ISAL0078

THESE de DOCTORAT DE L'INSA LYON, membre de l'Université de Lyon

Ecole Doctorale N° ED-205
Ecole doctorale interdisciplinaire science-santé

Spécialité/ discipline de doctorat : Ingénierie biomédicale

Soutenue publiquement le 24/10/2023, par :
Jiqing HUANG

Virtual Liver Biopsy for Chronic Liver Disease Monitoring by Using mpMRI-based Radiomic

Devant le jury composé de :

Lihui, WANG	Professeure	Guizhou University	Rapporteure
Johanne, BEZY-WENDLING	Maitre de Conférences, HDR	Université de Rennes	Rapporteure
Jean-Marie, BONNY	Directeur de Recherche	INRAE	Rapporteur
Antoine, VACAVANT	Professeur	Université Clermont Auvergne	Examinateur
Denis, FRIBOULET	Professeur	INSA-Lyon	Examinateur
Olivier, BEUF	Directeur de Recherche	CNRS	Directeur de thèse
Hélène, RATINEY	Chargée de recherche, HDR	CNRS	Encadrante de thèse
Benjamin, LEPORQ	Chargé de recherche	Inserm	Encadrant de thèse

Département FEDORA – INSA Lyon - Ecoles Doctorales

SIGLE	ECOLE DOCTORALE	NOM ET COORDONNEES DU RESPONSABLE
ED 206 CHIMIE	**CHIMIE DE LYON** https://www.edchimie-lyon.fr Sec. : Renée EL MELHEM Bât. Blaise PASCAL, 3e étage secretariat@edchimie-lyon.fr	**M. Stéphane DANIELE** C2P2-CPE LYON-UMR 5265 Bâtiment F308, BP 2077 43 Boulevard du 11 novembre 1918 69616 Villeurbanne directeur@edchimie-lyon.fr
ED 341 E2M2	**ÉVOLUTION, ÉCOSYSTÈME, MICROBIOLOGIE, MODÉLISATION** http://e2m2.universite-lyon.fr Sec. : Bénédicte LANZA Bât. Atrium, UCB Lyon 1 Tél : 04.72.44.83.62 secretariat.e2m2@univ-lyon1.fr	**Mme Sandrine CHARLES** Université Claude Bernard Lyon 1 UFR Biosciences Bâtiment Mendel 43, boulevard du 11 Novembre 1918 69622 Villeurbanne CEDEX e2m2.codir@listes.univ-lyon1.fr
ED 205 EDISS	**INTERDISCIPLINAIRE SCIENCES-SANTÉ** http://ediss.universite-lyon.fr Sec. : Bénédicte LANZA Bât. Atrium, UCB Lyon 1 Tél : 04.72.44.83.62 secretariat.ediss@univ-lyon1.fr	**Mme Sylvie RICARD-BLUM** Laboratoire ICBMS - UMR 5246 CNRS - Université Lyon 1 Bâtiment Raulin - 2ème étage Nord 43 Boulevard du 11 novembre 1918 69622 Villeurbanne Cedex Tél : +33(0)4 72 44 82 32 sylvie.ricard-blum@univ-lyon1.fr
ED 34 EDML	**MATÉRIAUX DE LYON** http://ed34.universite-lyon.fr Sec. : Yann DE ORDENANA Tél : 04.72.18.62.44 yann.de-ordenana@ec-lyon.fr	**M. Stéphane BENAYOUN** Ecole Centrale de Lyon Laboratoire LTDS 36 avenue Guy de Collongue 69134 Ecully CEDEX Tél : 04.72.18.64.37 stephane.benayoun@ec-lyon.fr
ED 160 EEA	**ÉLECTRONIQUE, ÉLECTROTECHNIQUE, AUTOMATIQUE** https://edeea.universite-lyon.fr Sec. : Philomène TRECOURT Bâtiment Direction INSA Lyon Tél : 04.72.43.71.70 secretariat.edeea@insa-lyon.fr	**M. Philippe DELACHARTRE** INSA LYON Laboratoire CREATIS Bâtiment Blaise Pascal, 7 avenue Jean Capelle 69621 Villeurbanne CEDEX Tél : 04.72.43.88.63 philippe.delachartre@insa-lyon.fr
ED 512 INFOMATHS	**INFORMATIQUE ET MATHÉMATIQUES** http://edinfomaths.universite-lyon.fr Sec. : Renée EL MELHEM Bât. Blaise PASCAL, 3e étage Tél : 04.72.43.80.46 infomaths@univ-lyon1.fr	**M. Hamamache KHEDDOUCI** Université Claude Bernard Lyon 1 Bât. Nautibus 43, Boulevard du 11 novembre 1918 69 622 Villeurbanne Cedex France Tél : 04.72.44.83.69 direction.infomaths@listes.univ-lyon1.fr
ED 162 MEGA	**MÉCANIQUE, ÉNERGÉTIQUE, GÉNIE CIVIL, ACOUSTIQUE** http://edmega.universite-lyon.fr Sec. : Philomène TRECOURT Tél : 04.72.43.71.70 Bâtiment Direction INSA Lyon mega@insa-lyon.fr	**M. Jocelyn BONJOUR** INSA Lyon Laboratoire CETHIL Bâtiment Sadi-Carnot 9, rue de la Physique 69621 Villeurbanne CEDEX jocelyn.bonjour@insa-lyon.fr
ED 483 ScSo	**ScSo**[1] https://edsciencessociales.universite-lyon.fr Sec. : Mélina FAVETON Tél : 04.78.69.77.79 melina.faveton@univ-lyon2.fr	**M. Bruno MILLY** (INSA : J.Y. TOUSSAINT) Univ. Lyon 2 Campus Berges du Rhône 18, quai Claude Bernard 69365 LYON CEDEX 07 Bureau BEL 319 bruno.milly@univ-lyon2.fr

[1] ScSo : Histoire, Géographie, Aménagement, Urbanisme, Archéologie, Science politique, Sociologie, Anthropologie

Virtual Liver Biopsy for Chronic Liver Disease Monitoring by Using mpMRI-based Radiomic

Abstract

Chronic liver disease (CLD) represents a broad spectrum of diseases involving different etiologies. These diseases are characterized by histological features such as inflammation, fibrosis, steatosis, ballooning, or iron overload. Among them, inflammation plays a critical role in the early liver fibrosis process, and fibrosis affects the CLD prognosis and treatment strategy. Although liver biopsy is the gold standard for the diagnosis of CLD, Its invasiveness limits its clinical use. Therefore, an alternative noninvasive, sensitive, and specific remains an unmet medical need.

Magnetic resonance imaging (MRI), especially with diffusion-weighted imaging (DWI) appears currently as an interesting imaging technique to detect CLD-related features. The objective of this thesis is to develop the concept of virtual biopsy to grade inflammation and fibrosis in CLD. To achieve this, the thesis is divided into two parts.

Firstly, using IVIM single sequence study, we studied the standard and advanced DWI's parameters with different fitting approaches and diffusion models, and then the relationship between CLD-related features and DWI parameters was investigated. Significant differences were found between the groups with different degrees of fibrosis. The top four significant differences parameters were selected to build classifiers to characterize fibrosis.

Secondly, from multiple MRI sequences, a radiomics approach involving extraction of several feature combinations from conventional T1w or T2w images as well as proton density fat fraction, T2*, and diffusion parameter maps were investigated. The best combinations were then searched to classify inflammation and fibrosis using random forest.

This study validated the utilization of multiparametric MRI for fibrosis and inflammation severity grading and proposed two effective classifiers for them.

Keywords: Chronic liver disease, Diffusion-weighted Image, Machine Learning, Magnetic Resonance Imaging, Radiomics

Jiqing HUANG

Thèse en traitement de l'image médicale / 2023
Institut national des sciences appliquées de Lyon

Biopsie Virtuelle du Foie pour le Suivi des Maladies Chroniques du Foie à l'aide de la Radiomique Fondée sur l'IRM multiparamétrique

Résumé

Les maladies hépatiques chroniques (CLD) représentent un large spectre de maladies impliquant différentes étiologies. Ces maladies se caractérisent par des aspects histologiques tels que l'inflammation, la fibrose, la stéatose, le ballonnement ou la surcharge en fer. Parmi ces caractéristiques, l'inflammation joue un rôle essentiel dans le processus de fibrose hépatique précoce, et la fibrose affecte le pronostic et la stratégie de traitement de la maladie de Creutzfeldt-Jakob. Bien que la biopsie du foie soit l'examen de référence pour le diagnostic de la CLD, son caractère invasif limite son utilisation clinique. Par conséquent, une alternative non invasive, sensible et spécifique reste un besoin médical non satisfait.

L'imagerie par résonance magnétique (IRM), en particulier l'imagerie pondérée en diffusion (DWI), apparaît actuellement comme une technique d'imagerie intéressante pour détecter les caractéristiques liées à la CLD. L'objectif de cette thèse est de développer le concept de biopsie virtuelle pour évaluer l'inflammation et la fibrose dans la CLD. Pour ce faire, la thèse est divisée en deux parties.

Tout d'abord, en utilisant l'étude IVIM à séquence unique, nous avons étudié les paramètres DWI standard et avancés avec différentes approches d'ajustement et modèles de diffusion, puis la relation entre les caractéristiques liées à la CLD et les paramètres DWI a été étudiée. Des différences significatives ont été trouvées entre les groupes présentant différents degrés de fibrose. Les quatre paramètres les plus significatifs ont été sélectionnés pour construire des classificateurs permettant de caractériser la fibrose.

Deuxièmement, à partir de séquences IRM multiples, une approche radiomique impliquant l'extraction de plusieurs combinaisons de caractéristiques à partir d'images T1w ou T2w conventionnelles ainsi que de cartes de densité de protons, de fraction de graisse, de T2* et de paramètres de diffusion a été étudiée. Les meilleures

combinaisons ont ensuite été recherchées pour classifier l'inflammation et la fibrose à l'aide d'une forêt aléatoire.

Cette étude a validé l'utilisation de l'IRM multiparamétrique pour la classification de la fibrose et de la gravité de l'inflammation et a proposé deux classificateurs efficaces.

Mots-clés : Maladie chronique du foie, Image pondérée en diffusion, Apprentissage automatique, Imagerie par résonance magnétique, Radiomique

Remerciement

This thesis is the result of four years of research work conducted at the Laboratoire de Centre de Recherche en Acquisition et Traitement de l'Image pour la Santé (CREATIS) of Institut National des Sciences Appliquées Lyon (INSA). I would like to express my sincere appreciation to all those who helped me during the thesis.

First and foremost, I would like to express my warmest thanks to my supervisors, Olivier Beuf, Hélène Ratiney, and Benjamin Leporq without whom this thesis would not have been accomplished.

Olivier, with his extensive experience in the field of MRI physics and his efforts, provided invaluable suggestions to enhance the clarity of the manuscript and offered guidance throughout the entire process. Engaging in discussions with him, his humor not only sparked my interest in science but also deepened my knowledge.

Hélène, played a pivotal role, offering help, encouragement, and motivation that alleviated my anxiety and fueled my research passion. In addition, as the project coordinator, she facilitated collaboration with the other two supervisors, ensuring a seamless working relationship. I sincerely thank her for all the confirmation and encouragement.

Benjamin, as an expert in machine learning, not only provided insightful suggestions on clinical aspects of chronic liver disease but also offered valuable expertise on radiomics and MRI applications in detail. His input significantly enriched the depth and breadth of my research. I appreciate these contributions, the time spent and his ideas on this work.

I would also like to express my gratitude to the members of my thesis jury, Prof. Lihui Wang, Prof. Johanne Bezy-Wendling, and Prof. Jean-Marie Bonny, for agreeing to be my thesis rapporteurs. Their guidance and ideas have not only enriched my thesis but have also sparked numerous possibilities for future exploration.

I also want to express thanks to Prof. Denis Friboulet, president of the jury, for his invaluable advice on my research and for presiding over the defense. I would also like to thank Prof. Antoine, VACAVANT as a member of my CST committee and defense jury. He provided valuable oversight during my PH.D.

Jiqing HUANG

My gratitude extends to the China Scholarship Council and INSAVALOR for its financial support during my PhD.

I also want to express thanks to the colleagues and staff in CREATIS. Special thanks go to the Magics and Pilot teams. Many thanks to all the Ph.D. students and friends with whom I had such a great time in Lyon.

最后我要感谢我在中国的家人和朋友们, 感谢他们的关心和支持。

Jiqing Huang

20/11/2023

Contents

Contents of Figures

Contents of Tables

General Introduction

Chronic liver disease (CLD) is a leading cause of morbidity and mortality worldwide, accounting for an estimated two million deaths per year (Roehlen, Crouchet, & Baumert, 2020). CLD is caused by one or more etiology. Historically, viral hepatitis has been the leading etiology for CLD. With the improved prevention strategies and treatments, there have been worldwide decreases in the prevalence of viral hepatitis. Meanwhile, obesity and alcohol consumption trigged a global pandemic in developed countries and regions. It includes a large variety of hepatic diseases that, in most subtypes, damage the liver in similar ways (Sharma & Nagalli, 2022). CLD progression may be characterized by histology with the presence of steatosis, inflammation, fibrosis, and iron overload regardless of the underlying etiologies. In essence, these interrelated factors create a cycle of damage and deterioration in the liver (Chowdhury & Mehta, 2022). Among them, inflammation and fibrosis have emerged as two pivotal factors in that inflammation plays a role in the early liver fibrosis process (Hammoud, 2016; Roehlen et al., 2020), while fibrosis affects the CLD prognosis and treatment strategy. While liver biopsy is a prerequisite to histology, there is still an unmet medical requirement to characterize CLD in a non-invasive way (Nalbantoglu & Brunt, 2014).

In the literature, extensive evidence demonstrated the value of multiple MRI techniques in the assessment of fibrosis or inflammation. Among MRI sequences, diffusion imaging is considered the most promising imaging method for the discrimination of CLD characteristics (Taouli, Ehman, & Reeder, 2009). Fibrosis is the excessive accumulation of extracellular matrix proteins, primarily collagen, in response to tissue injury or inflammation. This leads to tissue scarring and altered tissue microstructure. In fibrotic tissue, the increased density and arrangement of collagen fibers can restrict the diffusion of water molecules. The respective water diffusion is intrinsically linked to the degree of liver fibrosis. Such methods have been investigated extensively in the literature (Besheer et al., 2017; Park et al., 2021; Sandrasegaran et al., 2018). Specifically, CLD patients have lower apparent diffusion coefficient (ADC) values than healthy individuals since the abnormal liver parenchyma increase the liquid

impedance. However, the diagnostic value of ADC in the evaluation of fibrosis remains relatively controversial. Annet *et al.* demonstrated that the lower ADC values in fibrotic livers were caused mostly by perfusion alterations rather than decreased extra-vascular diffusion (Annet et al., 2007). Meanwhile, Yoshimaru *et al.* showed ADC-values were undervalued in cirrhotic tissue and tumors due to the restriction of molecular movement in a high cellularity structure.(Yoshimaru et al., 2019) In consequence, the simple ADC model depicts difficulty in describing such multifactorial mechanisms. Hence, in recent diffusion MRI studies, several advanced diffusion models were proposed to solve this problem, such as intravoxel incoherent motion (IVIM) (Le Bihan et al., 1986), stretched exponential model (SEM) (Bennett et al., 2003) or statistical diffusion model (Stat_D) (Yablonskiy, Bretthorst, & Ackerman, 2003).

Inflamed tissues can have increased cellular density, vascular permeability, and extracellular matrix changes. Taouli *et al.* has shown that lower ADC-values may be caused by inflammatory processes (Taouli et al., 2008). This phenomenon can be explained as the inflammation impact on water diffusion by producing obstacles and impediments to its passage. On the other hand, different forms of inflammation might result in varied diffusion patterns. For example, acute inflammation may increase extracellular fluid and result in higher ADC-values, whereas chronic inflammation with tissue remodeling may limit diffusion due to changed microstructure. In summary, diffusion measures can be influenced by a variety of parameters, including cellularity, cell membrane integrity, extracellular matrix composition, and others. Furthermore, fibrosis and inflammation may occur in the same tissue, making interpretation of diffusion changes more difficult.

In this Ph.D. work, considering the effect of different models and fitting methods on diffusion parameters, we first investigated the relationship between multiple DWI models' parameters and CLD-related features and compared different fitting methods for the estimation of diffusion parameters. However, in recognition of the confounding effects, we, in a second time, and with a radiomic approach, introduced T1-weighted imaging, T2-weighted imaging, and quantitative maps (PDFF and T2*) from chemical shift encoded MRI to classify CLD characteristics.

The part 1 of this thesis is dedicated to present all the foundations necessary for the thesis: the anatomical structure of the liver, insights into Chronic Liver Disease (CLD),

and the diagnostic procedures employed for the detection and evaluation of CLD. It is composed of 3 chapters:

In chapter 1, we introduced the liver structures and chronic liver disease pathology, from the macroscopic to the microscopic scale.

In chapter 2, another non-invasive approach based on the blood tests and liver radiology imaging examination techniques have been presented, with a special focus on the especially the principles of the promising technique the MRI techniques, have been described on which relies this thesis.

In chapter 3, we described diffusion imaging in terms of physic principles, sequences, models, and applications.

The part 2 focuses on presenting my methodological advancements and contributions. This work, makes in-depth use of an MRI acquisition database on CLD patients , collected at Civil Hospital of Lyon (CCP 2013-A00568-39).

In chapter 4, we compared three different fitting methods (nonlinear least square, Segmented nonlinear least square, and Bayesian shrinkage method) for the estimation of diffusion parameters in terms of estimation accuracy and relevance for fibrosis evaluation. Then, the parameters showing significant differences were combined to build classifiers based on several conventional machine learning methods. This study is presented in the form of an article that has been accepted for publication (Huang et al., 2023).

In chapter 5, a radiomic approach is developed to improve CLD patient classification. The proposed method relies on radiomics features extraction from T1-weighted imaging, T2-weighted imaging, and quantitative maps from chemical shift encoded, and diffusion-weighted imaging and then performs classification of the grade of inflammation and fibrosis using random forest classification. This study is presented in the form of an article that was submitted when this manuscript was finalized (Jiqing Huang, Benjamin Leporq, Valérie Hervieu, Sophie Gaillard, Jérôme Dumortier, Olivier Beuf, and Hélène Ratiney. "MRI Virtual Liver Biopsy Using Radiomics Analysis for the Assessment of Chronic Liver Disease, submitted in Journal of Biomedical and Health Informatics).

Part I

Medical and methodological background

Chapter 1 The Clinical background

Contents

1.1. Overview

The liver is one of the essential organs, the center of metabolism in the human body, responsible for material synthesis, glycogen, and fat storage, and digestion through secreting bile. Thus, the liver's health has significant effects on other organ functions and further impacts the quality of human life. Overall, there are approximately 29 million patients in the European Union (E.U.) suffering from chronic liver diseases (Blachier, Leleu, Peck-Radosavljevic, Valla, & Roudot-Thoraval, 2013). Meanwhile, patients are not sensitive to liver pain since the liver does not have any pain receptors (Peng, Hepgul, Higginson, & Gao, 2019). Hence, the screening and monitoring of liver disease are inseparable from the modern medical analysis techniques of histology, imaging, and metabolism examination. This chapter details the hepatic structure, the development of chronic liver diseases, and the criteria for clinical diagnosis.

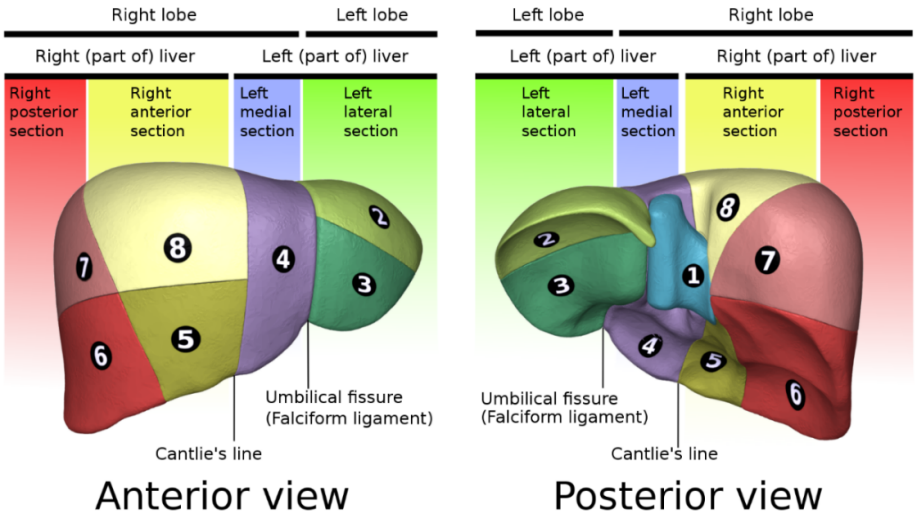

Fig. 1-1 Liver segment classification by Couinaud

https://en.wikipedia.org/wiki/Liver_segment#/media/File:Liver_04_Couinaud_classification.svg

1.2. Liver structure

1.2.1. Anatomic structure

The liver is the largest organ located in the upper right abdomen. Anatomically, the liver can be divided into the right and left lobes. Furthermore, Couinaud classifies the liver into eight hepatic segments (Germain et al., 2014). Each segment has its own independent but equivalent function and complete metabolic system, shown in Fig. 1-1.

There is no significant functional difference between the left and right lobes, even between different segments. The liver lies below the thoracoabdominal diaphragm, and the left lobe edge terminates below the apex of the heart. In consequence, liver imaging is inevitably impacted by the heartbeat and respiration motions.

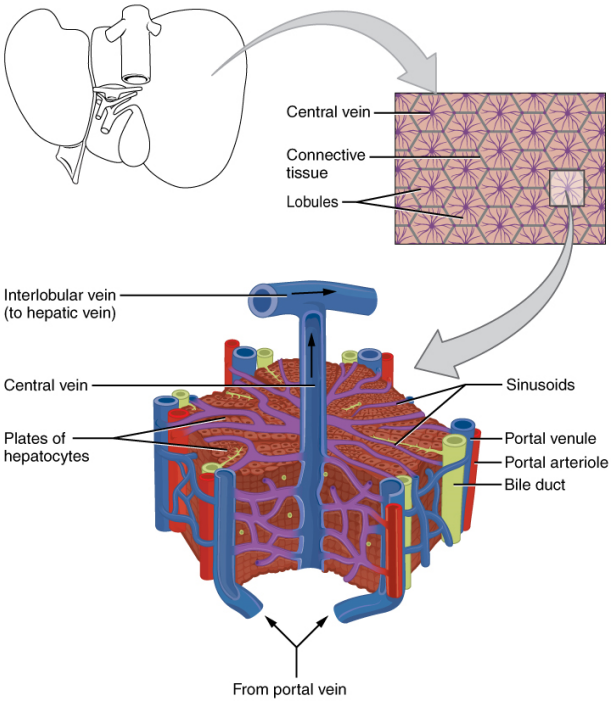

Fig. 1-2 Hepatic lobule structure

https://commons.wikimedia.org/wiki/File:2423_Microscopic_Anatomy_of_Liver.jpg#filelinks

1.2.2. Hepatic lobule

The hepatic lobule is the smallest independent function unit of the liver, as shown in Fig. 1-2. Owing to their physical locations, the hepatic lobules are divided into three microstructures: classical lobule, portal lobule, and acinus. Such tissue structures determine their functions, varying in metabolism, digestion, and transmission, respectively (Greaves, 2012). Abnormal liver parenchyma usually originates from the hepatic lobule destruction and is accompanied by diffusion to surrounding hepatic lobules (King, 2002). Although not every lobule is affected, extensive liver structure changes finally occur due to broad liver invasion and wide destruction spread (from the central vein to the portal area). Therefore， the local injury has the ability to reflect global destruction.

In addition, the hepatic lobule injury triggers the inflammation process, which activates the hepatocyte renewal process. Generally, the hepatic lobule injury causes cellular deficiency and, death, but also cellular propagation, and renovation through cell proliferation and growth. Unfortunately, regeneration has a limitation, so diffuse parenchyma liver disease inevitably happens when the accumulation of lobule damage exceeds the limits of liver regeneration. Meanwhile, the inflammation induces an aberrant healing process. The well-order regeneration sometimes alters into scarring under a toxic liquid environment. Further, the growing fibrosis destroys the hepatic architecture and substitutes the hepatic parenchyma (Bataller & Brenner, 2005). The scarring liver could continue to deteriorate into cirrhosis and hepatocellular carcinoma (HCC).

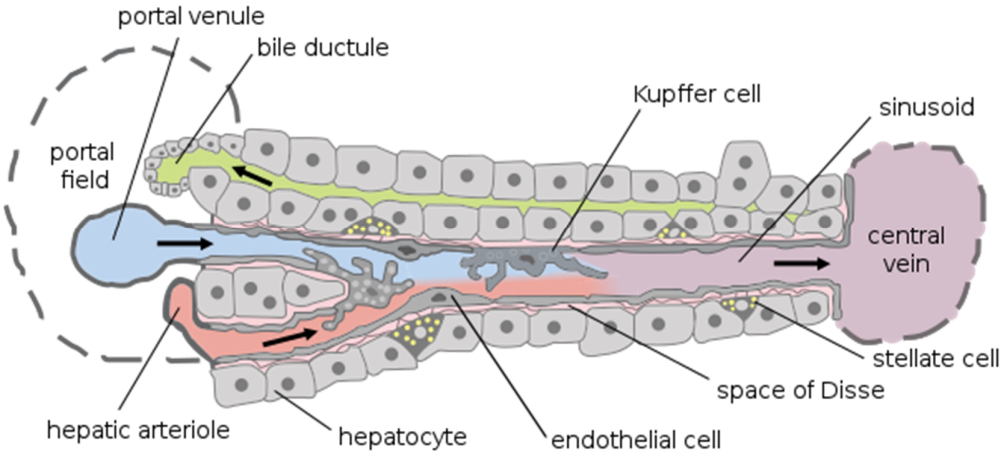

Fig. 1-3 Hepatocytes and their zonation

https://commons.wikimedia.org/wiki/File:Hepatic_structure2.svg

1.2.3. Hepatocytes

Hepatocytes are the smallest functional and structural portion of the liver. These kinds of cells are zoned in three membrane domains. Sinusoidal, lateral, and canalicular, as shown in Fig. 1-3 (Soto-Gutierrez, Gough, Vernetti, Taylor, & Monga, 2017). The cell death pathways are implicated in the pathogenesis of liver-related diseases (Dancygier & Schirmacher, 2010; Shojaie, Iorga, & Dara, 2020). Therefore, it is possible to analyze liver disease by detecting hepatocyte histomorphology changes at the cellular level.

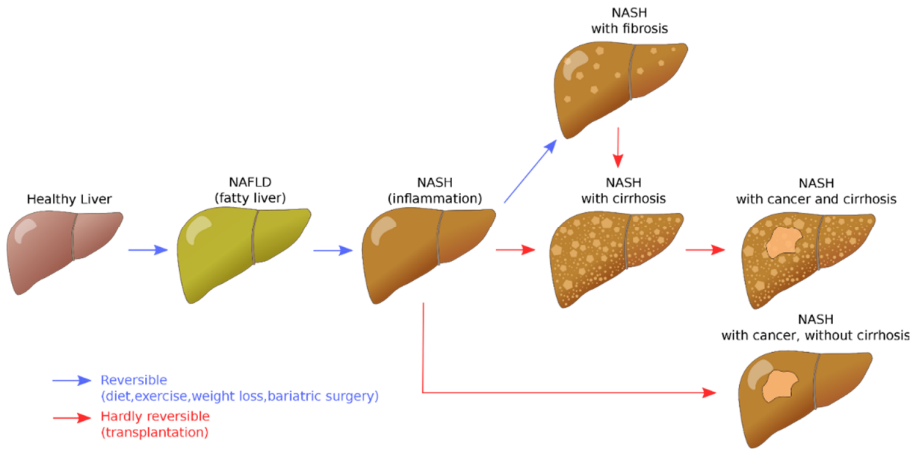

Fig. 1-4 Schematic progression of CLD

https://commons.wikimedia.org/wiki/File:NAFLD_liver_progression.svg

1.3.Chronic liver disease and its progression

Chronic liver disease (CLD) is a large group of hepatic disorders that, in most subtypes, damage the liver in similar ways (Starley, Calcagno, & Harrison, 2010). Etiologically, the CLD is caused by hepatitis virus, fat depots, and further steatosis from mild to severe degrees associated with alcohol or not. Referring to their symptoms, it is sometimes necessary to confirm the grade of the liver disease and then to take the most appropriate treatment (Chalasani et al., 2012). In the following section, we detail the damage related to CLD-related features from macroscopic (tissue and organ) to microscopic (hepatocytes and hepatic lobule).

1.3.1. Chronic liver disease progression

The progression of CLD is shown in Fig. 1-4. Non-alcoholic fatty liver disease (NAFLD) is the most common CLD subtype, with a prevalence ranging between 17 and 46% in western countries. NAFLD refers to overstocked fatty that has little or no inflammation or liver damage. NAFLD includes non-alcoholic fatty liver (NAFL) and non-alcoholic steatohepatitis (NASH). While NAFL has a good prognosis, NASH is associated with poor long-term outcomes (Angulo et al., 2015). The NASH development degrees are related to fibrosis that the inflammation and steatosis may drive. About 20% of NASH patients eventually evolve to cirrhosis or hepatocellular carcinoma, so NASH has become the fastest-growing cause of liver-related morbidity/mortality worldwide (Satapathy & Sanyal, 2015). In HCC patients, almost

80% grow within the cirrhotic liver, remaining 20% major caused by NASH inflammation (Perisetti, Goyal, Yendala, Thandassery, & Giorgakis, 2021). Regardless of the etiology of HCC, the malignant CLD begins with and is highly related to the NAFL/NASH development. In the following section, we will focus on NAFL/NASH as it has become the leading cause of chronic liver disease and constitutes a major public health concern.

1.3.2. Chronic liver disease progression at the macroscopic scale

NAFL is defined as the accumulation of liver fat that exceeds 5% to 10% of the liver's weight. NAFL is always associated with metabolic syndrome, including central obesity, diabetes mellitus, raised blood pressure, increased triglyceride levels, insulin resistance, and decreased high-density lipoprotein-cholesterol (Alberti, 2009). However, NAFL usually does not cause any liver damage. At the macroscopic scale, NAFL can be detected with the symptom of hepatomegaly in imaging examination and platelet-related parameters changes (platelet count increase and mean platelet volume decrease), with or without increasing liver enzymes in serum testing. However, these biomarkers are not enough specific to distinguish between NAFL and other hepatic diseases. Advanced CLD from NASH to HCC ranges from inflammation to steatosis and further fibrosis. On the macroscopic level, advanced CLD is associated with hepatomegaly, liver scarring, and atrophy with spleen enlargement. In general, CLD may change some metabolite levels, such as increase of enzymes leaked from the cell [serum glutamyl transferase, aka aspartate transaminase (AST) and alanine aminotransferase (ALT)], liver-derived plasma proteins decrease due to liver dysfunction (mainly albumin), and further increase or decrease of materials and products in metabolic reactions catalyzed or inhibited by hepatic synthetics.

Unfortunately, such anatomy and metabolic changes lack sensitivity and specificity to distinguish between fat-related, alcoholic, or virus-driven hepatic diseases (Ibrahim, Singh, Ganie, & Alsayari, 2009). Therefore, radiologists expect medical imaging to provide focal and clear insight to improve diagnosis and to be more specific.

1.3.3. Chronic liver disease progression at the microscopic scales

Hepatocyte damage is the smallest quantitative change that portends severe liver disorders. To completely understand the mechanism of CLD development, it requires discussing abnormal liver parenchyma at the cellular level. In brief, the fatty liver with

inflammation is toxic to hepatocytes and causes mitochondrial damage, which leads the NAFL to deteriorate to NASH, which brings steatosis and fibrosis and further to cirrhosis and HCC. Moreover, there is increasing evidence that CLD progression is highly correlated with hepatocyte death (Shojaie et al., 2020). The programmed hepatocyte death is mainly related to apoptosis, necroptosis, pyroptosis, and ferroptosis. Besides, it has been proven that apoptosis is the primary pattern that drives inflammation in NASH. A handful of studies show that the deactivation of apoptosis helps improve AST or ALT, resulting in lower liver inflammation and fibrosis (Caballero et al., 2010; Gautheron et al., 2014; Witek et al., 2009). Despite growing evidence being demonstrated in mice experiments progress, such results are difficult to reproduce in humans. Recent experiments showed a little progress that suppressing ALT levels and apoptosis helps to prevent the formation of fibrosis (Garcia-Tsao et al., 2020), but also the opposite result in another research (Harrison et al., 2020). The researchers explained that the hepatocyte chooses another death program when the apoptosis is suppressed. These phenomena are also found in mice experiments (Zhao et al., 2020). In other words, the complex human hepatocyte death mechanism makes it difficult to analyze the severity of CLD only using the level of cell metabolites. In histomorphology, the process of hepatocyte death may express the CLD progression. Under lipid and fatty acid metabolism change, hepatocytes die from stress. The hepatic lobule disorders appear with widespread intercellular hepatocyte death. Then, the hepatocytes' death triggers inflammation. During steatosis, the lipotoxicity may activate hepatic stellate cells that promote the fibrogenic phenotype and fibrosis (Herbert Tilg & Moschen, 2010). Under the synergistic effect of inflammation and steatosis even fibrosis, the hepatocytes are dysplastic, and then nodules appear, which indicates that the HCC is beginning (Schlageter, Terracciano, D'Angelo, & Sorrentino, 2014).

Previous studies also pointed out that necroptosis, pyroptosis, and ferroptosis have a direct or potential relationship to ballooning, fibrosis, or iron overload, respectively (Gaul et al., 2021; Schwabe & Luedde, 2018; Yu & Wang, 2021). The relationship between liver injury and hepatocyte death is shown in Fig. 1-5.

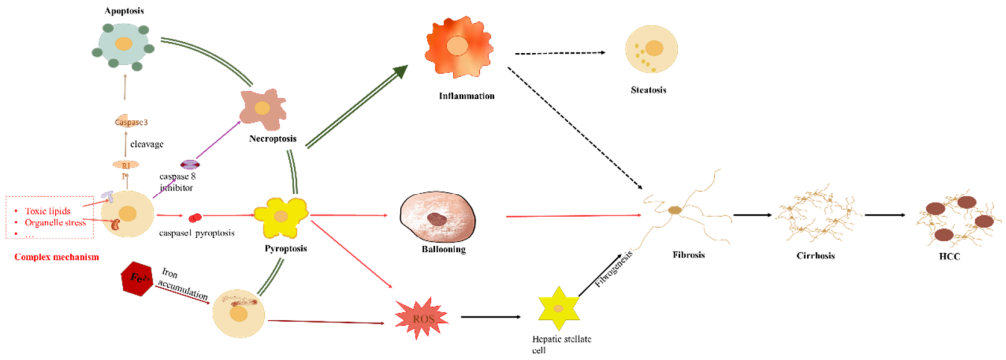

Fig. 1-5 NAFLD deterioration at microscopic scales

1.4. Liver biopsy — the reference for CLD diagnosis

1.4.1. Histological analysis

Liver biopsy is a procedure aiming to insert a biopsy needle and remove a small tissue from the liver to test liver tissue conditions. There are three puncture approaches, percutaneous, laparoscopic, and transvenous (Neuberger et al., 2020). The most common method is the percutaneous liver biopsy for which the biopsy needle is usually put slightly below the bottom right rib cage except for hepatic ectopia or hepatic cirrhosis. To extract the sample from the liver, the biopsy is usually assisted by ultrasound. After the staining procedure, the examiner analyzes the CLD-related histological features under electron microscopy. Compared to NAFL, NASH is characterized by steatosis, hepatocyte ballooning, inflammatory infiltrates, with or without fibrosis at histology. With the fibrosis increasing, cirrhosis occurs as some hepatocyte islands by fiber surrounding. For the last stage of CLD, there are various subtypes of HCC. Generally, almost all hepatocytes lose the typical hepatic architecture, and multiple spots of different sizes can be found. The comparison among the varying CLD conditions from histology is shown in Fig. 1-6. For diagnosis of NAFLD, and further distinction of advanced CLD level, the current classification scheme takes into account the following factors as shown in Fig. 1-7.

Inflammation

Inflammation marks the beginning of NASH, which contributes to the long-last liver injury. At histology, inflammation is defined as arising from lobular and portal injury. Experienced pathologists can distinguish liver inflammation's causes and

Thèse en traitement de l'image médicale / 2023
Institut national des sciences appliquées de Lyon

varying from cell distribution and morphology change, cell structural destruction (Nalbantoglu & Brunt, 2014).

Ballooning

Ballooning is defined as hepatocyte enlargement 1.5-2 times than the normal hepatocyte diameter. The ballooning number can be counted. Hepatocyte ballooning responding to necroptosis has been proved to be linked to the formation of fibrosis (Grootjans, Vanden Berghe, & Vandenabeele, 2017). Ballooning is an important NASH biomarker used as a major differential indicator in early diagnostic classification systems (Caldwell et al., 2010). Even now, ballooning is a component of multiple NASH grading systems including Brunt criteria (cf below), the NAFLD activity score (NAS), steatosis.activity.fibrosis score (S.A.F score), etc.…

Steatosis

Steatosis is the fatty depot within hepatocytes that the fatty hepatocytes exceed 5% of total hepatocytes. Such pathology features are associated with high-calorie and high-cholesterol diets and insulin resistance (Nassir, Rector, Hammoud, & Ibdah, 2015). In early or mild steatosis, the effect can be reversible through diet control and health management. To visualize lipid droplets, hematoxylin and eosin, Red O staining, etc... are used to staining. The percentage of steatosis is estimated by the number of hepatocytes with fat droplets divided by the total number of hepatocytes.

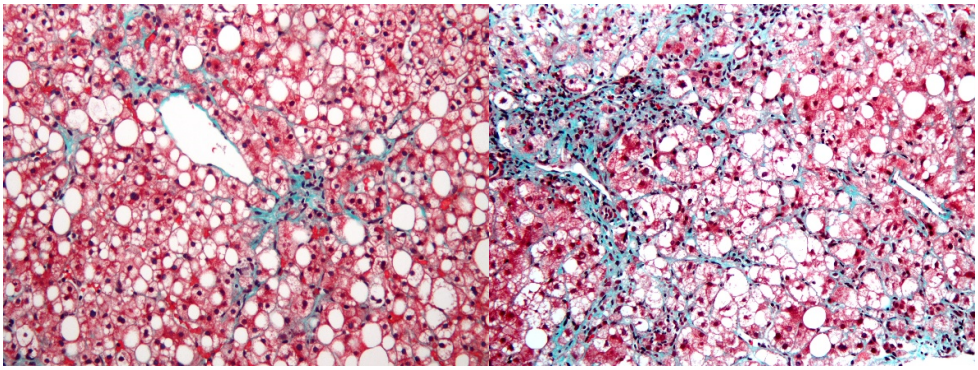

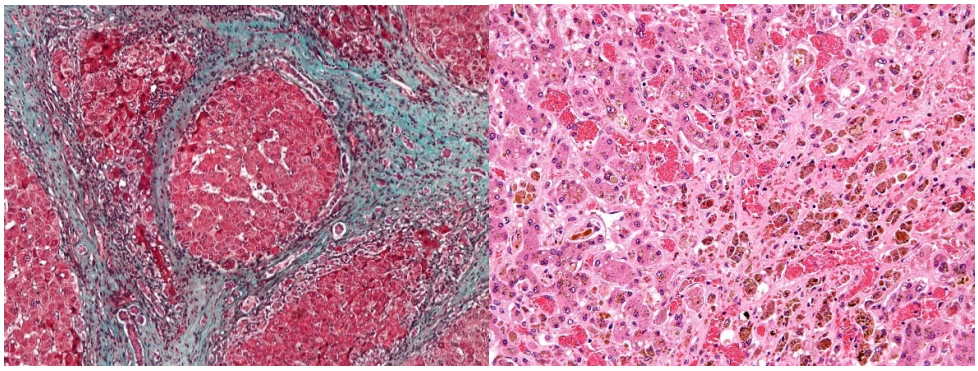

Fig. 1-6 Tissue sample for CLD conditions (top-left: NAFL top-right: NASH Bottom-left: cirrhosis bottom-right: HCC)

https://commons.wikimedia.org/wiki/File:Non-alcoholic_fatty_liver_disease1.jpg
https://commons.wikimedia.org/wiki/File:Periportal_hepatosteatosis_intermed_mag.jpg
https://radiopaedia.org/cases/cirrhosis-histology-2
https://commons.wikimedia.org/wiki/File:Fibrolamellar_hepatocellular_carcinoma_-2-_very_high_mag.jpg

Iron-overload

The iron overload is related to hepatocytes ferroptosis. In human studies, the mechanism of iron death is complex and still being explored and discovered in relation to NASH. However, more and more evidence supports that iron overload correlates with several CLD conditions, especially fibrosis (Chen, Zhu, Zang, & Zhai, 2021). In histology, iron overload within the hepatocytes can be found through the Perls-Prussian blue staining. Iron overload is manifested by the presence of small particles within reticuloendothelial cells as well as granules within the hepatocytes.

Fibrosis

Fibrosis is the most crucial feature to be evaluated since it relates to the NASH prognosis and drives the treatment strategy. Although fibrosis is not the essential feature for diagnosing NAFLD, it marks the beginning of cirrhosis. Chronic inflammation induces hepatic stellate cells' fibrogenesis and the proteins (mostly collagen) depot at the extracellular level. The fibrosis occurs in the portal tracts and extends to adjacent portal tracts and hepatic venules (Lo & Kim, 2017). Cirrhosis is the end-stage of fibrosis in which the intertwined fibrosis suppresses the metabolic exchanges (Schuppan & Afdhal, 2008).

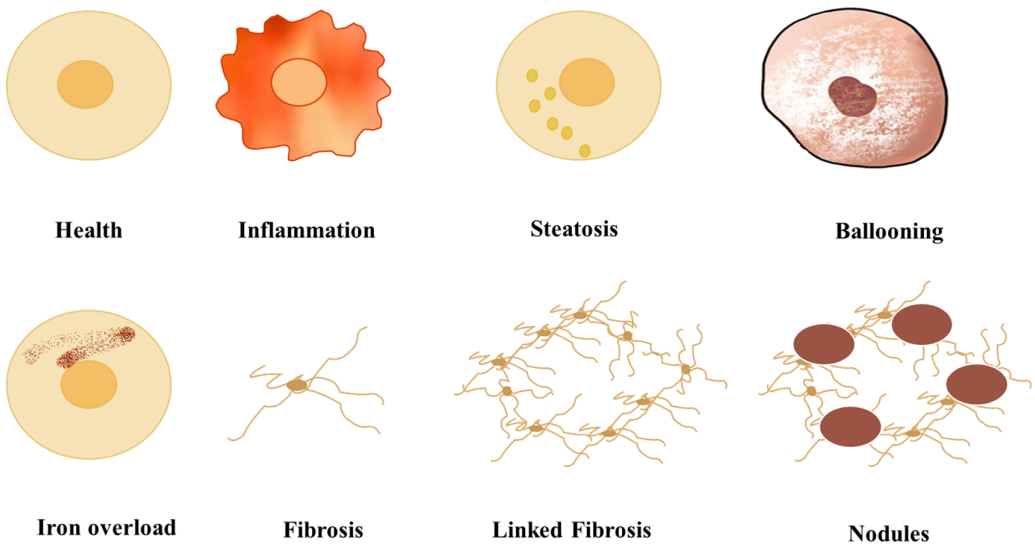

Fig. 1-7 Chronic liver disease-related characters

Nodules

HCC almost always occurs in case of hepatic impairment. The classical theory demonstrates that inflammation is an important factor driving cancer progression (Hanahan & Weinberg, 2011). Recently studies suggest cirrhosis is often the preface to the HCC, which is correlated with the regenerating nodules. The benign nodules develop into dysplastic nodules and final form as tumors accompanied by fibrosis depots (Paradis & Beaufrère, 2022). Referring to the size of the nodules, the hepatocyte's differentiated levels, and nodular type, the HCC can be distinguished from early to advanced HCC (Schlageter et al., 2014).

1.4.2. Grading system

This section does not present the assessment index for cirrhosis and HCC, since NAFL/NASH separation is still the core issue in clinical. Based on the above background information, one can retain that (1) NAFL is easily reversible (through diet control and exercise), (2) the inflammation by NASH leads to the CLD deterioration procession, and (3) fibrosis is the accelerator of CLD procession. Therefore, we highlight the adult NAFLD scoring systems and fibrosis scoring systems in this section.

It is also worth noting that almost all biomarkers in histology are qualitative indicators. It is why a series of grading systems have been proposed and developed by pathologists to decrease the subjectivity of histology analysis with strong inter and

intra-observer reliability and to provide uniform and accurate determined information for diagnosis and prognosis.

To classify NAFLD into NASH and NAFL, NASH Clinical Research Network (NASH CRN), steatosis+fibrosis+activity (SFA), and Brunt system are three common assessments responding to steatosis, lobular or portal inflammation, ballooning degeneration, with or without fibrosis. Additionally, the Brunt scoring system is the most widely used in clinical because it considers the hepatic fibrosis effect.

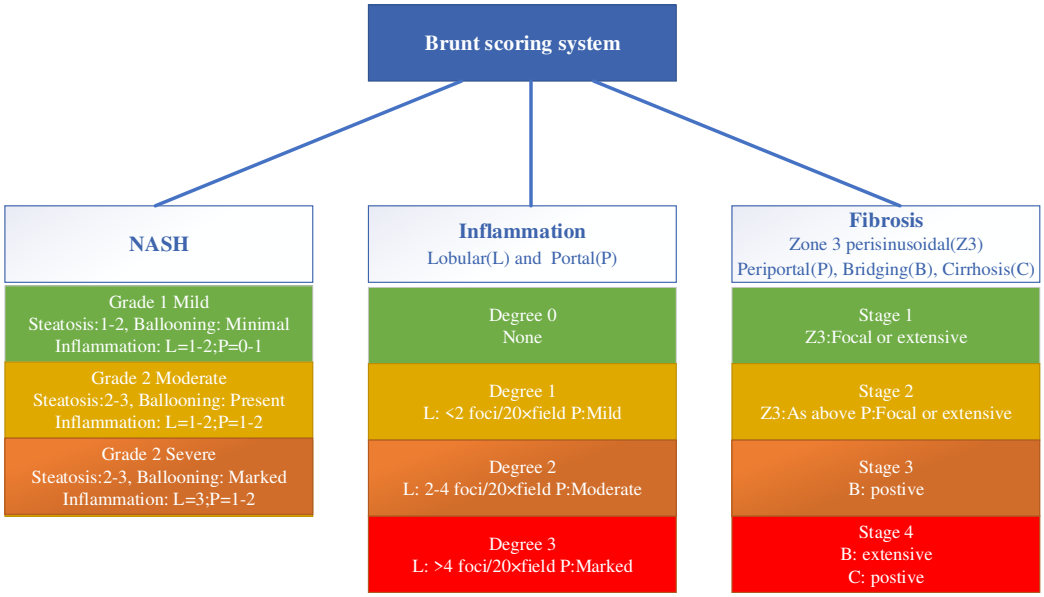

Fig. 1-8 Brunt scoring system

Unfortunately, fibrosis pattern diversity is constrained by the Brunt system, because it only quantifies fibrosis into four levels. For further refinement of hepatic fibrosis, the cheuer system, the Batts-Ludwig system, the Ishak system, and the METAVIR system are proposed (Lo & Kim, 2017). Compared to other fibrosis systems, Ishak provides more continuous changes from one stage. to the next. Therefore, Ishak is widely used in clinics (Everhart et al., 2010). Fig. 1-8 and Fig. 1-9 give the details of the Brunt scoring system and Ishak Fibrosis and METAVIR scoring system. Among them, the brunt scoring system and Ishak Fibrosis scoring will be used in this thesis as the ground truth.

1.4.3. Risk and limitation

Biopsy is recommended because it is helpful in distinguishing coexisting disorders, investigating the unknown etiology, tracing focal lesions, confirming special diseases

and etc… whatever is in diagnosis, prognosis, and therapeutic management decisions (Polson & Lee, 2005). However, patients are often anxious about this procedure. It is not reasonless because liver biopsy is associated with inherent morbidities, like pain, bleeding, organ perforation, and sepsis. To overcome the biopsy insertion problem, real-time guidances (CT, US) are helpful for avoiding cystic, solid, or vascular. Nevertheless, it is still a diagnostic dilemma that biopsy also has multiple potential complications (including up to 84% pain, bleeding, gall bladder puncture, Renal failure, and death). Thus, the biopsy is not suitable for large population systematic screening (i.e. 40% of the world population could be eligible due to the increase of overweight incidence). Although biopsy is the gold standard for diagnosis of NAFL/NASH, there is an unmet requirement in non-invasive methods for clinical practice. Meanwhile, the sampling variable and pathologists' subjectivity also limit the accuracy of histological evaluation. It still needs attention to obtain sufficient tissue at minimum injury and establish a more objective scoring system.

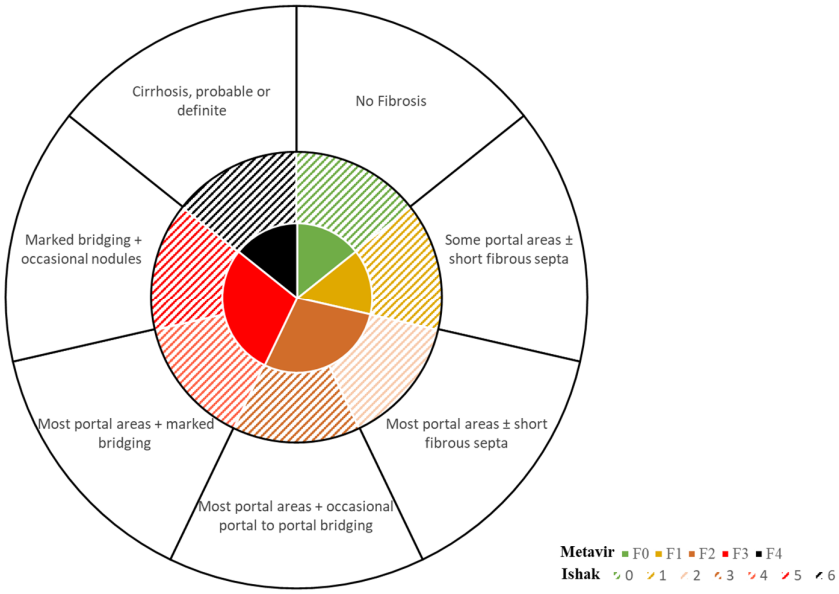

Fig. 1-9 Ishak Fibrosis scoring system

1.5. Conclusion

This chapter introduced the liver structures and chronic liver disease pathology, especially for NAFLD, from the macroscopic to the microscopic scale. The microscopic disorder is directly related to hepatocyte death and can be detected and analyzed in liver

biopsy. Due to the injury that could cause biopsy, it is still required to characterize chronic liver diseases in a noninvasive way.

Chapter 2 Noninvasive diagnostic modalities

Contents

2.1. Introduction

As discussed in Chapter 1, liver biopsy is the gold standard for the diagnostic and staging of CLD but its invasiveness limits its repeated clinical use. In the past decades, clinicians and pathologists have been committed to find alternative noninvasive methods for evaluating CLD. Such techniques have achieved excellent diagnostic implications to a certain extent but sometimes are still absent of specificity and sensitivity. Several techniques were proposed to solve this issue in clinical routine and in cutting-edge scientific research.

2.2.Blood test

The blood test is a lab analysis to track human overall physical well-being quickly. The common biomarkers are listed in Table 2-1 (a). Generally, these biomarkers reflect the body's global metabolic level to help check liver functioning. Some biomarkers at abnormal levels may indicate problems with liver function but is difficult to ensure the type of disease. Possible reasons are: (1) some biomarkers not only correlate with the liver state but also with other organs; (2) a variety of metabolic mechanisms exist in the human body.

Table 2-1 Blood test

(a) Common biomarkers

Function	Biomarkers	Type of evaluation
metabolism	a. Albumin	liver condition
	b. Bilirubin	Obstruction of bile flow
		The problem of processing bile
	c. Cholesterol	Diet
	d. Glucose	Diet
	e. Triglycerides	Diet
	f. Plate count	Inflammation or infection
	g. prothrombin time	Activity
Liver enzymes	h. 5'-nucleotidase	Cholestasis
	i. Alanine transaminase	Acute hepatocyte damage
	j. Alkaline phosphatase	Liver activity and obstruction
	k. Aminotransferases	Hepatocyte lesion
	l. Aspartate transaminase	Liver activity
	m. Gamma-glutamyl transpeptidase	Liver function and alcohol ingestion
	n. Lactic dehydrogenase	Widely cell damage
	o. Haptoglobin	Yellow tinge
Etiology	p. Alpha-1 antitrypsin	Fibrosis and cirrhosis
	q. Alpha-2-Macroglobulin	Fibrosis and cirrhosis
	r. Alpha-fetoprotein	Tumor
	s. Apolipoprotein A1	Cholestatic liver disease

	t. Mitochondrial antibodies	Fibrosis and cirrhosis
External	u. Age	-
	v. Body mass index (BMI)	-
	w. Diabetes	-
	x. Gender	-
	y. Waist circumference	-

(b) Blood test indicators

Function	Name of test	Biomarkers	Limitation
Fatty and steatosis	Fatty Liver Index (Bedogni et al., 2006)	e, m, v, w	Not accurate; correlated with insulin resistance; confounded with fibrosis and inflammation (Fedchuk et al., 2014)
	SteatoTest (Poynard et al., 2005)	a, c, d, e, i, m, q, s, o, u, v, x	Underestimated; BMI significant variability; Bilirubin induce false positive (Poynard et al., 2019)
	Hepatic Steatosis Index (Lee et al., 2010)	i, l, w, x	Not accurate; correlated with insulin resistance; confounded with fibrosis and inflammation (Fedchuk et al., 2014)
Inflammation	ActiTest® (Bedossa & Poynard, 1996)	Unknown	Oversensitive [initial designed for CHC and CHB] (Poynard et al., 2019)
NASH	NashTest, NashTest-2	Unknown	Low precision (Poynard et al., 2019)
	NIS4®	miR34a-5p, α2 macroglobulin, YKL-4, HbA1c	Multi-platform analysis of 4 different biomarkers
	NIS2+®	miR-34a-5p and YKL-40	Not validated outside dataset and Age robustness
Fibrosis	NAFLD Fibrosis score (Angulo et al., 2007)	a, i, l, f, u, v, w	Less accurate in identifying intermediate stages of fibrosis (Montaño-Loza, 2022)
	Fibrosis-4 (Sterling et al., 2006)	i, l, f, u	
	APRI (Lok et al., 2009)	l, f	Not useful tools in early stage of fibrosis (Abd El Rihim et al., 2013)
	BARD (Harrison, Oliver, Arnold, Gogia, & Neuschwander-Tetri, 2008)	j, l, v, w	Not useful in identifying severe fibrosis (Ruffillo et al., 2011)
	FibroSURE	b, i, m, o, q, s, u, x	Not useful in identifying severe fibrosis and cirrhosis (Salkic, Jovanovic, Hauser, & Brcic, 2014)
Alcoholic	Glasgow Alcoholic Hepatitis Score (Forrest et al., 2007)	b, g, u + white cell count, blood urea	Lacked specificity (H Tilg & Kaser, 2005)
	ABIC Score for Alcoholic Hepatitis	b, g, u+ creatine	Not consistent with mortality (Dominguez et al., 2008)
Insulin resistance	Homa IR Homa 2	d+ Insulin	Insulin sensitivity (Bugianesi, McCullough, & Marchesini, 2005)

To cope with these problems, clinicians and researcher proposed several indicators for different CLD, as shown in Table 2-1 (b). In clinical routine, the blood test and

further blood test indicators are recommended for large-scale screening and preliminary diagnosis because it is readily available at a low cost. Meanwhile, the difficulty in assessing qualitative indicators that rely on a specialist's expertise and experience, statistical bias due to sampling and formula, and complex etiologies are the limitations of blood tests.

2.3. Radiologic modalities

To date, conventional medical imaging is not used to confirm or diagnose CLD. Stade 2 and more steatosis (> 30%) can be detected at conventional b-mode US (Hirooka et al., 2022). And conventional MRI is only used for the screening of HCC in cirrhosis histologically-proven patients (F4 METAVIR). Compared to liver biopsy, medical imaging has shown substantial advantages, including being non-invasive, showing more minor sampling error by evaluating directly the liver parenchyma, and exhibiting less variability with both qualitative and quantitative protocols (Q. Li, Dhyani, Grajo, Sirlin, & Samir, 2018), listed in Table 2-2.

Table 2-2 Medical imaging techniques and modalities

Techniques	Modalities	Information	Limitation
US (Gerstenmaier & Gibson, 2014; Piscaglia et al., 2014)	Conventional B-mode	Steatosis, Cirrhosis	Acceptable sensitivities Reproducibility problem
	Doppler	Hepatic blood flow	Complex mechanisms
	Elastography [transient elastography FibroScan [imaging-based]	Fibrosis	Required to avoid bias within different techniques, manufacturers, and operators
CT	Conventional	Liver and biliary tract structure Infection Fatty and steatosis	Radiation exposure Lack of sensitivity to tiny lesions Confounded by deposition of other materials (iron, copper, glycogen, and amiodarone)
	Dual-energy spectral CT	Quantification of fat iron and iodine	Radiation exposure No significant improvement
NMR	Conventional anatomical imaging	Structure and morphology	Radiation exposure Difficult to determine the etiology sources

Diffusion	Water molecular motion	Technical limitation (conflicting results)
Perfusion	Blood volume and blood floor	Need contrast agent
Proton density fat fraction	Fat depots and steatosis	Confounding effect of iron (Tang et al., 2013)
Susceptibility weighted imaging	Iron overload and fibrosis	
Quantitative susceptibility mapping	Iron overload and fibrosis	-
Spectroscopy		Time-consuming and limited to one voxel (Vernuccio et al., 2021)
Elastography	Stiffness	Poor image resolution (Manduca et al., 2021)

2.3.1. Ultrasound (US)

US is the most prevalent qualitative radiology examination for CLD. Conventional B-mode US is still the effective and economical fast assessment tool providing valuable information on liver parenchyma and liver lesions (Gerstenmaier & Gibson, 2014). However, US-based transient elastography methods such as Fibroscan are used in clinical routine to confirm or diagnose fibrosis and refunded by French welfare system. In addition, the controlled attenuation parameters (CAP) function in the Fibroscan is able to provide also quantitative information about steatosis grade. To separate the effect between fibrosis and steatosis, the development of the US elastography received widespread attention because of its potential ability to stage liver fibrosis. It can be expected that elastography will be a good choice after more evidence and validation (Gerstenmaier & Gibson, 2014). Nevertheless, it is not a slice imaging technique (do not image the whole liver).

2.3.2. Computer tomography (CT)

It has been proven that CT is valuable for screening of HCC , but not effective enough for condition explain the CLD characteristics (Alberti, 2009; Elbanna, Mansoori, Mileto, Rogalla, & S Guimarães, 2020). In general, injected CT can replace MRI in case of is MRI contra-indication. The major problem is that conventional CT is difficult to differentiate the fatty effect, and even dual-energy CT could not improve the division result (Artz et al., 2012; Mendler et al., 1998). To date, the advanced

technique, spectral CT, is still stuck in the CT's traditional application to cirrhosis and hepatocellular carcinoma (Laroia et al., 2021; Lv, Lin, Gao, & Chen, 2012). Therefore, the development of new contrast agents is still awaited to expand the spectral CT diagnostic power (Yeh et al., 2017).

2.3.3. Magnetic resonance

Nuclear Magnetic Resonance (NMR) is the most promising imaging technique to evaluate CLD conditions comprehensively. Several protocols can diagnose various CLD features that differ in structure, stiffness, hemodynamics, and metabolism. Magnetic resonance elastography (MRE) outperforms. Fibroscan due to its assessment of a significantly larger volume through three-dimensional displacement analysis. Magnetic resonance spectroscopy (MRS) and proton density fat fraction (PDFF) are consider as a gold standard replacing the biopsy for the steatosis and fatty depots assessment.(Caussy et al., 2018; Springer, Machann, Claussen, Schick, & Schwenzer, 2010). Diffusion-weighted imaging (DWI) and iron susceptibility-based imaging including T2 or T2* mapping demonstrated potential in assessing fibrosis and iron overload (Taouli et al., 2007; Yoshikawa et al., 2021). Although MRI is the most promising imaging technique in CLD diagnosis, there remain unresolved issues that we will explain in detail in the next section.

2.4. Nuclear magnetic resonance

The abundance of information provided by NMR, not to mention the simultaneous high spatial resolution, high intrinsic contrast, and large field of view, has trigged wide scholarly attention on NMR application for diagnosing CLD. However, the long acquisition time, complexity of interpretation, availability of MR systems, and cost may limit accessibility. In addition, integrating diverse information requires clinicians to have professional knowledge of multi-parametric NMR, which brings a tremendous challenge for clinical application. For that matter, understanding the NMR diagnostic function requires great knowledge, understanding of the NMR principles, and learning new techniques, including aspects of NMR hardware and software.

In this section, we attempt to introduce the basic concept involved in NMR and make clear how it works. The fundamental elements of an NMR experiment are:

longitudinal macroscopic magnetization, radiofrequency (RF) excitation, space encoding, and signal reconstruction.

2.4.1. Magnetic resonance

MRI exploits the magnetic properties of some particular nuclei. The hydrogen (^{1}H or proton) is the most common and abundant nucleus present in biological tissue and thus used in MR imaging.

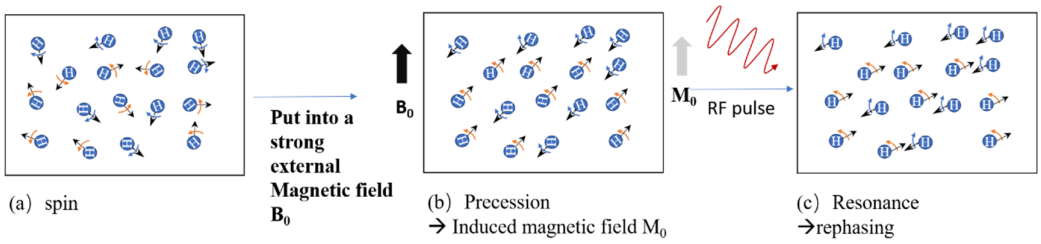

Fig. 2-1 precession and resonance of protons

Nuclear Magnetic moment and precession

As shown in Fig. 2-1 (a), ^{1}H has a non-zero spin quantum number (half integer) which gives it a nuclear magnetic moment μ. By itself, normally, these moments take random orientation, and thus present magnetic forces neutral from the overall perspective. When a strong external magnetic B_0 field is applied (Fig. 2-1 (b)) the magnetic moments of a large number of nuclei are aligned along B_0 and create a macroscopic magnetization M_0. Unfortunately, this magnetization cannot be straight detected because it is very small compared to the external magnetic field B_0. From the interaction of the magnetic moment with the external magnetic field results a precession movement. Rather than settle down on the direction of the external field direction, the magnetic moment precesse as a rotating spinning top ensemble. Being able to treat the behavior of an ensemble of magnetic moments in terms of macroscopic magnetization allows a transfer from a quantum mechanical to a classical description of NMR, which simplifies the picture of the NMR experiment.

RF pulse excitation

The equilibrium of the macroscopic magnetization M_0 is disturbed by moving it away from its position with a radiofrequency magnetic field B_1: this the RF pulse excitation.

This RF pulse must be applied at the resonance frequency of the spin system, the Larmor frequency, in order to achieve this perturbation. The Larmor pulsation or angular frequency is given by:

$$f=\frac{\gamma B_0}{2\pi} \tag{2-1}$$

Where B_0 is the strength of the magnetic field and γ the gyromagnetic ratio of ^1H. In a general and simplified way, the evolution of the macroscopic magnetization M in the presence of a magnetic field B is given by the phenomenological equations of Bloch.

For the sake of clarity, the macroscopic magnetization can be decomposed into longitudinal components $M_{||}$ and rotating transverse components $\vec{M}_{\perp}$. The RF field will momentarily tilt the magnetization in the plane transverse to B_0 (the tilt will be characterized by a tilt angle). After tilting, the movement of precession of all the magnetic moments in phase results in a transversal magnetization $\vec{M}_{\perp}$ which rotates in x-y plane. After the RF pulse switches off, the magnetization gradually returns to its initial state- so that the gradually vanishing $\vec{M}_{\perp}$ can be detected and measured.

2.4.2. Signal detection

MR signal detection is a reverse process to signal generation, referring to Faraday's law of electromagnetic induction. Specifically, the rotating transversal magnetic sweeps create an electromotive force by crossing the receiver loop coil in the transverse plane. The time-dependent transversal magnetization transformed into the time-varying current signal, so-called free induction decay (FID). Physically, the decay rate of FID signal is related to the relaxation process that is described below.

Relaxation

As we discussed, after excitation, the transverse magnetization flips to the original longitudinal magnetization. As opposed to excitation, the magnetization regrows at the z-axis, called spin-lattice relaxation (T_1-relaxation). Independently, the x-y magnetization at the beginning evolves to 0 at the end. The protons are dephasing, thus the x-y magnetization decreases with constant time, called spin-spin relaxation(T2-relaxation). The magnetization recovers in the z-axis and decays in the x-y plane, as described by the Bloch equation, see

Fig. 2-2. The receiver coil can only detect the changing of magnetization on the x-y plane. In real applications, the FID signal decay is faster than T2-relaxation. Indeed,

field inhomogeneities contribute to accelerating the FID decay, which is characterized by T_2^*-relaxation. Hence various sequences were designed to weigh or carry different tissue information playing on T1, T2, and T2*.

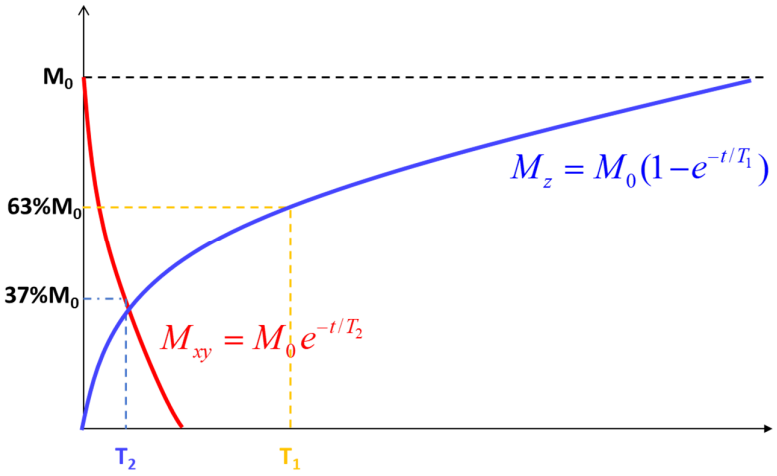

Fig. 2-2 evolvement of magnetization for longitudinal regrowth and transverse decay

2.4.3. From signal to image

MRI is a tomographic technique. Although the magnetization can be detected, all protons are excited together and contribute to the MRI signal. To locate the proton, gradient encoding, including slice selection, phase encoding, and frequency encoding, are sequentially performed, as shown in Fig. 2-3. To assist the explanation, we assume the slice selection, phase encoding, and frequency encoding are applied in the z, y, and x-axes.

Slice selection

The slice selection is performed with linear variation of z component of magnetic field with z, in the same time as a RF pulse as shown in Fig. 2-3 (b). While the gradient magnetic field created by the z magnetic coil is on, the resonance condition for each proton -Larmor frequency- varies linearly along the z-direction. Thus far, the on-resonance protons during the RF pulse application will select a slice with a certain thickness.

Phase encoding

After the slice selection, the transverse magnetization from each voxel is in-phase within a slice (a rephasing gradient is often used to meet this requirement). The y-axis gradient turns on quickly, altering the magnetization precession rate. The magnetization rotates at different angular velocities along y and accumulates its own unique phase, as shown in Fig. 2-3 (c). Once the phase encoding gradient has been turned off, the magnetization phase shifts are kept along the direction y while the frequency recovers to Larmor frequency.

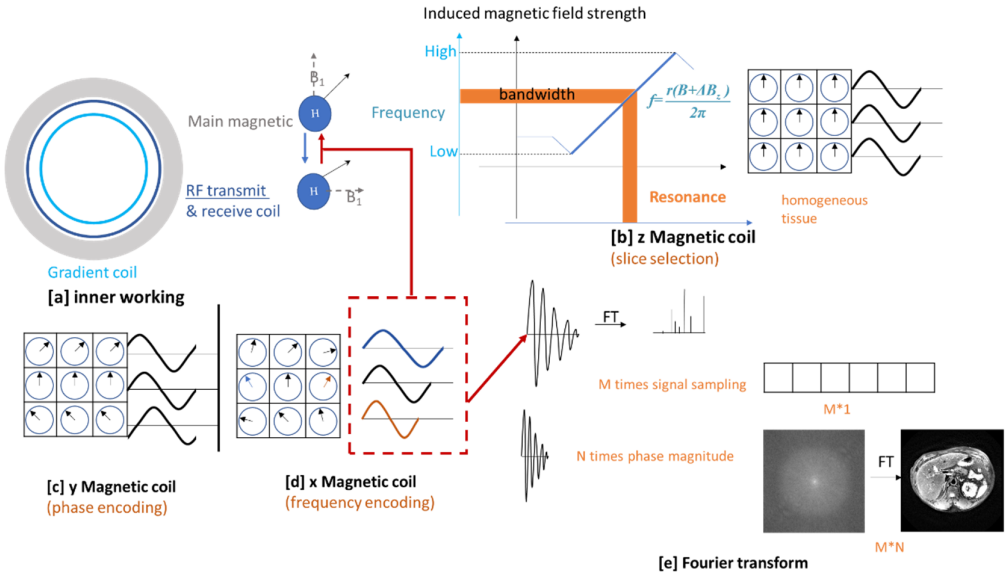

Fig. 2-3 Signal detection

Frequency encoding

The frequency encoding is similar to the phase encoding but switches at the x-axis (the last and third directions). While the frequency encoding is on, similar to the phase encoding, magnetization precesses at a different angular frequency along the x direction, as shown in Fig. 2-3 (d). Unlike with phase encoding, the signal is acquired during frequency encoding simultaneously. One FID packaged the information for all voxels recording the overall signal contributed by each voxel at the dependent starting phase and angular frequency.

Fourier transform

In fact, the FID signal is already in Fourier format and composes all voxel information. To obtain a 2D image, the conventional encoding is done as follows: for each phase encoding (performed M times), an MRI signal is sampled N times during the frequency encoding gradient application and the "k-space" is filled. Then the k-space (of size M*N samples) is transformed to the spatial domain by inverse 2-D Fourier transform, obtaining MR images of M*N voxels. One role of the MRI sequences is to determine the k-space coverage strategy. The modalities used in this thesis and their corresponding sequence will be presented in the next section.

2.4.4. MRI pulse sequences

For clinical application, T1-weighted (with and without Gd-based contrast agent injection) and T2-weighted imaging are the two most common sequences used for detecting abnormalities in structure and function. To obtain more informative data about liver tissue structure, multiple echo - gradient echo (or chemical-shift encoded), and multiple b-values diffusion MRI pulse sequences are included in my Ph.D. thesis work. The diffusion imaging will be discussed in detail in Chapter 3. In the patient cohort used in this thesis, T1-weighted, T2-weighted, CSE-MRI are acquired with gradient recalled echo (GRE), spin echo (SE), and multiple echoes GRE, respectively. This section briefly introduces the MRI pulse sequences, principles and their advantages and limitations.

Spin echo sequence

The principle of a SE sequence is schematically shown in Fig. 2-4 (a). In order to understand the spin echo principle, spin dephasing with T2* effect has to be considered. SE is composed of pairs of RF pulses: a 90° RF pulse applied for excitation and a 180 ° RF pulse applied for spin rephasing. After the 90° RF pulse, all spin magnetizations are entirely in-phase and immediately diphase at T_2^* rate within a voxel due to the external magnetic field inhomogeneity, chemical shifts, and static tissue susceptibility gradients. In order to cancel these effects, the 180° RF is placed after TE/2 times. Thus, all protons mirror flips along the x-z plane. The ahead of magnetic moment produced by the fastest frequency spin is flipped to the last phase. After TE/2 times, the spin magnetization refocuses and produces the highest signal in one echo. During the echo

time, several appropriate gradients are applied for field slice selection, phase encoding, and frequency encoding. The signal is acquired around the echo time and filled in k-space from left to right at the corresponding location. The refocusing by 180° RF pulse minimizes the signal loss by T2*. It brings high spatial frequencies signal— T2 weighted information usually at a high signal-to-noise ratio (SNR) if the echo time is correctly chosen, but it also causes longer acquisition time compared to gradient recalled echo.

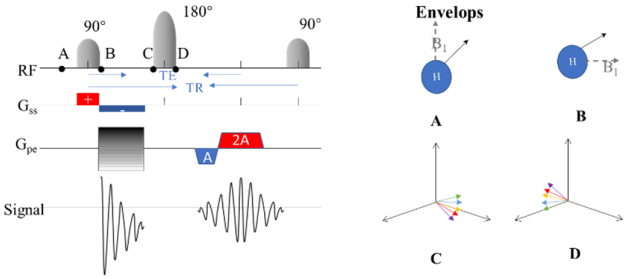

[a] Spin echo(SE)

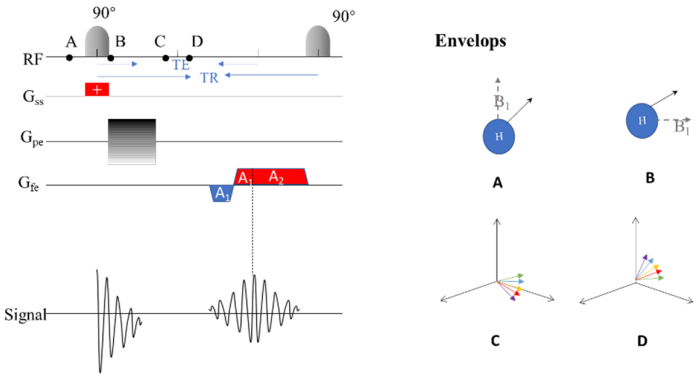

[b] Gradient recalled echo (GRE)

Thèse en traitement de l'image médicale / 2023
Institut national des sciences appliquées de Lyon

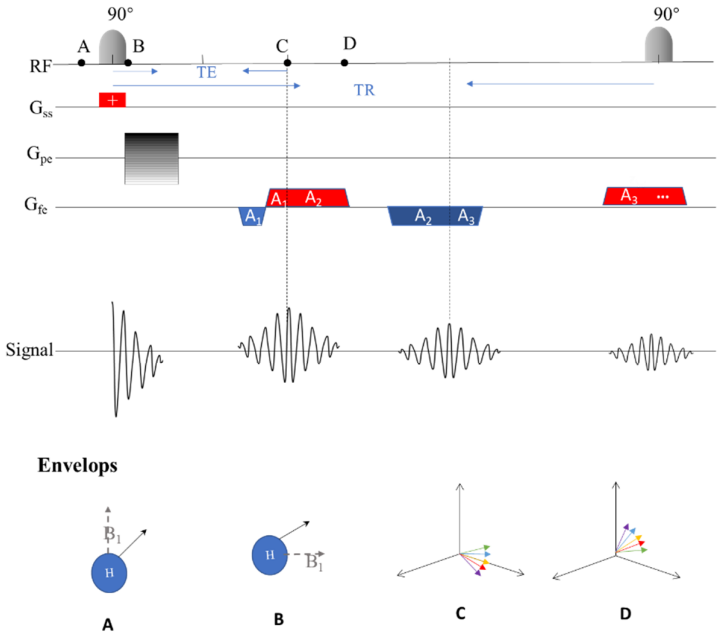

[c] multiple echoes GRE (mGRE)

Fig. 2-4 MRI pulse sequences

Gradient recalled echo

The GRE only has one excitation RF pulse, tilting the magnetization by usually less than 90, denoted by α. The larger the flip angle is the more the signal information will be T1-weighted, and the smaller the flip angle is the more the signal information will be weighted by T2*. The frequency encoding contains two opposite gradients, which generated a recalled echo. Magnetization diphase, rephase and diphase again during pairs of gradient encoding in opposite directions. This manipulation caused that the FID signal can be recorded without the disturbances of inhomogeneity produced by the gradient magnetic field. The principle is similar to spin echo in terms of dephasing and then rephrasing magnetization. Compared to the SE sequence however, the effect of field inhomogeneity is not refocused. The GRE pulse sequence methodology allowed the signal to be acquired far faster than a spin echo. Therefore, the GRE sequence is a template for most rapid imaging techniques. Also, in this case, the unmitigated T2* effect may produce the magnetic susceptibility artifact.

Multiple echo Gradients recalled echo

When the rephasing and dephasing encoding gradient are repeated alternately, the GRE sequence becomes the multiple echoes GRE (mGRE) as shown in Fig. 2-4 (c)-A. One of the most crucial applications of multiple echo GRE is fat-water separation imaging or chemical-shift encoded MRI (CSE-MRI), also called the Dixon technique. The elementary physical property of fat-water separation imaging is that the ^{1}H in water and fat have slightly different frequencies. Protons in fat precesse more slowly than in water. The relative magnetic movements produced by protons in these two substances can be seen as the hour and minute hands of a clock. Sometimes they overlap and generate a high-frequency signal called in-phase. Sometimes they are in opposite directions, called out phase. In this case, they cancel each other out. Therefore, if the signal could be acquired at least two certain times during multiple echoes, the fat and water can be separated. The use of parametric adjustment methods applied to the water/fat signal sampled at echo times determined by the use of several gradient echoes in a row allows the proportion of fat to water to be determined (PDFF).

2.5. Nuclear magnetic resonance applications

2.5.1. Focal liver lesion and destruction

In the course of liver disease development, a growth of focal liver lesions (FLL) is observed from hepatomegaly, focal nodular hyperplasia, scarring, cirrhosis, and further to HCC. Conventional MRIs, T_1 -, T_2 -, and T_2^* -weighted imaging, provide high-quality images and allow the liver to be viewed with different contrasts. T_1 -weighted images acquired mostly with gradient-echo sequences show low signal intensity in the FLL (Matos et al., 2015). However, the decline of the signal is also affected by fats, iron overload, highly concentrated proteins, etc.…(Furlan et al., 2009). T_2 -weighted images scanned with fast spin-echo sequences are employed to detect fluid content, fibrotic tissue, and iron content. T_2^* -weighted images acquired with multiple chemical-shift-encode echoes. However, the T_2^* -weighted imaging for assessing the focal liver lesion does not reach a consensus in the scientific community.

These different contrasts allow a comprehensive analysis of the lesion characterization but also bring pitfalls in imaging explanation mainly because their physical interpretation is difficult due to a lack of specificity.

2.5.2. Fatty depots and steatosis

Quantitative fat-water separation methods based on CSE MRI such as IDEAL-IQ, mDixon-Quant, or Q-Dixon are able to provide an accurate measurement of PDFF corrected from T2* relaxation effect and accounting for fat spectrum complexity, and T1 effect. In addition to PDFF, these methods also provide the measurement of T2* which is linked to liver iron concentration (LIC). Originally, MRS was the gold standard for PDFF. With the development of science and technology, MRI-PDFF has been the most accurate non-invasive quantitative biomarker of steatosis (Gu et al., 2019). Since MRI-PDFF is spatially-resolved in the three dimensions, it reduces the statistical bias and variance linked to MRS-based PDFF by reducing the sampling effect. For MRS, it sometimes showed less reproducibility than MRI-PDFF. This divergence could potentially stem from the intricate nature of configuring the fat spectrum model to accurately encompass the complex human triglyceride structure, alongside the challenge of fitting spectrum data in a reliable way. Additionally, the fidelity of MRS signals can be influenced by factors such as shimming conditions and the presence of respiratory motion. Meanwhile, steatosis is a confounding factor in molecular diffusion measurement and diffusion MRI is not used to measure steatosis.

2.5.3. Inflammation

The investigation into the connection between inflammation and multiparametric MRI maps has yielded inconclusive findings. Some studies noted a significant correlation between diffusion-weighted MRI and liver activity. Furthermore, research into multiple frequency elastography has proved a potential association between the multifrequency dispersion coefficient and inflammation (Garteiser et al., 2021; Sofue et al., 2020). Nevertheless, some experts remain cautious about the efficacy of these approaches (Moura Cunha et al., 2021). As a result, these attributes necessitate additional evidence and deeper exploration to ascertain their potential in replacing biopsy for inflammation grading.

2.5.4. Fibrosis

Fibrosis is an important indicator of CLD development and prognosis. In the fibrosis occurrence and progression, MRI technique usually illustrates from the perspectives of structure, stiffness, and hemodynamics. In data, the MR elastography (Garteiser et al., 2021; Sofue et al., 2020) remains the image method that has a great

prospect to replace the biopsy. Furthermore, a notable concept has been introduced the T1 mapping corrected for iron effects (T1c). This novel approach (exemplified by the commercially available 'Liver multiscan' solution by Perspectum) has emerged as a reliable non-invasive diagnostic method for staging fibrosis in CLD and also diagnosing NASH."

2.6. Conclusion

In this chapter, the blood test and liver radiology examination techniques have been presented, especially the principles of the promising technique MRI have been described. MRI enables multiple contrast mechanisms for different sources of CLD-related features. For promoting multi-parametric MRI into clinical adoption, it still needs to ensure the quantitative imaging biomarkers' reproducibility, standardize the multiple protocols, and further validate the values in the combination of multiple imaging techniques.

Chapter 3 state of the art of diffusion-weighted imaging

Contents

3.1. Diffusion physics

3.1.1. Brownian motion

Molecular diffusion is a basic thermal physical concept, usually simply named diffusion. Diffusion is produced by random motion in liquids or gases, also known as Brownian motion (Brown, 1828). Overall, diffusion almost reduces the gradients of concentration in water and tends to an even dynamic equilibrium. Albert Einstein proposed the Stokes-Einstein equation (Einstein, 1905; Stokes, 1851) to quantify the water diffusion D describing the average displacement of the molecules, as shown in Fig. 3-1 (a).

$$D = \frac{kT}{6\pi\eta r} \tag{3-1}$$

Where k is Boltzmann constant, T is the absolute temperature, $6\pi\eta r$ is mobility given by Stokes' law (η: medium viscosity, r: radius of particles).

3.1.2. Non-Gaussian diffusion

In a homogeneous medium, the diffusion shares the same rate in every direction, called the isotropic diffusion coefficient. In contrast, highly structured tissues disturbed the diffusion rate and direction. In biological tissue, the water molecules are confined in two distinct environments—in the tissue, denoted as "true" diffusion, or in the capillaries microcirculation, referred to as perfusion (Le Bihan et al., 1986). For "true" diffusion, water molecules exist in intercellular and intracellular spaces (Morozov et al., 2020).

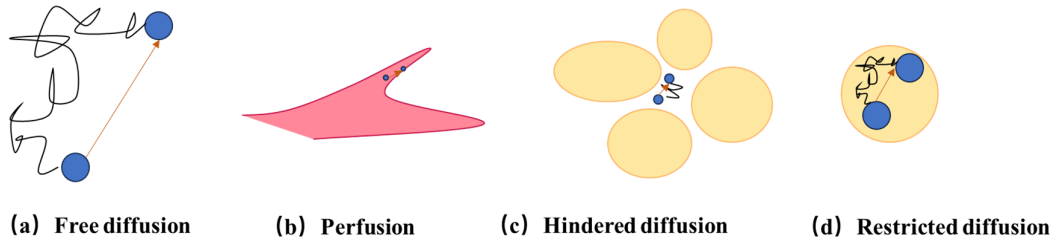

Fig. 3-1 The diagram of different diffusion types

Perfusion effect

The water molecules in the capillaries are propelled along with the randomly oriented blood microcirculation, as depicted in Fig. 3-1 (b). This movement causes their velocity to be thousands of times higher than that observed in free diffusion. It behaves

as free diffusion but hundreds of times faster than it, so-named pseudo-diffusion or fast diffusion. Although perfusion is physically different from diffusion, it confounds diffusion measurement.

Hindered diffusion

Neighboring cell membranes, linked fibers, and macromolecules hinder the water molecules out of the cells. The trajectory of molecular diffusion is along the intercellular pathway. The isotropic diffusion becomes anisotropic diffusion, and its rate decrease, as shown in Fig. 3-2.

Restricted diffusion

The water molecules inside the cells are restricted by the cell membranes. Compared to hindered diffusion, restricted diffusion is time-changing. In the beginning, water molecules freely diffuse. By the time the water molecules gradually approach the boundary, the increase leads to diffusion decreasing.

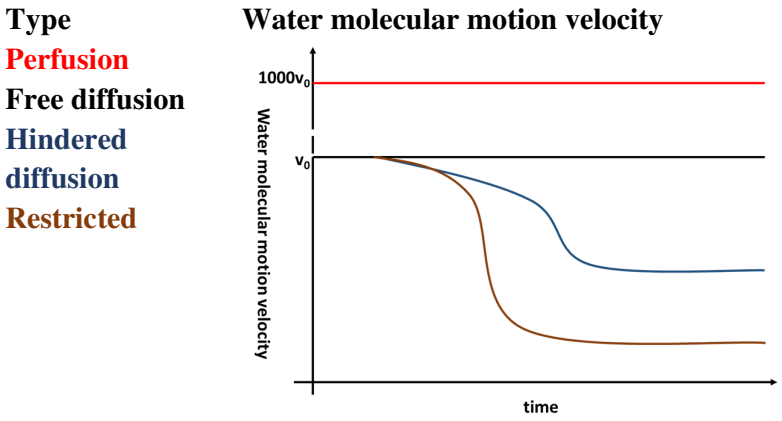

Fig. 3-2 Water molecular motion velocity in different micro-environment

3.1.3. Diffusion in liver

As we illustrated in the first chapter, the liver is the largest metabolic organ, carrying out the decomposition, synthesis, and exchange of substances all the time. Several studies have shown that liver lesion induced lower diffusion since the lesions increase the liquid impedance (Le Bihan, 2019). Therefore, diffusion-related imaging has been considered biomarker reflecting the liver's overall functional condition. Several clinical diagnostic criteria to distinguish different CLD are widely proposed referring to diffusion MRI (Anderson et al., 2014; Fujimoto et al., 2021; Zhou et al., 2019a).

Exchanged diffusion

Earlier studies have indicated that liver-diffuse disease relate to the impairment of protein liver synthesis (Bharwani & Koh, 2013). Thus, the decrease in protein will reduce the blood colloid osmotic pressure and the liquid remaining in the tissue. The minor suppression drives the lower exchanged diffusion observed on quantitative diffusion techniques.

Ballooning

Ballooning is measured by counting the hepatocyte ballooning identified by hepato-pathologists. Even though experienced pathologists still hold reserved opinions about histological analysis, the judgment about ballooning is exceptionally subjective (Brunt et al., 2022). However, it is clear that the intercellular space decreases with ballooning. Theoretically, the water molecules outside the cells are confined to a smaller intercellular space. The more congested molecular channel leads to lower diffusion (Gilbert, 2009).

Inflammation

Inflammation usually is diffuse damage due to toxic overloads, such as fat, alcohol, and virus. Chronic inflammation may lead to type V collagen excessive accumulation, which functions to lower inflammation (Narayanan, Engel, & Page, 1983). The collagens may also cause connective tissue disorder. It may indicate that diffusion could possibly be restricted by increased connective tissue, and perfusion could decrease with overloaded blood flow. So far, scientists and histologists still do not sufficiently understand the mechanism of inflammation at the biochemical level. It is difficult to quantify and clarify the mechanism of hepatitis via diffusion.

Iron overload

A high iron content deposition, often caused by hemochromatosis, can sometimes be concomitant with NASH. The excessive iron is finally stored in the liver. Although iron overload may cause CLD and, even worse –liver cirrhosis, it is still hard to accumulate abundant iron to the degree that causes liver damage. However, the magnetic properties of the iron have a huge impact on MRI imaging. More specifically,

it results in low diffusion signal intensity and minimal ADC values (Chandarana et al., 2012).

Steatosis

Hepatic steatosis is defined histologically by a proportion of hepatocytes with a fat vesicle higher than 5%. The effect of steatosis on diffusion can be explained from two perspectives. On the one hand, protons contained within triglyceride reduced diffusivity. On the other hand, the existing fat increases the viscosity of the cellular environment and contributes to molecular crowding. Correspondingly, lower diffusivity could be observed in patients with higher hepatic fat fraction (Makhija, Vikram, Srivastava, & Madhusudhan, 2021).

Fibrosis

Similar to inflammation, the fibrosis material (collagen, proteoglycan, etc…) deposition would restrict water diffusion. At the same time, fibrosis material deposition in the Disse space restrict liver micro-perfusion by reducing sinusoid permeability. As a result the perfusion-related diffusion measured with IVIM is decreased (P.-X. Lu et al., 2014).

3.2. Diffusion MRI

As we discussed, diffusion is a free or restricted motion of molecules within a liquid. This motion maps the molecules' interaction with versatile microenvironments linking to varying liver injuries. Torrey enriched Bloch equations with the interaction between macro-magnetization and molecular diffusion (Torrey, 1956), defined as formula 3-2.

$$\frac{d\overline{M}}{dt} = \gamma\overline{M} \times \overline{B}_0 - \begin{pmatrix} \frac{M_x}{T_2} \\ \frac{M_y}{T_2} \\ \frac{M_0 - M_z}{T_1} \end{pmatrix} + \overline{D}\nabla^2\overline{M} \qquad (3\text{-}2)$$

Where $\overline{D}$ is diffusion tensor, ∇^2 is Laplace operator. From now on, the information underlying the MRI signal was uncovered.

3.2.1. Diffusion sequence

On the basis of Bloch-Torrey equation, Stejskal and Tanner developed a specific sequence based on SE sequence (Stejskal & Tanner, 1965), as shown in Fig. 3-3. Likewise, the diffusion sequence composes a pair of RF pulses (90° and 180). Unlike SE sequence, there are pairs of linearly diffusion-weighted gradient impulses to three encoding directions between the encoding of slice selection and phase. In each direction, diffusion encoding contains two opposite gradients (G). The first encoding empowers proton to precess at location determined frequency, caused in magnetization diphase and signal losing. After a period of time (Δ), an opposite gradient in the same magnitude generated a recalled echo. The proton refocuses, nevertheless, the FID signal could not recover to the initial intensity. The proton diffused in interval time between two gradients usually change the location. These protons are not refocused perfectly, thus the signal loss because of molecular diffusion. Multiple recordings of FID signals with different diffusion interval times and diffusion gradients, allow diffusion information could be measured as a simplified equation, assuming the diffusion is isotropic and the same gradient diffusion encoded in tree directions）:

$$S_i = S_0 \exp(-b \times ADC)$$
$$b = -\gamma^2 \delta^2 (\Delta - \delta/3) G^2 \quad (3\text{-}3)$$

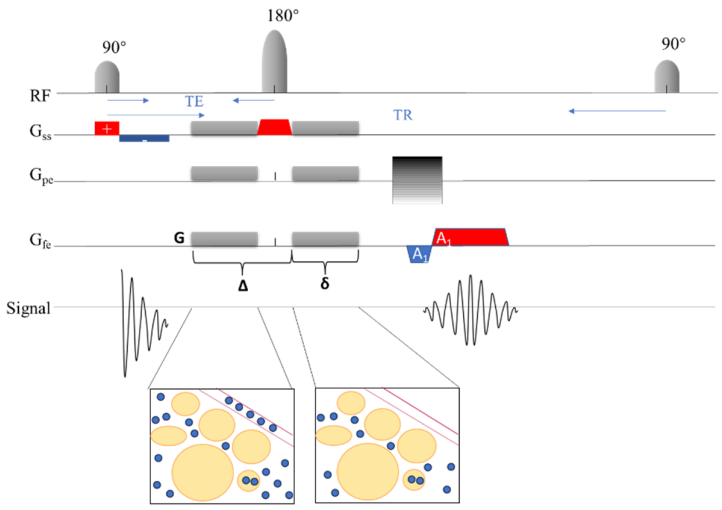

Fig. 3-3 Diffusion MRI sequence

where $\mathbf{S}_i$ represents the signal intensity at a given b-value and $\mathbf{S}_0$ represents the signal intensity when no pulsed diffusion gradient is applied. b-value is adjustable factor

which integrates with diffusion gradient properties, involving the strength of the diffusion gradient, G the duration of the gradient pulse, and the interval time between two gradient pulses. ADC is the magnitude of isotropic diffusion, named apparent diffusion coefficient.

Although the initial diffusion imaging sequence could detect the diffusion information, it requires long acquisition times and thus it is plagued by motion artifacts.

3.2.2. Fast imaging techniques

Echo planar imaging (EPI) is a rapid MRI acquisition technique; however, this speed comes at a cost. To acquire images quickly, the readout (data collection) process is usually accelerated. This acceleration can reduce the spatial resolution of the images. In this context, influential producers proposed their own sequence improving clinical application. The following is illustration of General Electric-EPI (GE-EPI). GE-EPI is comparable to mGRE sequence. After GRE sequence, a series of phase encodings and frequency encodings are applied. The rapidly alternating phase encoding will provide water motion information. The combination of intermittently blipped frequency encoding (along k-space horizontal) and phase encoding (along k-space versatile) moves the read-out direction like a zig-zag, as shown in the right of Fig. 3-4. In one repeated time, the several lines in k-space are filled. The strategy of filling data in k-space accelerates considerably the FID signal acquisition.

3.3. Diffusion models and their applications

Under the additional magnetic field gradients, diffusion signal attenuation is caused by the phase dispersion of transverse magnetization. This diffusion decay can be decomposed into three compartments – perfusion, limited isotropic diffusion, and non-Gaussian diffusion (hindered and restricted), as shown in Fig. 3-5, – depending on the water proton surroundings: microcirculation, tissue fluid, and intra- or extracellular membranes, respectively. The contribution of the parameters of each model in the triangular behaviors is listed in Table 3-1.

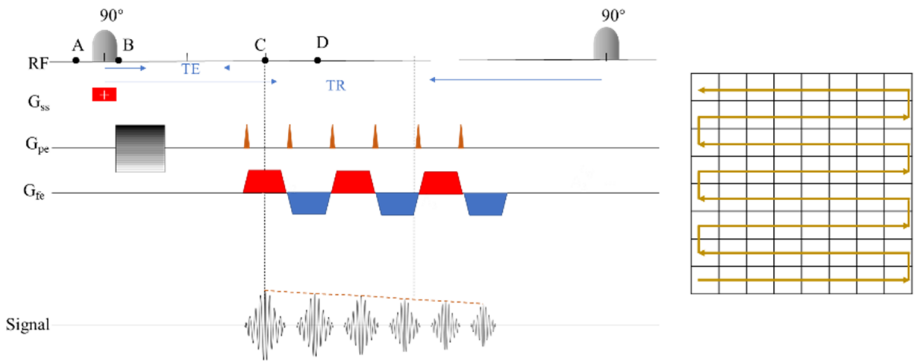

Fig. 3-4 General Electric echo-planar imaging (GE-EPI) sequence

3.3.1. ADC

The mean apparent diffusion coefficient (ADC), the most common diffusion parameter, fitted from the one-compartment mono-exponential diffusion model, assumes that the protons diffuse in a homogeneous environment. It is well-known that CLD patients have lower ADC-values than healthy individuals since the fibrosis material deposition restricts the movement of water molecules (Chandarana & Taouli, 2010).

3.3.2. IVIM

In 1988, Le Bihan et al. proposed the IVIM model, which quantified diffusivity separated into diffusion D and pseudo-perfusion D* effects (Le Bihan, 1988). In liver imaging, the influence of echo time (TE) on the apparent arterial fraction (f) is particularly crucial for tissues with substantially shorter transversal relaxation times compared to blood, as ignoring this effect could lead to an overestimation of the perfusion fraction f fraction, consequently limiting the. highest b-values used in liver MRI exams. Leporq et al. demonstrated that D and D* significantly decreased between early and advanced fibrosis groups (Benjamin Leporq et al., 2015). Lefebvre et al. also reported that perfusion fraction f is strongly correlated with inflammation and fibrosis after accounting for fibrosis and steatosis (Lefebvre et al., 2021). From these studies, it can be concluded that the parameters derived from the IVIM model could serve as alternative biomarkers for evaluating hepatic fibrosis with perfusion and diffusion parameters.

3.3.3. SEM

In 2003, Bennett et al. introduced an SEM applied in the brain that expanded the bi-exponential compartments to multi-compartments with fewer parameters than IVIM (Bennett et al., 2003) . Park et al. reported that DDC in the SEM presented a higher diagnostic function for hepatic fat staging compared with parameters in IVIM and ADC (Park et al., 2021). Moreover, SEM proved to be a promising method for fibrosis staging requiring fewer b-values than IVIM, but the physical significance of the diffusion rate parameter α remains unclear. Meanwhile, Seo et al. stressed inconsistent results in the association between α and fibrosis staging, which were attributed to different research subjects(Seo et al., 2018).

Table 3-1 Diffusion-based MRI model parameters and their structural proxy

Diffusion MRI model	Parameters	Definition (Structural proxy)	Function
Stat_D	D_s (mm²/s)	Position of distribution maxima ADC (Limited isotropic diffusion)	$\frac{\mathbf{S}_i}{\mathbf{S}_0} = exp(-\mathbf{b} \times D_s + \frac{1}{2} \times \mathbf{b}^2 \sigma^2)$
	σ (mm²/s)	Distribution width of ADC (Non-Gaussian diffusion)	
SEM	DDC (mm²/s)	Distributed diffusion coefficient (Limited isotropic diffusion)	$\frac{\mathbf{S}_i}{\mathbf{S}_0} = exp[-(\mathbf{b} \times DDC)^{\alpha}]$
	α	Diffusion (heterogeneity Perfusion)	
IVIM	f	Vascular volume fraction (Isotropic diffusion fraction)	$\frac{\mathbf{S}_i}{\mathbf{S}_0} = (1-f)exp(-\mathbf{b} \times D) + f \times exp(-\mathbf{b} \times D^*)$
	D (mm²/s)	Pure diffusion (Limited isotropic diffusion)	
	D^* (mm²/s)	Perfusion-related diffusion (perfusion)	
DKI	D_{app} (mm²/s)	Measured diffusion Limited isotropic diffusion	$\frac{\mathbf{S}_i}{\mathbf{S}_0} = exp(-\mathbf{b} \times D + \frac{1}{6} \times \mathbf{b}^2 \times D^2 \times K_{app})$
	K_{app}	Kurtosis effect (Non-Gaussian diffusion)	
Full	f, D, D^*, K_{app}	The exact representation in IVIM and DKI models	$\frac{\mathbf{S}_i}{\mathbf{S}_0} = f \times exp(-\mathbf{b} \times D^*) + (1-f) \times exp(-\mathbf{b} \times D + \frac{1}{6} \times \mathbf{b}^2 \times D^2 \times K_{app})$

3.3.4. DKI

In 2005, Jens *et al.* proposed the DKI model that quantifies water diffusion in tissue with non-Gaussian behavior, such as cellular compartments and membrane (Jensen, Helpern, Ramani, Lu, & Kaczynski, 2005). Yang *et al.* suggested that D_{app} and K_{app} can be used to determine the fibrosis stage (Yang et al., 2018). Daisuke *et al.* reported that K_{app} also correlated with the liver functionality index (Yoshimaru et al., 2019). Therefore, the DKI model can also potentially provide a useful biomarker for describing intracellular substructures, extracellular space, and metabolites.

3.3.5. Statistical diffusion model

In order to simultaneously quantify perfusion and non-Gaussian behavior, Yablonskiy *et al*. proposed a phenomenological statistical diffusion model that describes the *ADC* and its distribution (Yablonskiy, Bretthorst, & Ackerman, 2003); this model took into account perfusion and non-Gaussian behaviors. In particular, σ adjusts the width of the signal decay at low b-values, which plays an equivalent role to D^* in the IVIM model. For large b-values, the parameter σ slowed the diffusion decay, as the K_{app} function does in the DKI model. Zhou et al. explored the application of non-Gaussian models for the prognosis of colorectal cancer(Zhou et al., 2019). Significantly lower values of σ were observed in the response group before treatment (Zhou et al., 2019). Although this model has not yet been applied in the liver, the model effectiveness is still in doubt because one parameter is hard to estimate while capturing both perfusion and the non-Gaussian phenomenon.

3.3.6. FULL

For the separate computation of isotropic diffusion, perfusion, and kurtosis behavior, Wen-Chau Wu proposed the IVIM-DKI model for brain tumors (Wu, Yang, Chen, Tseng, & My, 2017). Fujima *et al.* investigated this model to predict head and neck squamous cell carcinoma and achieved high accuracy (Fujima et al., 2019).

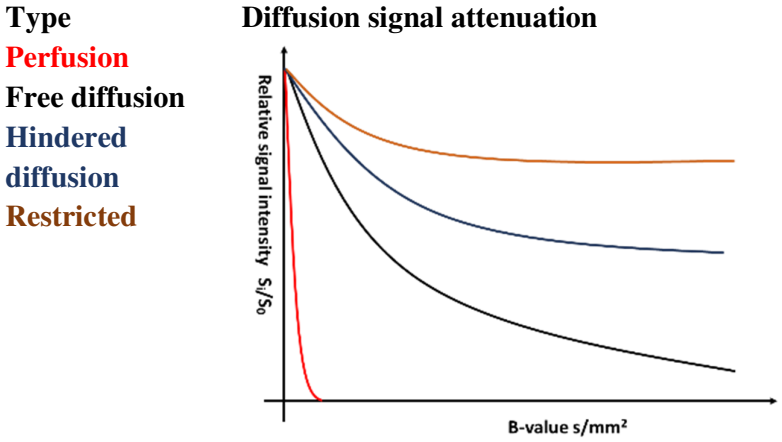

Fig. 3-5 Diffusion signal attenuation for different “diffusion”

3.4. Conclusion

In this chapter, we illustrate diffusion imaging in terms of physics, principles, sequences, models and applications. Diffusion MRI provides noninvasive way to characterize and discriminate the tissues monitoring the liquid trace from inter- and

intra-cellular. Diffusion imaging shows promise for diagnosing CLD, but its effectiveness is challenged by the need to account for diverse CLD characteristics, manage interactions between parameters, ensure meaningful interpretation and integrate other MRI modalities.

PART II

Contribution

Chapter 4 DWI of the liver in patients with CLD

: A comparative study between different fitting approaches and diffusion models (Original Article, accepted by JMRI, Huang et al., 2023)

Contents

4.1. Introduction

Chronic liver disease (CLD) represents a broad spectrum of diseases involving different etiologies (e.g., nonalcoholic steatosis, viral hepatitis, and hemochromatosis). These diseases are characterized by histological features such as inflammation, fibrosis, steatosis, ballooning, or iron overload. Among them, liver fibrosis is a key feature since it affects the prognosis and guides the treatment strategy (Roehlen et al., 2020). Overall, estimated 1.5 billion people worldwide have CLD, and 2 million people die from cirrhosis and liver cancer per year (Blachier et al., 2013; Cheemerla & Balakrishnan, 2021). Although liver biopsy carries an approximate 2% mortality with a high risk of major bleeding, followed histological analysis is still the reference method for the diagnosis of CLD, but its invasiveness limits its clinical use (Thomaides-Brears et al., 2022). Therefore, an alternative noninvasive, sensitive and specific method for population screening and monitoring remains an unmet medical need.

Diffusion-weighted imaging (DWI) derived from MRI has been increasingly used in liver examinations because of the excellent insight offered by the quantitative measurement of water molecule movement in different microenvironments. The respective water diffusion is intrinsically linked to the degree of liver fibrosis (Lewis, Dyvorne, Cui, & Taouli, 2014). Such methods have been investigated extensively in the literature (Annet et al., 2007; Bennett et al., 2003; Gambarota, Hitti, Leporq, Saint-Jalmes, & Beuf, 2017; Le Bihan et al., 1986; Lefebvre et al., 2021; Benjamin Leporq et al., 2015; Lewis et al., 2014; Yablonskiy et al., 2003a). Specifically, CLD patients have lower apparent diffusion coefficient (ADC) values than healthy individuals since the abnormal liver parenchyma increase the liquid impedance (Le Bihan, 2019). However, the diagnostic value of ADC in the evaluation of fibrosis remains relatively controversial (Annet et al., 2007; Yoshimaru et al., 2019). Annet et al. demonstrated that the lower ADC values in fibrotic livers were caused mostly by perfusion alterations rather than decreased extra-vascular diffusion. Meanwhile, Yoshimaru et al. showed ADC-values were undervalued in cirrhotic tissue and tumors due to the restriction of molecular movement in a high cellularity structure. In consequence, the simple ADC model shows difficulty in describing such multifactorial synergy mechanisms. Hence, in recent diffusion MRI studies, several advanced diffusion models were proposed to solve this problem, such as intravoxel incoherent motion (IVIM) (Le Bihan et al., 1986), stretched exponential model (SEM) (Bennett et al., 2003), statistical diffusion model

(Stat_D) (Yablonskiy et al., 2003a).

In 1986, Le Bihan et al. proposed the IVIM model, which quantified diffusivity separated into diffusion (D), pseudo-perfusion (D*) effects, and perfusion fraction (f) (Le Bihan et al., 1986). Leporq et al. demonstrated that D and D^* significantly decreased between early and advanced fibrosis groups (Benjamin Leporq et al., 2015). Lefebvre et al. also reported that f was strongly correlated with inflammation and fibrosis after accounting for fibrosis and steatosis (Lefebvre et al., 2021). However, an incomplete understanding of the IVIM mechanism in the tissue structure led to difficulties in separating the pseudo-perfusion and diffusion effects (Le Bihan, 2019).

In 2003, Bennett et al. introduced SEM in the brain that expanded the bi-exponential compartments to multi-compartments with fewer parameters than IVIM (Bennett et al., 2003). The SEM model evaluated the average diffusion rate through distributed diffusion coefficient (DDC) and diffusion heterogeneity (α) (Bennett et al., 2003). Park et al. reported that DDC in SEM presented a higher diagnostic function for hepatic fat staging compared with parameters in IVIM and ADC (Park et al., 2021). Moreover, SEM may be regarded a promising method for fibrosis staging requiring fewer b-values than IVIM, but the physical relevance of α remains unclear (Seo et al., 2018).

In 2003, Yablonskiy et al. proposed a phenomenological Stat_D that describes the ADC (D_s) and its distribution (σ) (Yablonskiy et al., 2003a). Zhou et al. explored the application of non-Gaussian models for the prognosis of colorectal cancer (Zhou et al., 2019) . Significantly lower values of σ were observed in the response group before treatment. Although this model has not yet been applied to study the liver, the model's effectiveness is still in doubt because one parameter is hard to estimate while capturing both perfusion and the non-Gaussian phenomenon.

In this context, the aim of the present study was to investigate the effects of different fitting methods on the measurement of diffusion parameters from IVIM, SEM, and Stat_D models and to study their relationship with diffuse parenchyma liver disease-related features, particularly for fibrosis assessment.

4.2. Materials and methods

4.2.1. Numerical simulation

To evaluate numerically the accuracy of fitted parameters with different noise level conditions according to the diffusion model function and the different fitting methods, we simulated diffusion MRI signals with multiple b-values for all the aforementioned

diffusion models. All simulations were implemented in MATLAB R2019b (The MathWorks Inc., Natick, MA, USA). For each voxel, the diffusion parameters can be represented as $S_i = S_0 \times L(\mathbf{c})$, where S_i represents the signal intensity at a given b_i-value, S_0 represents the signal intensity without a diffusion gradient, and c and $L(\mathbf{c})$ are the model parameters and model function, respectively. First, the Gaussian distribution randomly generated the coefficient with a certain mean and standard deviation, as shown in Table 4-1. Then, the advanced diffusion model signals were calculated with their function, as described in Table 4-2.

Table 4-1Major parameter settings in the simulation

Parameters	Model		Values
b-values set (s/mm^2)	-		0, 10, 20, 40, 60, 80, 100, 200, 300, 400, 600, 800
-	STD	D_s ($\times 10^{-3}$mm^2/s)	1.34 ± 0.81
		σ ($\times 10^{-3}$mm^2/s)	0.37 ± 0.18
	SEM	DDC ($\times 10^{-3}$mm^2/s)	1.353 ± 0.268
		α	0.569 ± 0.073
	IVIM	f (%)	24.6 ± 7.28
		D ($\times 10^{-3}$mm^2/s)	0.91 ± 0.19
		D^* ($\times 10^{-3}$mm^2/s)	76.2 ± 7.98

Abbreviations: Stat_D, Statistical diffusion model; SEM, Stretched exponential model; IVIM, Intravoxel incoherent motion. In the simulation, the same b-values were used as in the in vivo study. The parameters were assumed to follow Gaussian distribution. The data are represented as median ± standard deviation.

The noise levels were impacted differently according to the different b-values. We thus considered adding various inherent noises that we characterized through the Rician–STD method (Coupé et al., 2010) from 85 patients DWI detailed in MRI acquisition (Liu et al., 2020). The simulated diffusion signals were then corrupted by Rician noise, which was closer to the actual noise power than the Gaussian distribution since magnitude MRI data were used. The probability distribution for the noisy signal can be calculated as follows:

$$NS_i = \sqrt{S_i + \sigma R_i \times randn(n)^2 + \sigma I_i \times randn(n)^2}, i=1,...,12 \quad (4\text{-}1)$$

where NS and S represent the noisy signal and pure, noiseless signal, respectively, i is the index of b-values, and σR_i and σI_i are averaged standard deviation at specific b-values for the real and imaginary parts, respectively. In practice, the real and imaginary parts shared the same values simplifying the noise model. After generating the ground truth and noisy signal, the parameters were estimated using NLS, segmented NLS, and Bayesian fitting methods. The performance of the three estimation methods was validated by mean squared error on fitted parameters and mean absolute percentage error on signal.

4.2.2. Patient population

In this study, the patients were retrospectively enrolled from a database of 85 patients with CLD (Liu et al., 2020), including alcoholic hepatitis, NASH, and viral hepatitis. This database included conventional diagnostic MRI acquisitions and multiple b-values diffusion acquisition, hepatic blood biomarkers, fibroscan results and histology. This database was built in our institution. Our institutional review board approved this retrospective study and the requirement to obtain informed consent was waived. Information on the patient population is summarized in Table 3. Inclusion criteria were age superior to 18 years; chronic liver disease based on clinical history or prior examination; need for liver biopsy and liver MRI imaging. Exclusion criteria included liver transplantation within the last six months, acute liver disease, pregnancy and patient with claustrophobia, metallic implant, pacemaker or coagulation disorders.

Table 4-2 Diffusion-based MRI model parameters and their structural proxy

Diffusion MRI model	Parameters	Definition (Structural proxy)	Function
Stat_D	D_s (mm^2/s)	Position of distribution maxima ADC (Limited isotropic diffusion)	$\frac{\mathbf{S}_i}{\mathbf{S}_0} = exp(-\mathbf{b} \times D_s + \frac{1}{2} \times \mathbf{b}^2 \sigma^2)$
	σ (mm^2/s)	Distribution width of ADC (Non-Gaussian diffusion)	

SEM	DDC (mm^2/s)	Distributed diffusion coefficient (Limited isotropic diffusion)	$\frac{\mathbf{S}_i}{\mathbf{S}_0} = exp[-(\mathbf{b} \times DDC)^{\alpha}]$
	α	Diffusion (heterogeneity Perfusion)	
IVIM	f	Vascular volume fraction (Isotropic diffusion fraction)	$\frac{\mathbf{S}_i}{\mathbf{S}_0} = (1-f)exp(-\mathbf{b} \times D) + f \times exp(-\mathbf{b} \times D^*)$
	D (mm^2/s)	Pure diffusion (Limited isotropic diffusion)	
	D^* (mm^2/s)	Perfusion-related diffusion (perfusion)	

Abbreviations: Stat_D, Statistical diffusion model; SEM, Stretched exponential model; IVIM, Intravoxel incoherent motion

4.2.3. Diffusion-weighted MRI acquisition

All patients underwent an MRI examination with a 3-Tesla system (GE MR750, GE Healthcare, Chicago, IL, USA). The DWI sequence was a spin echo-echo planar imaging (SE-EPI) enhanced DWI (eDWI) acquired in the transverse plane using a tetrahedral gradient encoding (i.e., four combinations of x, y, and z gradients within 50 mT/m^{-1}) (Finkelstein, Cao, Liao, Schifitto, & Zhong, 2022). The acquisition parameters of the diffusion MRI protocols are listed in Table 4-4. The MRI signal was acquired with 128 × 96 matrix, a field of view (FOV) of 400 x 300 mm^2, and joined slices had a slice thickness of 8 mm and were reconstructed in 256× 256 by zero filling to a FOV of 400 x 400 mm^2. No motion correction or fat saturation pulses were applied.

Table 4-3 Patient characteristics

		Values
General information	Gender	Male: *n*=49 Female: *n*=36
	Age (years)	47.9 ± 15.5 [20–80]
	Height (m)	1.70 ± 0.11
	Weight (kg)	76.8 ± 17.99
Laboratory parameters	ASAT(U/L)	51.25 ± 39.28
	ALAT(U/L)	83.80 ± 89.48
	ISHAK score	F0: 9, F1: 20, F2: 15 F3: 15, F4: 16, F5: 8, F6: 2
	Inflammation	A0: 28, A1: 47, A2: 10
Clinical etiology	Alcohol	23
	NASH	23
	Viral hepatitis	B: 24 C: 21 Others: 4
	Liver transplant	7

Abbreviations: ASAT, Aspartate transaminase; ALAT, Alanine transaminase; NASH, Nonalcoholic fatty liver disease. Data are represented as median ± standard deviation, with the unit in parentheses and range in brackets.

4.2.4. Diffusion parameter fitting methods

Under the additional magnetic field gradients, diffusion signal attenuation is caused by the phase dispersion of transverse magnetization (Lewis et al., 2014). This diffusion decay can be decomposed into three compartments: perfusion (eg. D^*, α, σ), limited isotropic diffusion (eg. D, D_s , DDC), and non-Gaussian diffusion (eg. σ), depending on the water proton surroundings (microcirculation, tissue fluid, and intra- or extracellular membranes) (Supplementary material). The contribution of the parameters of each model in the triangular behaviors is listed in Table 2. The MRI diffusion-weighted signals were acquired for the pre-defined b-values indexed with i =1,2,3,…,12. The parameters (Table 4-2) were fitted using a nonlinear least squares method (NLS), a combination of an NLS fit with a segmented approach as a first step

to initiate NLS guess values (segmented NLS), and Bayesian methods (Luciani et al., 2008; Meeus et al., 2017; X. Wang et al., 2021; While, 2017). The following equation describes the process for the IVIM model (Table 4-2). In this case, the model function is given by equation:

$$\frac{S_i}{S_0} = (1-f)\times\exp(-b\times D)+f\times\exp(-b\times D^*) \quad (4\text{-}2)$$

where S_i represents the signal intensity at a given b-value and S_0 represents the signal intensity when no pulsed diffusion gradient is applied.

Table 4-4 MRI acquisition parameters

Parameters	Sequence
	SE-EPI-eDWI
b-values (s/mm²)	0, 10, 20, 40, 60, 80, 100, 200, 300, 400, 600, 800
TE (ms)	54.3
TR (ms)	2050
Acquisition matrix size	128×96
Matrix size	256×256
FOV (mm²)	400×300
Signal average	2, 2, 2, 2, 3, 3, 4, 5, 6, 7, 8, 9
Slice thickness (mm)	8
Acquisition time(s)	312

Abbreviations: SE-EPI-eDWI, Spin echo-echo planar imaging-enhanced diffusion-weighted imaging; TE, Echo time; TR, Repetition time; FOV, Field of view. Adjacent slices were joined with no gap between the slices.

Nonlinear least squares method

The NLS method iteratively finds the best fit for the given nonlinear data by minimizing an objective function, such as in equation (4-2) constituted by the residual sum of squares, i.e., the sum of the squares of residuals (deviation of estimated model from actual acquired data):

$$\sum_{i\in b \text{ values set}} (S_i - \hat{S}_i)^2 \quad (4\text{-}3)$$

where $\hat{S}_i$ is the reconstructed signal with the estimated parameters in each iteration. The

parameters are updated by the gradient descent until convergence or until reaching the maximum number of allowed iterations.

Segmented NLS method

For the NLS methods to work properly, the parameters need to be weakly correlated (Sigmund et al., 2011). However, in the diffusion models studied, most of the model parameters are highly correlated, which leads to an often ill-posed problem and results in a high noise level dependence (Jalnefjord et al., 2018). To help distinguish between the water motion in diffusion from perfusion behavior, the segmented NLS method adopts a piecewise fitting strategy. The D^* is a hundred times higher than D (Jalnefjord et al., 2018). Thus, the D^* can be negligible when the b-value is high enough ($b \geq b_{th}$). In this case, the signals are considered as nearly pure diffusion. In the first step, the IVIM model is simplified to a mono-exponential model:

$$S_i = S_{b_{th}} \exp[(-b+b_{th}) \times \hat{D}] = S_0 (1-f) \exp(-b \times \hat{D}) = \hat{A} \exp(-b \times \hat{D}) \; (b >= b_{th}) \qquad (4\text{-}4)$$

The perfusion fraction is calculated as $\hat{f} = 1 - \hat{A}/S_0$. The parameters are underestimated ($\hat{D} < D, \hat{f} < f$). Therefore, the parameter values fitted in this piece can be used as lower bounds for the next steps.

Then, f and D^* were estimated in $b \leq b_{th}$ with fixed D as follows:

$$S_i = S_0 \{\exp[(1-f)(-b \times D)] + \exp[f(-b \times D^*)]\}, (f > \hat{f}, b \leq b_{th}) \qquad (4\text{-}5)$$

Bayesian method

The NLS-based methods find the optimized parameters with respect to the residuals. By contrast, the Bayesian approach maximizes the posterior probability with the observed signal, an infinite parametric distribution, and noise distribution (Gustafsson, Montelius, Starck, & Ljungberg, 2018). The objective function is defined as:

$$\text{argmax}\, p(P, \beta, \Sigma_\beta | S) \propto p(S | P, b, \beta, \Sigma_\beta)\, p(P | \beta, \Sigma_\beta) \qquad (4\text{-}6)$$

where P is a vector of the IVIM's parameters, including, f, D, D^*, S_0, and β, Σ_β, which are the mean values of P and their covariances. In practice, to estimate the full parameters with the Bayesian method in a finite time, a Monte Carlo Markov chain (MCMC) is built, and Metropolis–Hastings sampling with a shrinkage strategy is used to accelerate the MCMC convergence (Rodrigues et al., 2019). In Bayesian estimation,

the parameters are initialized by the NLS results, and their priors are assumed to be of Gaussian form, except for f, which is supposed to have a uniform distribution (Jalnefjord et al., 2018).(Jalnefjord et al., 2018)

4.2.5. In vivo data analysis

Based on the MRI acquisition, the different models were used to compute diffusion parameters with the three fitting methods (NLS, segmented NLS and Bayesian) for each voxel within Regions of interest (ROIs). The ROIs were placed in the entire right hepatic lobe to minimize the heartbeat effect in MATLAB R2019b (The MathWorks Inc., Natick, MA, USA). For each patient, 5 slices were located in the middle of the liver by J.H. with the guidance of B.L. (12 years' experiences) ensuring the largest view of the liver lobe. For post-processing, MR signals were arranged in ascending order into multiple vectors (1×number of b-values) at each pixel. The mean values in ROI for all parameters were calculated for each patient.

4.2.6. Histology

All patients underwent liver biopsy under ultrasound guidance. A 15G needle was inserted slightly below the bottom right rib cage to obtain the tissue samples. The mean biopsy length was 13.08 ± 2.35 mm (range: 7-18 mm) and the cross-sectional area was 9.14 ± 3.15 mm^2 (range 2.08-18.72 mm^2). Tissue samples were embedded in paraffin after being fixed in buffered formalin. All histological slides were stained with hematoxylin-eosin-saffron, Sirius red, and Perls stain. Histopathological assessment was achieved blinded to any clinical information or MRI result by two pathologists (pathologist 1: 20 years of experience and H.V. (co-author): 10 years of experience) according to Ishak, non-alcoholic fatty liver disease activity score(NAS), and meta-analysis of histological data in viral hepatitis (METAVIR) for fibrosis, steatosis, and inflammation, respectively(Arjmand et al., 2020; Yin et al., 2019). The histopathologic analysis was reviewed by H.V. and the discrepancies were co-validated. The area of steatosis and fibrosis (in %) were evaluated by H.V. The percentage of steatosis was morphological and semi quantitative (NAS) and the percentage of fibrosis was morphological and quantitative. Image analysis was performed by using a light microscope (Eclipse E400, Nikon France, Champigny, France) equipped with a tri-CDD video camera (Sony, Tokyo, Japan) was determined by morphometric analysis (Hisolab, Microvision Instruments, Evry, France). Inflammation was measured by combining the degree of portal necrosis and lobular necrosis based on METAVIR.

4.2.7. Statistical analysis

Statistical analyses were performed in GraphPad Prism (version 5.0 for Windows, GraphPad Software, San Diego, California USA) and MATLAB R2019b (The MathWorks Inc., Natick, MA, USA). To evaluate diffusion parameters in assessing liver fibrosis, we analyzed the results of the three fitting approaches by computing the Spearman correlation coefficients between the diffusion parameter mean values and the fibrosis area. We also evaluated associations between liver steatosis and the diffusion parameters by computing Spearman correlation coefficients between the diffusion parameters and the steatosis area. Based on the Ishak score, the patients were divided into two groups according to fibrosis severity (mild fibrosis [F0–F2] vs. severe fibrosis [F3–F6]) and according to the activity score (no inflammation [A0] vs. hepatitis [A1–A2]). Mann–Whitney U-test was used to compare averaged diffusion parameter values for the different groups. A statistical significance level of 0.05 was used, such that any p-value below this threshold was deemed significant.

The parameters showing significant differences with $p<0.01$ between the groups for a given fitting method were combined to build classifiers based on several conventional machine learning methods (Supplementary material), including linear regression, decision tree (DT), quadratic discriminant (QD), logistic regression, naïve Bayesian (NB), support vector machines (SVMs), and k-nearest neighbor (KNN) methods (MATLAB R2019b Classification Leaner; The MathWorks Inc., Natick, MA, USA). The classification task consisted in determining if a patient belongs to a severe or mild fibrosis group using diffusion parameters. The dataset was divided into training (75%) and test subsets (25%) by stratified sampling strategies to guarantee completeness (involving all possibilities) and identities (same proportions as the population). In training, 10-folders cross-validation was used for generalization to avoid the high model bias or overfitting problem. In order to tune the hyperparameters of the aforementioned classification methods, the hyperparameter optimization option was activated in the Hyperparameter Optimization Options toolbox of MATLAB. After training the classifiers, receiver operating characteristic (ROC) analysis with the area under the curve (AUC) was performed on the test subset to evaluate the diagnostic performance in classifying mild or severe fibrosis.

4.3. Results

4.3.1. Simulation

The diffusion signals were calculated as the ground truth according to the fixed parameters described in Table 4-1 and Table 4-2. The average standard deviations of noise given through the Rician–STD method were found to be 6.1, 4.2, 4.2, 4.1, 3.7, 3.6, 3.4, 2.9, 2.6, 2.4, 2.3, 2.5 for b-values ranging from 0 to 800 s/mm^2.

The relative errors between the reconstructed signal or fitted parameters and their corresponding ground truth are displayed in Fig. 4-1 with their mean ± standard deviation plots in order to assess the accuracy performance. The Bayesian fitting method almost systematically improved the accuracy of the parameters compared with the NLS-based method (Figure 1 a and b). The relative errors in pure diffusion parameters were less than 10%, and in signal amplitudes even less than 2%. However, there were greater errors with advanced diffusion parameters, especially for σ and D^*.

4.3.2. In vivo study

Figure Fig. 4-2 shows the representative diffusion parameters fitted by the three methods for patients with severe and mild fibrosis. Fig. 4-3 summarizes the statistically significant correlation coefficients that were found between limited isotropic diffusion parameters and steatosis (Fig. 4-3 a) or fibrosis area (Fig. 4-3 b). A higher correlation was observed for parameters fitted by the Bayesian method compared with the other methods. The highest correlation was found with the Bayesian method for D_s in the Stat_D model that showed the strongest and statistically significant negative correlation with steatosis (r=-0.46). For fibrosis area, a weak but still significant correlation (α: r = 0.23, D^*: r= 0.24) was found with the parameters fitted with the Bayesian method.

Significant differences were found between the groups with different degrees of fibrosis: D_s, D_{app} as well as σ, α and D^*(Table 4-5). In addition, statistically significant differences were only found for diffusion parameter estimations obtained with the Bayesian inference method (D_s and σ). When considering inflammation groups, no significant differences between groups were found for the different fitted parameters (no inflammation[A0] vs. hepatitis[A1-A2], p-values ranged from 0.11~0.95). Decision tree with Bayesian fitted parameters, as shown in Fig. 4-4, achieved the best AUC. The AUC was 0.92 (sensitivity=0.91 and specificity=0.70), as shown in the ROC curve in Fig. 4-5.

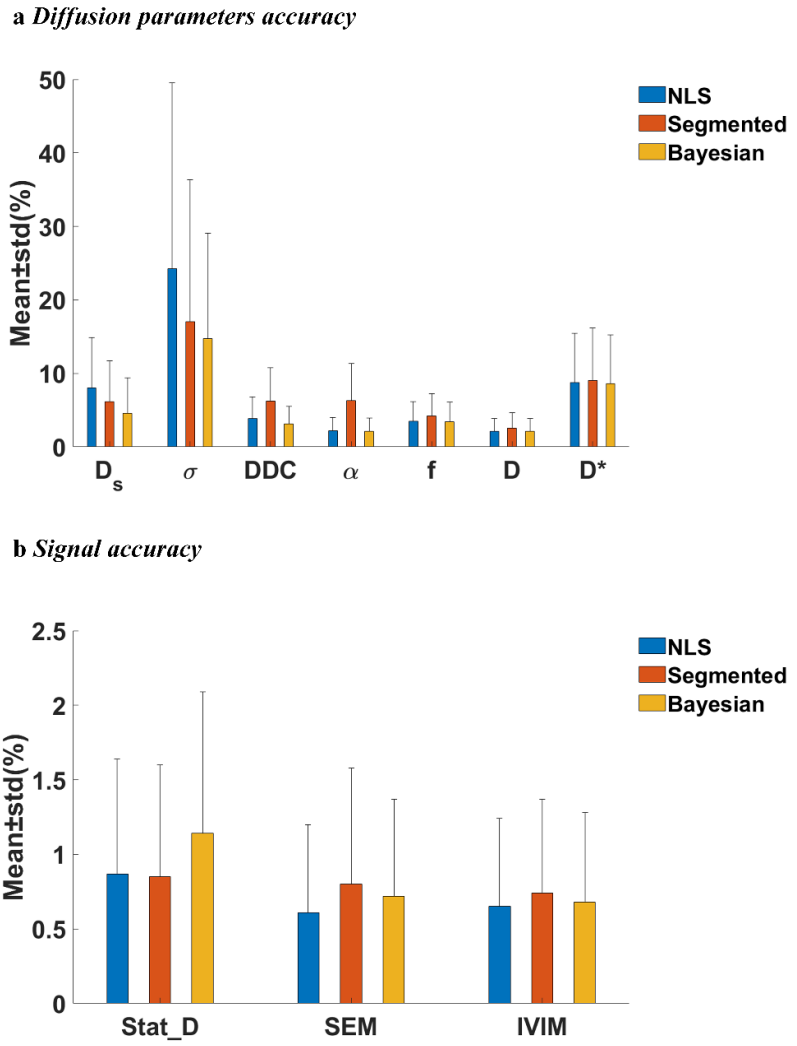

Fig. 4-1Estimation of accuracy in parameters and signal. In the simulation, all parameters fitted by NLS, segmented NLS, and Bayesian methods were compared with the ground truth. Subfigure(a): comparison of three estimators for different parameters between ground truth and fitted-parameters based on mean squared error. Subfigure(b): comparison of three estimators for signal between ground truth and reconstructed signal based on mean average percentage error. Abbreviations: NLS, Nonlinear least squares method

4.4.Discussion

In this work, we evaluated the effect of different fitting methods on the quantification of diffusion parameters from different models. Compared with the NLS-based method, the Bayesian approach provided greater accuracy in diffusion parameter estimation and fibrosis classification.

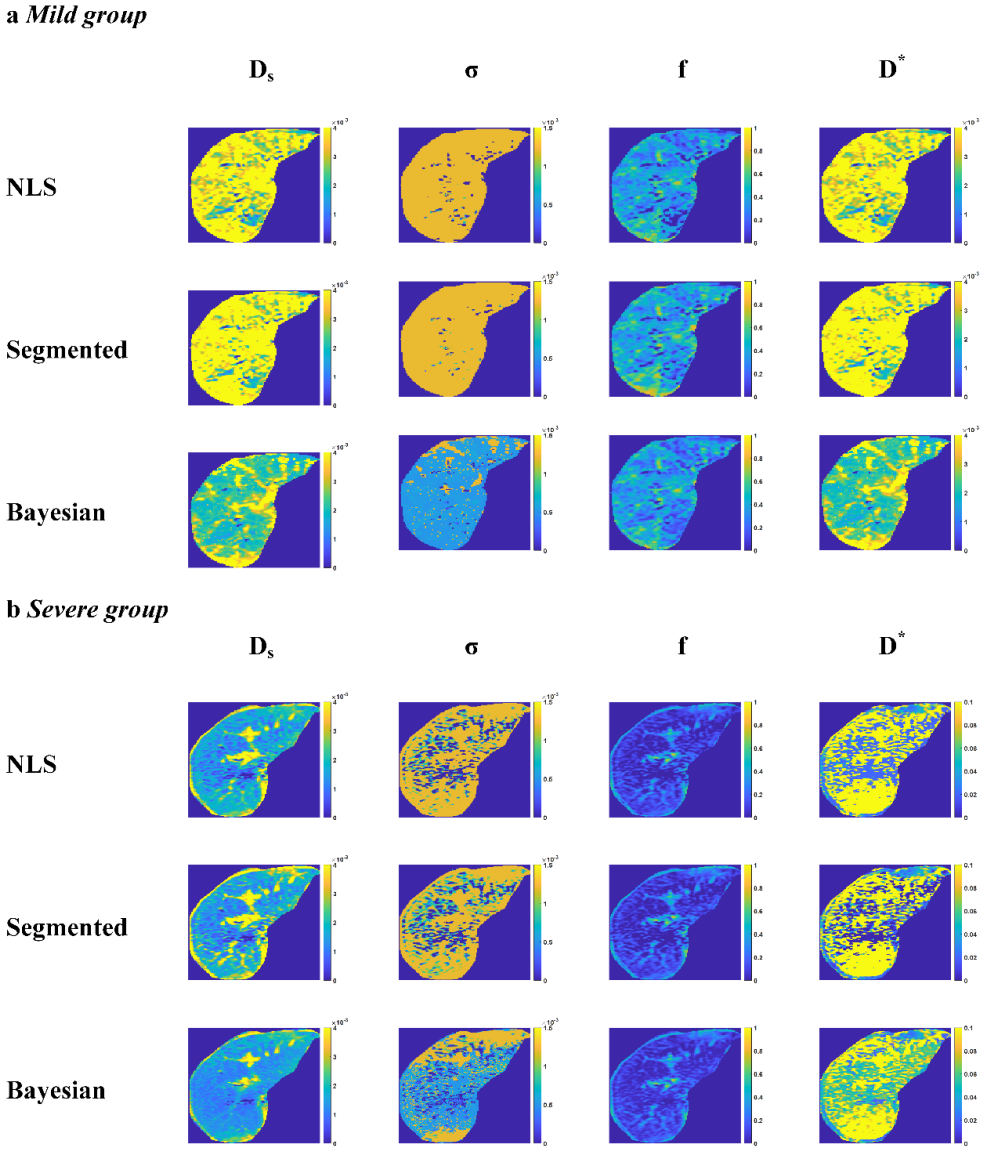

Fig. 4-2 Representative diffusion parameters (mm2/s) fitted by three methods for two fibrosis groups Abbreviations: NLS, Nonlinear least squares method

Table 4-5 Diagnostic values of diffusion parameters in diagnosing mild and severe fibrosis (*p<0.05, **p<0.01, ***p<0.001)

		NLS	Segmented	Bayesian
D_s(×10^{-3}mm^2/s)	Mild	3.11 ± 0.59	3.37 ± 0.58	**2.63 ± 0.60**
	Severe	2.78 ± 0.76	3.03 ± 0.77	**2.18 ± 0.58**
	p	**	**	***
σ(×10^{-3}mm^2/s)	Mild	1.06 ± 0.11	1.08 ± 0.10	**0.85 ± 0.20**
	Severe	1.00 ± 0.12	1.01 ± 0.12	**0.71 ± 0.16**
	p	**	**	***
DDC (×10^{-3}mm^2/s)	Mild	2.30 ± 0.57	1.37 ± 0.23	2.28 ± 0.56
	Severe	2.04 ± 0.69	1.30 ± 0.25	2.03 ± 0.65
	p	*	0.13	*
α	Mild	0.58 ± 0.07	0.49 ± 0.08	0.58 ± 0.07
	Severe	0.62 ± 0.10	0.54 ± 0.10	0.62 ± 0.09
	p	*	*	0.06
f	Mild	0.22 ± 0.05	0.23 ± 0.05	0.22 ± 0.04
	Severe	0.20 ± 0.06	0.20 ± 0.07	0.20 ± 0.06
	p	*	*	*
D(×10^{-3}mm^2/s)	Mild	1.34 ± 0.24	1.30 ± 0.22	1.36 ± 0.23
	Severe	1.24 ± 0.25	1.21 ± 0.23	1.27 ± 0.24
	p	*	0.07	*
D*(×10^{-1}mm^2/s)	Mild	1.18 ± 0.37	0.98 ± 0.33	**1.03 ± 0.34**
	Severe	1.05 ± 0.37	0.89 ± 0.33	**0.84 ± 0.26**
	p	0.11	0.18	**

Abbreviations: NLS, Nonlinear least squares method. The values are mean values and standard deviation for the average parameters in two groups. A p-value <0.05 was considered statistically significant.

The present numerical experiments conducted on simulated signals demonstrated that the Bayesian approach performed better than the NLS-based methods for most parameter estimations. Bouhrara et al. also reported similar results for the IVIM and SEM models in a simulation study (Bouhrara, Reiter, & Spencer, 2015). The Bayesian method systematically outperformed the NLS-based method in parameter estimation, probably because the Bayesian method reduced the influence of noise on parameters according to the prior and also because it started from the NLS-based estimations (Bouhrara et al., 2015). The Bayesian approach may constrain the signal deviations in a larger solution space than the NLS method. To reduce the residual, the NLS solver moves along the gradient descent direction. The algorithm tends to optimize the parameters that contributed the most to the model residual reduction and may remain at a saddle point since the parameter change is not always linearly continuous with

signal residuals. With a combination of parameter distribution and knowledge regularization, Bayesian regression self-adaptively updated the parameters. Despite the lower error obtained by the Bayesian method, advanced parameters like σ and D^* are observed with greater errors for all estimators. This result is consistent with the finding given in the literature that the D* is sometimes associated with inflammation activity (Leitão et al., 2013). Sensitivity of the parameter estimation to noise and the use of b-values resulted in inaccurate parameter estimation.

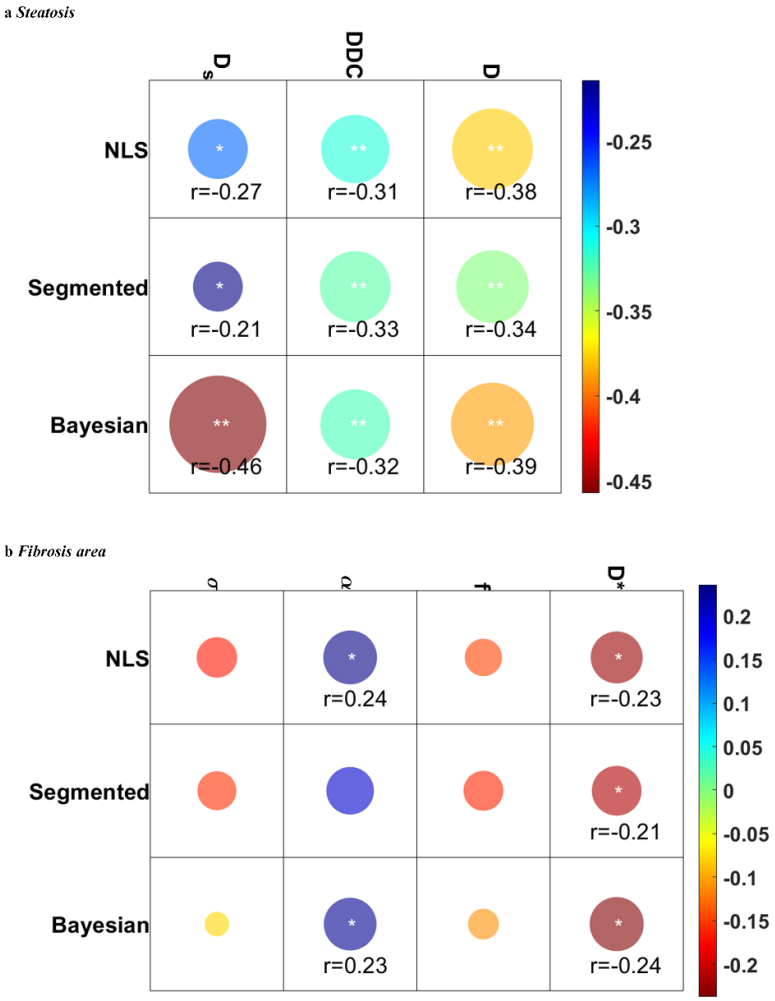

Fig. 4-3 Correlation of diffusion parameters with CLD histology biomarkers for (a) steatosis and (b) fibrosis (the color of the circle reflects the relevance, and the area of the circle reflects the significance; *p<0.05; **p<0.01), when no r-value is given, there is no significant correlation. A p-value <0.05 was considered statistically significant.

Abbreviations: NLS, Nonlinear least squares method

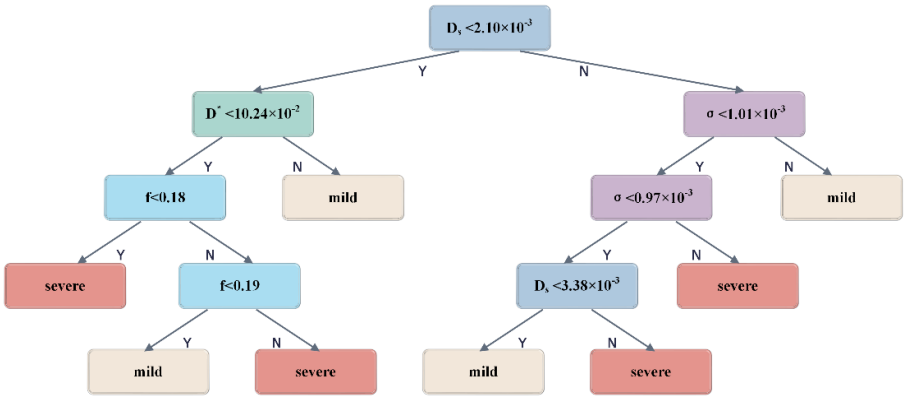

Fig. 4-4 Decision tree structure. The unit of parameters (Ds, σ, and D*) are mm^2/s.

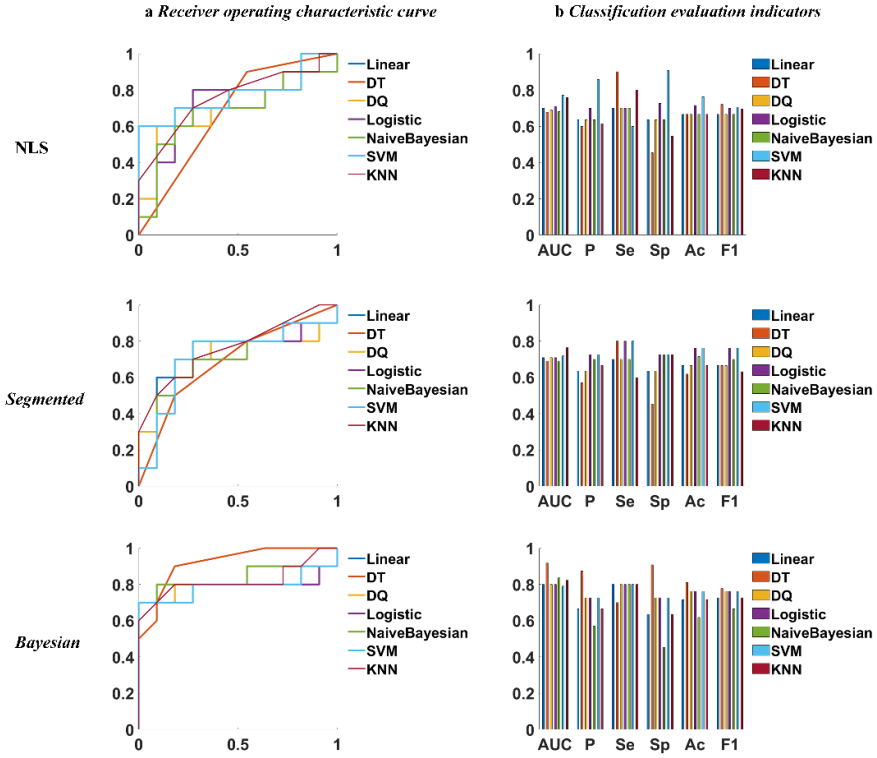

Fig. 4-5 Diagnostic values of diffusion parameters in the Classification of mild and severe fibrosis

Abbreviations: NLS, nonlinear least squares method; DT, Decision tree; QD, Quadratic discriminant; SVM, Support vector machine; KNN, K-nearest neighbor; AUC, area under the curve; P, precision; Se, sensitivity; Sp, specificity; Ac, Accuracy; F1, F1 score

Concerning the segmented method, which shared the same optimization algorithm as the NLS, the approximation made for the signals at each step could inevitably introduce systematic errors. In low-noise conditions, the segmented methods have lower accuracy than NLS in terms of signal or parameters. When additional noise becomes important, the segmented NLS method improved the accuracy of the statistical

diffusion model. This may partly demonstrate that the segmented NLS method may help obtain quality and correct estimations using the particular b-values at each step. In other words, the segmented NLS method improved the performance in comparison with the NLS method when parameters were difficult to estimate (i.e., are correlated) and in the presence of noise.

Since fibrosis can be accompanied by fat accumulation in CLD, we performed a correlation study to evaluate the confounding effect of fat on diffusion parameters in the assessment of fibrosis. As already found by other studies (Besheer et al., 2017; Lefebvre et al., 2021), we found a strong correlation between parameters related to isotropic limited diffusion and steatosis. This effect can be explained by the additional restriction of proton motion due to the fat vesicles. Indeed, all "pure" diffusion parameters fitted by the three methods decreased gradually with steatosis severity.

There was a significant correlation between perfusion-related diffusion parameters and fibrosis. In this *in vivo* study, diffusion parameters estimated with the Bayesian method could lead to differences between groups of patients with varying degrees of liver fibrosis. Statistically significant differences were observed for D_s, σ, D^*, and f values between patients with mild versus severe fibrosis using the Bayesian method. We also found that D_s values were significantly lower in the severe fibrosis group than in the mild fibrosis group. This finding may support the notion that both fibrosis and steatosis decrease the limited isotropic diffusion parameters, and fibrosis may impact the limited isotropic diffusion, non-Gaussian diffusion, and perfusion parameters in independent ways.

Several previous studies have focused on staging the grade of fibrosis associated with inflammation and steatosis (Besheer et al., 2017; Bouhrara et al., 2015; Lefebvre et al., 2021; Leitão et al., 2013; Yang et al., 2018) . The grading of fibrosis is difficult to guarantee when using only the ADC parameters (Shin et al., 2019). In the present study, D_s, σ, D^*, and f were used to train the variety of classifiers. For the classification between mild and severe fibrosis, the AUC of multiple classifiers used parameters computed with the Bayesian approach, has comparable values to the NLS-based method. In particular, the decision tree classifier achieved the best diagnostic performance with parameters fitted by the Bayesian method. This result may indicate that the accuracy of the fibrosis classification was also influenced by the estimation method. The parameters of each model tested individually were evaluated for their ability to classify fibrosis grade, but none of them provided better results than the

combination of parameters from different models in our data. In this regard, many studies have shown that some diffusion parameters can be used to stage liver fibrosis, but they were all conducted on the statistical level (as the first study on *in vivo* data of this contribution) and did not perform a classification task (Kim et al., 2019; Liang et al., 2018; Shin et al., 2019; Yang et al., 2018). The decision tree could allow us to get a clearer picture of the relevance of the different fitted parameters. Based on decision tree, D_s could be routinely monitored as a non-invasive screening reference for fibrosis. On the successfully found classifier, D_s have two nodes in 4 depth decision tree and appear at the head of the decision tree. The nodes closer to the root are more representative and understandable as well as the purity of the nodes are also related to the importance of features. For descendant nodes, the decision tree is not straightforwardly readable, given that it used a combination of different parameter level to refine the decision. For example, f values were used for classification on both layer 3 and layer 4. However, we have not found a significant correlation between fibrosis severity and σ values. This later result may support that some advanced parameters are non-linearly correlated with fibrosis severity. Despite the very good classification results achieved by the decision tree, 4 patients from the test set were not well-classified. In our data, the etiologies of CLD among patients were numerous and we suspect that for these patients impaired vascularization (for 1 misclassified patients), high level of steatosis (for 2 misclassified patient),or focal lesion (for 1 misclassified patient) may have had an impact on diffusion impedance, which was challenging for the classification.

4.4.1. Limitations

We did not consider the imaging gradient effect on low b-values in the simulation study. Indeed, this could be an additive source of signal fluctuation. Second, the cohort of patients was small including different etiologies of chronic liver diseases (such as nonalcoholic steatohepatitis [NASH], viral hepatitis, or alcoholic hepatitis), and it is known that the topography of fibrosis differs according to the etiology (peri-sinusoidal in viral hepatitis vs. centro-lobular in NASH) (Graupera et al., 2022). Consequently, in this work, the etiologies may have introduced some bias in the diffusion parameters for fibrosis evaluation Additionally, due to the limited dataset size, it was not possible to develop individual classifications for fibrosis grades using a complex classifier. Third, this study did not discuss the sampling choice of b-values. Indeed, the present work

focused on comparing different estimation approaches and diffusion function models for liver characterization. However, it can be shown that b-value sampling schemes impact the parameter fitting and thus their correlation with liver disease features. In order not to underestimate perfusion-related parameters, low b-values (0-50 s/mm^2) were used in this study as recommended in previous liver studies (Cohen, Schieke, Hohenwalter, & Schmainda, 2015; Y. T. Li et al., 2017). In the present study, due to insufficient signal-to-noise ratio (SNR), gradient strength value, and liver short T2 value, the MRI scanner was limited in the ability to obtain images at b-values greater than 800 s/mm^2. To keep the acquisition time short and to keep good SNR, DWI data were thus acquired with averages and with the maximum b-value set at 800 s/mm^2. Historically, the model capturing non-Gaussian behavior has been performed with high b-values, even has been reported as 2000 s/mm^2 (Yang et al., 2018). However, the Stat_D has never been applied to liver fibrosis and therefore the required b-values for this model is not fully established. Finally, spatial resolution may impact IVIM parameter values, particularly f and D^*. Indeed, when voxel size increases, the risk to include large vessels or biliary ducts due to the partial volume effect increases. In this context, another faster-decaying diffusion component may corrupt the bi-exponential model and a third component should be added. To address this issue, different approaches have been proposed. Gambarota et al. used a non-negative least squares (NLLS) analysis to determine the number of components in the NLSS spectrum and discarded the first b-values for the fitting step in voxels where three components were present (Gambarota et al., 2017). Another work has suggested to start IVIM modeling at b = 2 s/mm^2 instead of 0 (T. Li et al., 2019). Li et al. demonstrated that compared with IVIM analysis starting from b = 2 s/mm^2, IVIM analysis that included b = 0 s/mm^2 led to higher inter-subject variations among healthy young volunteers (T. Li et al., 2019). In addition, an increased sensitivity of IVIM in detecting liver fibrosis has been demonstrated when starting from b = 2 s/mm^2 (T. Li et al., 2019). Another group has suggested to acquire additional sets of very small b-values (typically between 0 and 20 s/mm^2) and performed a tri-exponential analysis (Chevallier et al., 2019). Thus, a future study investigating b-value sampling could be used to enhance the findings of the present work.

4.5.Conclusion

In this work, we compared three different fitting methods for the estimation of

diffusion parameters in terms of estimation accuracy and relevance for fibrosis evaluation. Based on this analysis, we trained a decision tree combining different advanced diffusion parameters computed with the Bayesian approach to predict severe fibrosis (F>2 based on the ISHAK classification) with an AUC of 0.92. Our results also demonstrate that the Bayesian approach improves the diagnostic performance of diffusion parameters for assessing liver fibrosis and may confirm the confounding effect of fat in the use of diffusivity (D) for assessing liver fibrosis.

Chapter 5 MRI Virtual Liver Biopsy

Using Radiomics Analysis for the Assessment of Chronic Liver Disease models (Original Article, submitted in JBHI)

Contents

5.1. Introduction

Chronic liver disease (CLD) is a leading cause of morbidity and mortality worldwide, accounting for an estimated two million deaths per year (Cheemerla & Balakrishnan, 2021). It includes a large variety of hepatic diseases that, in most subtypes, damage the liver in similar ways (Sharma & Nagalli, 2022). CLD progression may be characterized by histology with the presence of steatosis, inflammation, fibrosis, and iron overload regardless of the underlying etiologies (Chowdhury & Mehta, 2022). While liver biopsy is a prerequisite to histology, there is still an unmet medical requirement to characterize CLD in a non-invasive way (Chowdhury & Mehta, 2022). Among them， inflammation and fibrosis have emerged as two pivotal factors in that inflammation plays a role in the early liver fibrosis process (Gao & Tsukamoto, 2016), while fibrosis affects the CLD prognosis and treatment strategy (Roehlen et al., 2020).

To date, ultrasound (US) and Magnetic resonance imaging (MRI) are used for CLD diagnosis (Sutherland et al., 2017). Unfortunately, conventional imaging techniques are limited in assisting in the diagnosis of advanced CLD (Sutherland et al., 2017). With the development of elastography using both US and MRI, called transient elastography (Fibroscan) and magnetic resonance elastography (MRE) respectively, quantitative elastic properties related to fibrosis and inflammation can be estimated (Zhang et al., 2022). However, reliable Fibroscan or MRE examination requires an external device (to generate mechanical wave), experienced radiology, and careful analysis with fat content and iron overload (Chang, Goh, Ngu, Tan, & Tan, 2016). In practice, diagnostic performance is intricately linked to the radiologist's expertise and experience (Chang et al., 2016). Moreover, elastography is considered irrelevant in many studies for patients with early fibrosis and unreliable in overweight patients (Afdhal, 2012).In the literature, extensive evidence demonstrated the value of multiple MRI techniques in the assessment of fibrosis or inflammation. The T1 weighted (T1WI) and T2 weighted (T2WI) sequences may reflect disordered structure or microscopic changes in the tissue (Hoffman et al., 2020; Mesropyan et al., 2021). T2* mapping is able to evaluate the magnetic field inhomogeneities caused by iron overload (Heris et al., 2021); proton density fat fraction (PDFF) provides information about steatosis and fat content (Ye et al., 2019); Diffusion-weighted imaging (DWI) has the capability to assess fibrosis and is potentially associated with inflammation (Huang et al., 2023; Lefebvre et al., 2021; Y. X. J. Wang et al., 2021). Collectively, MRI has been considered a promising imaging modality for the diagnosis of CLD, thanks to multi-contrast and high spatial resolution quantitative protocols.

In addition, an emerging discipline known as radiomics has garnered growing attention in the detection of CLD (X. Lu et al., 2021; Song et al., 2020). The meaningful features were extracted, selected, and then used to assist in characterizing various histological features. In this study, we explored the performance of radiomics analysis for the evaluation of fibrosis and inflammation in CLD using images derived from conventional and advanced MRI acquisitions.

5.2.Materials and method

5.2.1. Patients

This study protocol was approved by the local ethics committee (CCP 2013-A00568-39). Seventy-seven patients (33 women, 44 men, mean age 48.9 ± 15.0 years; mean weight: 77.1 ± 16.6 Kg; mean height: 1.67 ± 0.09 m) with histology-proven CLD diseases were enrolled. The patients have one or more etiologies including viral hepatitis B, and C (VHB, n = 20, and VHC, n = 17); Non-alcoholic steatohepatitis (NASH, n = 19); and others (cholangiopathy; vascular diseases; steatosis; immune disorder; hemochromatosis, n = 17). All patients underwent biopsy and MRI acquisition with information and consent.

5.2.2. Liver biopsy

Biopsies were done using an 18 or 16 G biopsy needle via a transparietal approach to collect tissue samples. After being fixed by 10% neutral buffered formalin, the tissues were embedded in paraffin. The small portion of the liver was sectioned 4mm thick and was mounted on glass slides. Each section was stained with hematoxylin-eosin-saffron, iron stain, and Masson trichrome reagents. The histopathological evaluation was co-evaluated by two pathologists (VH) with more than 10 years of experience. The pathologists were blinded to any clinical information and MRI result. The steatosis and fibrosis percentages were calculated by the ratio of components on the slide with computerized morphometry. The inflammation was analyzed separately in the lesion region (portal or lobular) considering their respective degrees (portal: P=0: no, P=1: mild, P=2: severe; lobular: L=0: no, L=1: mild, L=2: severe).

The steatosis was classified into four grades with Brunt's score (S0: 0-5%, S1: 5-33%, S2: 33-66%, S3 >66%). The inflammation was classified into 3 grades (A0-A2, grade= max (P, L)). The fibrosis was stratified using the ISHAK score. The score is mainly related to fibrosis, but it is also related to the activity and presence of other

associated lesions (F0: no fibrosis, F1: some portal areas ± short fibrosis septa, F2: most portal areas± short fibrosis septa, F3: most portal areas + occasional portal to portal bridging, F4： most portal areas + marked bridging, F5: marked bridging + occasional nodules, F6: cirrhosis, probable or define).

The binary classification labels were set for fibrosis and inflammation (non significant fibrosis [F0–F2] vs. significant fibrosis [F3–F6], and no inflammation [A0] vs. hepatitis [A1–A2], respectively).

5.2.3. Image acquisition

The acquisition protocol included conventional T1WI with contrast agent gadobentate-dimeglumine (Gd-BOPTA) injection, T2WI, chemical shift encoded (CSE-MRI) - providing proton density fat fraction (PDFF) and T2*maps - and multiple b-value diffusion-weighted imaging (DWI). All MRI examinations were carried out at 3-Tesla (GE MR750, GE Healthcare, Chicago, IL, USA) with slices oriented in the transverse plane. The conventional MRI protocols consisted of 3D fat-suppressed LAVA FLEX T1WI sequence (TE/TRE =3.4/4.2 ms, slice thickness/ spacing between slices = 3.4/1.7 mm, field of view = 304× 304 mm2, flip angle = 15º, acquisition matrix = 320 × 224, reconstruction matrix = 512×512) and turbo spin echo T2WI PROPELLER sequence (TR/TE = 3157.9/113.1 ms, slice thickness = 4.0 mm, field of view = 400× 400 mm2, flip angle = 110 º, acquisition matrix = 384× 384, reconstruction matrix = 512×512)

Chemical shift-encoded multiple spoiled gradient recalled echo (SPGR) sequence with 4 echoes (TR/ TE = 100/ TE0: 1.1, TE1: 2.3, TE2: 3.6, TE3: 4.8 ms, slice thickness/ spacing between slices = 10.0/5.0 mm, field of view = 410× 410 mm2, flip angles = 5º, 15º, 30º, 45º, acquisition matrix = 128 × 128, reconstruction matrix = 256×256) was used to compute PDFF and T2* maps (Benjamin Leporq, Ratiney, Pilleul, & Beuf, 2013).

DWI was performed with spin-echo echo planar imaging (SE-EPI) enhanced diffusion-weighted imaging (TR/ TE = 2050.0/ 54.3 ms, slice thickness/spacing between slices =8.0/4.0 mm, field of view = 400 × 300 mm2, flip angle = 90º, acquisition matrix = 96 × 128, reconstruction matrix = 256×256). Twelve b-values (0, 10, 20, 40, 60, 80, 100, 200, 300, 400, 600, 800 s/ mm2) were acquired with a tetrahedral diffusion gradient encoding. The diffusion models including the mono-

exponential model (MONO), intravoxel incoherent motion (IVIM), stretched exponential model (SEM), statistical diffusion model (Stat_D), were fitted with nonlinear least square (NLS, for MONO), and Bayesian shrinkage approach with NLS initialization (for others model) in MATLAB 2019b (The MathWorks Inc., Natick, MA, USA) (Huang et al., 2023). The model and corresponding parameters were listed in Table 5-1.

The whole liver was manually segmented in two-dimension from a single slice located at the middle of the liver by JH and validated by BL.

Table 5-1 Diffusion-based MRI Model's Parameters And Their Function

Models	Parameters	Function
MONO	ADC (mm^2/s)	$\mathbf{S}_i = \mathbf{S}_0 exp(-\mathbf{b} \times ADC)$
Stat_D	Ds (mm^2/s) σ (mm^2/s)	$\mathbf{S}_i = \mathbf{S}_0 exp(-\mathbf{b} \times D_s + \frac{1}{2} \times \mathbf{b}^2 \sigma^2)$
SEM	DDC (mm^2/s) α	$\mathbf{S}_i = \mathbf{S}_0 exp[-(\mathbf{b} \times D)^{\alpha}]$
IVIM	f D (mm^2/s) D* (mm^2/s)	$\mathbf{S}_i = \mathbf{S}_0[(1-f) exp(-\mathbf{b} \times D) + f \times exp(-\mathbf{b} \times D^*)]$

Table 5-2 Clinical Characteristics of Patients in Training and Testing Sets by Fibrosis and Inflammation

Target	Characteristics	Mild	Severe	p-value
Fibrosis	**Sex**			*
	Male	18	26	
	Female	23	10	
	Age			0.976
	Mean	48.85	48.89	
	Std	13.85	16.32	
	BMI			0.68
	Mean	27.44	27.85	
	Std	5.58	5.85	
	Clinical etiology			
	NASH	7	12	0.12
	Hepatitis B	11	9	1.00
	Hepatitis C	6	11	0.11
	Others			
	Alcohol	1	2	0.60
	Liver transplant	6	1	0.11

	Inflammation			**
	No	18	5	
	A1-A2	23	31	
	Sex			0.80
	Male	14	30	
	Female	9	24	
	Age			0.49
	Mean	50.17	48.31	
	Std	15.79	14.70	
	BMI			0.33
	Mean	26.66	28.9	
	Std	5.53	5.74	
Inflammation	**Clinical etiology**			
	NASH	6	13	1.00
	Hepatitis B	4	16	*
	Hepatitis C	5	13	*
	Others			
	Alcohol	1	2	
	Liver transplant	3	4	1.00
	Fibrosis (Ishak)			**
	F0-F2	18	23	
	F3-F6	5	31	

The student t-test was used to compare the difference in age and BMI and Fisher's exact test was used to compare the difference in other characters. (*P < 0.05; **P < 0.01)

5.2.4. Radiomic feature extraction

Radiomic feature extraction was carried out using the Pyradiomics toolbox (in Python version 3.7) (Van Griethuysen et al., 2017). For preprocessing, all MRI parameters including T1WI, T2WI, b=0 diffusion image (B0), PDFF, T2*-maps, and diffusion parametric maps (eight maps, listed in Table 5-1) were normalized with z-score. Then, ninety-four features (first-order statistics: 19, gray level co-occurrence matrix: 24, gray level run length matrix: 16, gray level size zone matrix neighboring: 16, gray-tone difference matrix: 5, gray level dependence matrix: 14) were extracted from original normalized images and wavelet decomposed images (eight decompositions). As a result, a total of $94 \times 13 \times 9 = 10998$ features were extracted for each patient.

5.2.5. Feature selection and reduction

To avoid curse of dimensionality problem, a features reduction method has been implemented using scikit-learn. First, unsupervised principal component analysis (PCA) was adopted to select sixty features with low redundancy features per contrast. Second, for each classification tasks, (inflammation or significant fibrosis), the supervised Fisher method was used to discard up to 20 features with both small intra-

class differences and large inter-class differences per modality. Finally, the desired features contributing to classification are determined by the support vector machines-recursive feature elimination (SVM-REF) method. The maximal number of features was set as 15 for inflammation classification, and 20 for fibrosis classification in single and multiple sequences model construction. For inflammation classification task, the dataset was resampled by adaptive synthetic (ADASYN) algorithm to balance the numbers of the patient in two groups. To properly adapt to the classification task, the features numbers and modalities combination were iteratively tuned from a few to more.

5.2.6. Models' construction

Patients were divided into training (75%) and test sets (25%) according to inflammation grades or fibrosis grades by stratified strategy. Random Forest Classifier (RFC) with scikit-learn was constructed on the training data with stratified k-folders cross-validation (k=5). The optimized classifier with minimal features and modalities combination was determined on the training dataset. For CSE and diffusion sequences, the RFC was trained with one or more features extracted from the maps in this sequence. In each combination, grid searching was used to find optimal hyperparameters. The best RFC with optimized hyperparameters was retraining in k-folders and k classifiers were built. Then the performance of k classifiers was both validated on the training and test dataset.

5.2.7. Statistical analysis and diagnostic performance

Fisher's exact test and student-t test were used to compare the difference in categorical and continuous variables in the clinical characteristics of patients, respectively. The ROC curves and AUC analysis were plotted to assess and compare the quantitative performance both on the training dataset and test dataset. The cutoff values provided a balanced combination of sensitivity and specificity were calculated on the training dataset. Further to quantitatively analyze the diagnostic performances of different combinations the accuracy, precision, sensitivity, and specificity were computed on training and test set at cutoff values. The AUCs of model trained from radiomics extracted from different images combinations were compared by the Delong test.

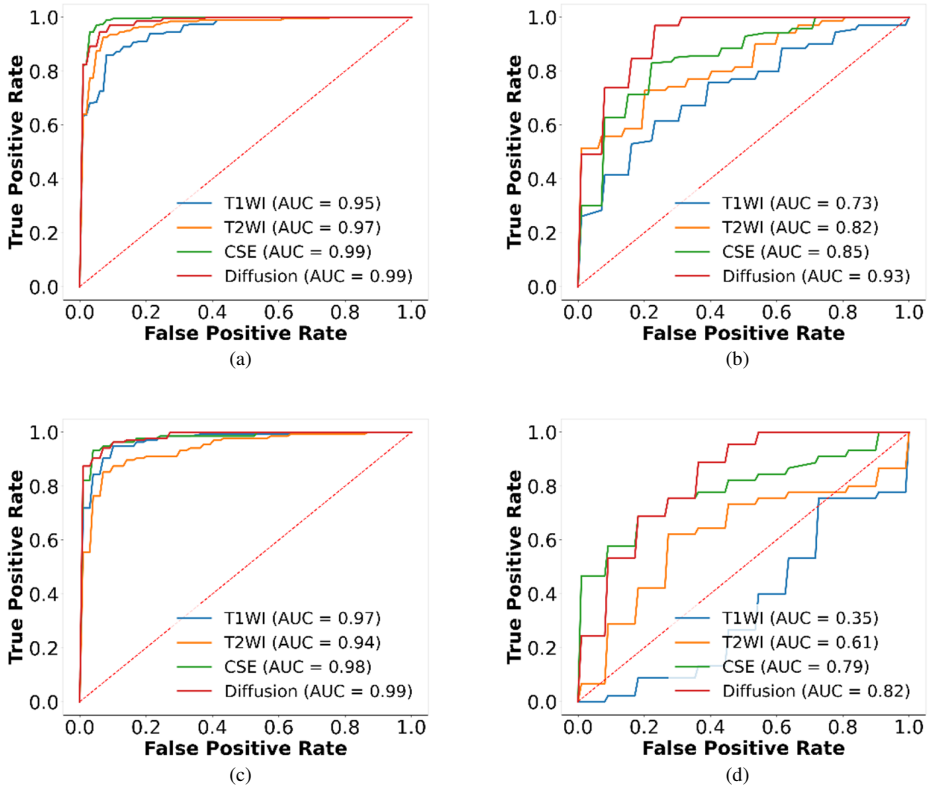

Fig. 5-1Comparison of ROC curves using a single sequence for the classification. (a) and (b) are ROC curves in case of inflammation classification for training and test set. (c) and (d) are ROC curves in case of fibrosis classification for the training and test set.

5.3. Results

5.3.1. Clinical characteristics

The baseline characteristics of patients are summarized in Table 5-2. Even though inflammation and fibrosis are distinct processes, they can be distinguished ($p<0.01$) from each other considerably. In our cohort, viral hepatitis constitutes a higher proportion of patients with inflammation.

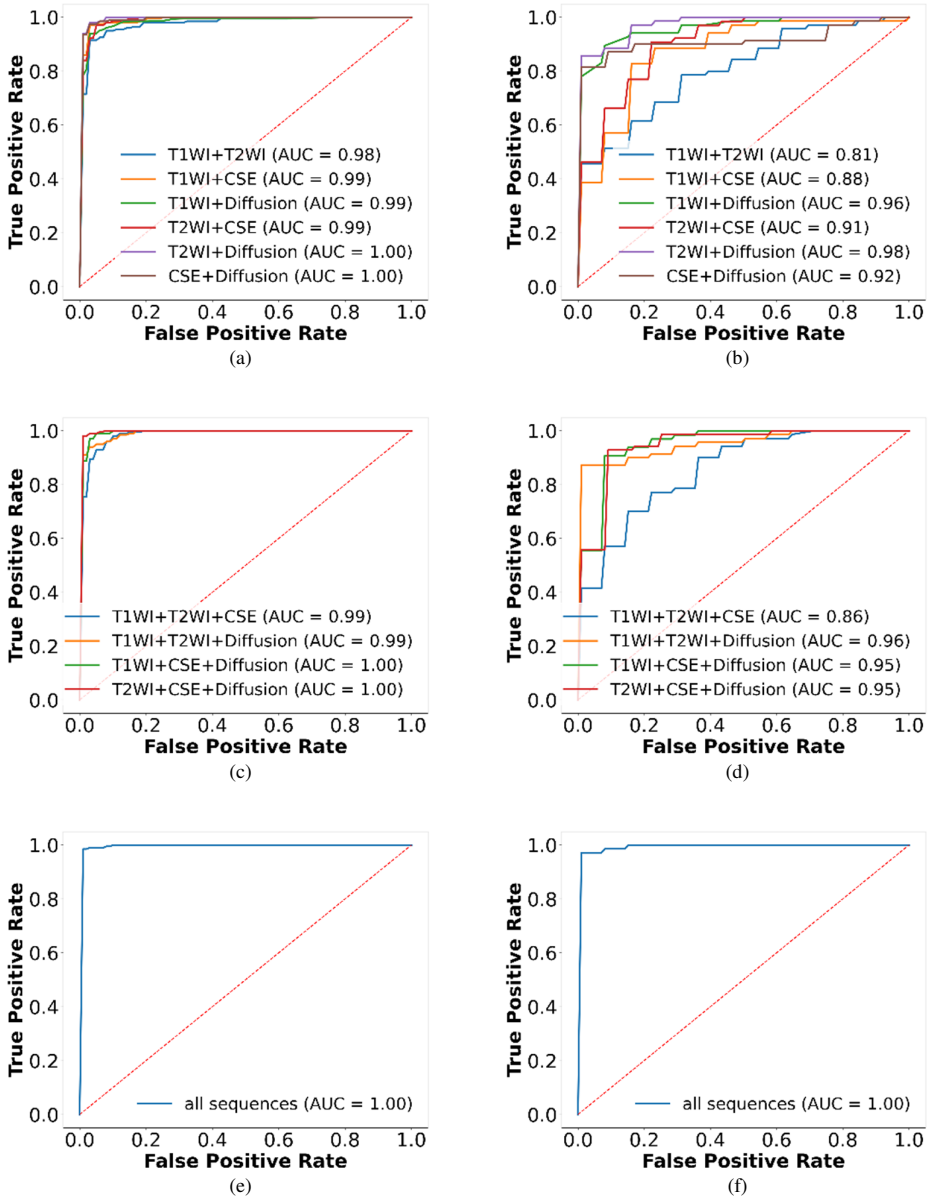

Fig. 5-2 Comparison of ROC curves of multiple sequences for inflammation classification. (a) and (b) are ROC curves with two sequences in the training and test set. (c) and (d) are ROC curves with triple sequences in the training and test set. (e) and (f) are ROC curves with all sequences in the training and test set.

5.3.2. Comparison of features extracted from a single sequence for inflammation or fibrosis

For inflammation classification, radiomics extracted from PDFF and a combination of diffusion parameters {f, D*,σ, ADC, B0} provided the best performances: AUC (training set :0.99; test set: 0.94) compared to other combinations within the sequence.

Meanwhile, PDFF and a combination of diffusion parameters {DDC, Diffusion, Ds} achieved an AUC of (training set: 0.98; test set: 0.81) for fibrosis.

For the construction of further multiple sequences, the terms “CSE combination” and “diffusion combination” refer to the parameter combinations in last sentence. These combinations result in the highest AUC values obtained during single sequence constructions for inflammation or fibrosis. Fig. 5-1a-d shows the ROC curves of the aforementioned sequence for fibrosis or inflammation in the training and test set. In addition, the cut-off value was decided in the training set. For each classification task, the quantitative metrics (accuracy, precision, sensitivity, specificity) at corresponding cut-off values were calculated as shown in Table 5-3. In the case of the fibrosis multiple combination model, the T1WI sequence was excluded from the construction of the multiple sequences model because its AUC dropped below 0.5.

Table 5-3 Performance of Single Sequence Model

Target	Cohort	Sequence	AUC(%)	Acc(%)	Preci(%)	Sen(%)	Spe(%)	F1	Cut-off(%)
Inflammation	Training	T1WI	95 (93-97)	90 (87-94)	93 (88-100)	88 (82-95)	93 (87-100)	90 (88-94)	52 (44-60)
		T2WI	97 (96-99)	94 (90-95)	93 (87-97)	94 (90-95)	93 (87-97)	93 (86-98)	51 (40-58)
		CSE(PDFF)	**99 (99-100)**	97(95-100)	95 (91-100)	**99 (97-100)**	95(90-100)	97 (95-100)	41 (33-45)
		Diffusion (DDC+σ+D+D*)	99 (97-100)	97 (95-100)	**97 (93-100)**	97 (93-100)	**97 (92-100)**	97 (95-100)	52 (45-57)
	Test	T1WI	73 (66-83)	68 (59-74)	69 (58-77)	73 (64-79)	63 (38-77)	70 (67-74)	-
		T2WI	82 (73-86)	74 (62-79)	78 (58-100)	71 (50-79)	**77 (47-100)**	73 (67-79)	-
		CSE(PDFF)	85 (78-94)	76 (64-86)	76 (62-92)	79 (71-86)	73 (57-93)	77 (67-85)	-

Fibrosis	Training	Diffusion (DDC+σ+D+D*)	**93 (89-96)**	**82(69-88)**	**78 (62-92)**	**94 (85-100)**	71 (38-92)	**85 (76-89)**	-
		T1WI	97 (94-99)	94 (89-96)	93 (89-100)	94 (89-100)	93 (90-100)	93 (89-96)	51 (40-63)
		T2WI	94 (90-97)	90 (88-95)	90 (84-96)	90 (81-96)	91 (82-97)	90 (86-94)	51 (42-60)
		CSE(PDFF+T2*)	98 (95-99)	**96 (95-98)**	**96 (93-100)**	95 (93-96)	**97 (93-100)**	**96 (94-98)**	51 (42-60)
		Diffusion (DDC+σ+D+D*)	**99 (98-99)**	95 (93-98)	94 (87-100)	97 (93-100)	94 (87-1)	95 (93-98)	48 (39-56)
	Test	T1WI	35 (25-46)	41 (30-60)	29 (0-55)	33 (0-67)	47 (27-64)	30 (0-60)	-
		T2WI	61 (49-68)	59 (50-70)	55 (40-67)	56 (22-78)	62 (27-82)	53 (29-67)	-
		CSE(PDFF)	79 (68-92)	**75 (65-90)**	**79 (58-100)**	64 (44-89)	**84 (55-100)**	69 (53-89)	-
		Diffusion (DDC+σ+D+D*)	**82 (77-90)**	71 (65-80)	75 (57-100)	**67 (33-89)**	75 (45-100)	66 (50-80)	-

5.3.3. Diagnostic performances of models training from different radiomics features combination for the classification of liver fibrosis and inflammation

The RFC was then trained by combining features extracted from different images from two to multiple sequences. ROC curves illustrating the diagnostic performances for the classification of fibrosis and inflammation are shown in Fig. 5-2 a-f and Fig. 5-3 a-d. The performances of different combinations evaluation were provided in Table 5-4. Besides, a combination of {T1WI, T2WI, CSE, Diffusion} and {T2WI, CSE,

Diffusion} performed best on inflammation (AUC: training 1.00; test 1.00) and fibrosis (AUC: training 0.99; test 0.89) respectively.

Given that inflammation is significantly associated to fibrosis, we also trained an integrated model taking into account the probability score of inflammation predicted by the best inflammation classifier and radiomics features extracted from three MRI sequences (T2WI, CSE, and DWI). The performance of the integrated model was obviously increased than the MRI-only model (AUC training set: 0.99; AUC test set 0.97) with only 14 features (13 MRI features+ inflammation likelihood).

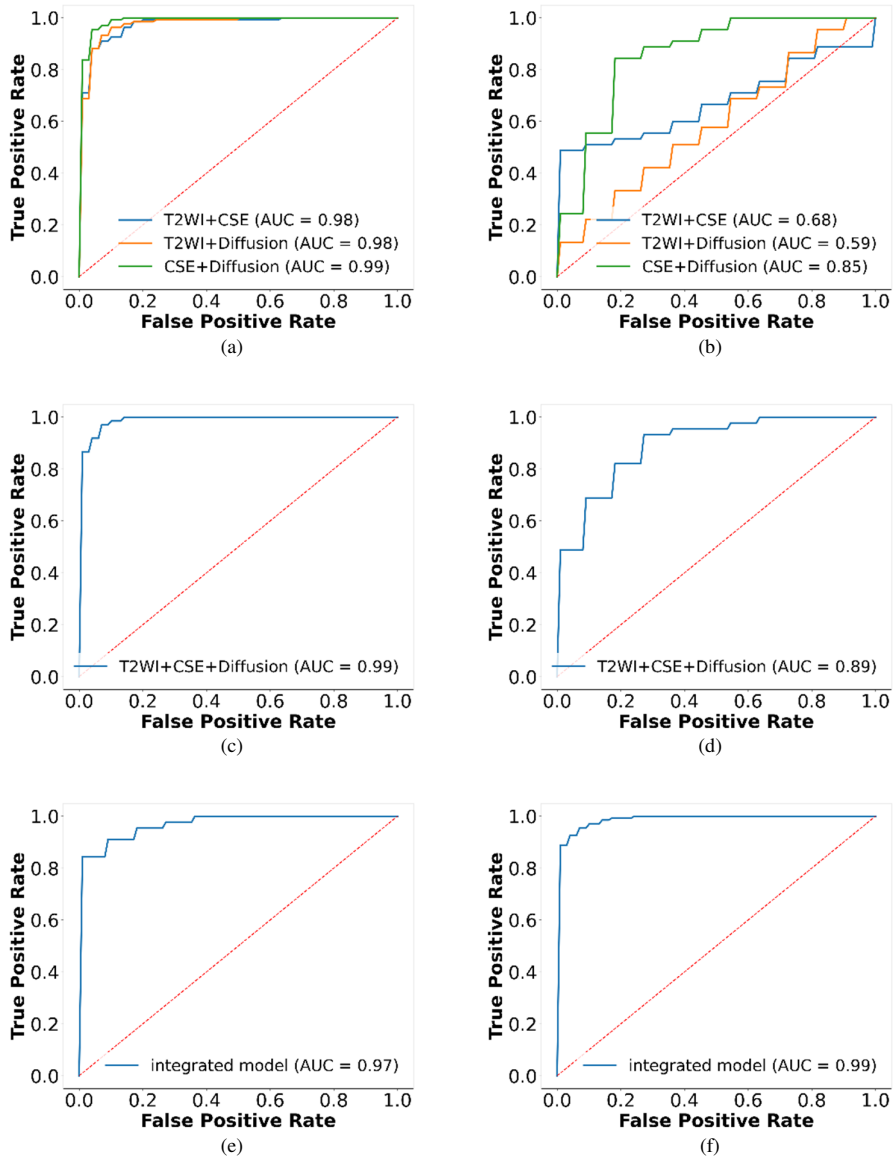

Fig. 5-3 Comparison of ROC curves of multiple sequences for fibrosis classification. (a) and (b) are ROC curves with two sequences in the training and test

set. (c) and (d) are ROC curves with triple sequences in the training and test set. (e) and (f) are ROC curves with triple sequences and inflammation prediction scores in training and test set.

5.3.4. Comparison of multiple sequences and single sequence models

The Fig. 5-4, summarized the Delong test p-values computed used to compare the classifiers built from radiomics extracted from a single sequence and from a combination of multiple sequences. In Fig. 5-4 a-b, RFC built with radiomics extracted from diffusion parameters displayed improved performances than others for both inflammation and fibrosis (except the CSE in fibrosis classification). In Fig. 5-4 c-d, the models built with all sequence's combination provided better diagnostic performances compared to other sequences for both inflammation and fibrosis.

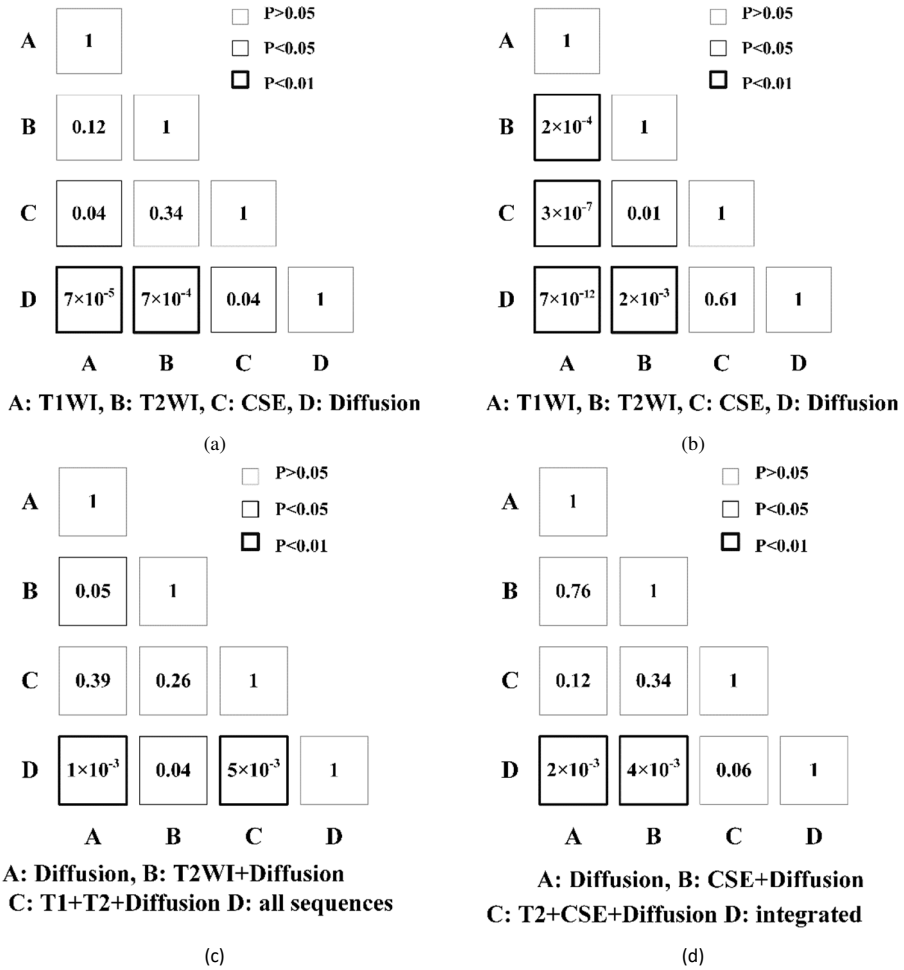

Fig. 5-4 Delong test between different models. (a) and (b) are the Delong test p-values between ROC for inflammation and fibrosis classification models trained from radiomics extracted from a single MRI sequence. (c) and (d) are the Delong test p-

values between ROC for inflammation and fibrosis classification models trained with radiomics extracted from multiple sequences.

5.4. Discussion

In this retrospective study, we investigated radiomics analysis based on features extracted from one or more conventional MRI acquisitions (injected T1 weighted and fat-saturated T2 weighted) and parametric maps such as T2*, PDFF and diffusions maps computed from multiple b-values acquisition with different function models to classify inflammation and fibrosis in patients with CLD. In single sequence model construction, we found that the model built with features extracted from diffusion maps in significantly improved diagnostic performances in comparison with others for both fibrosis and inflammation assessment. When we add information from the combination of multiple sequences, the diagnostic performances were significantly improved. RFC built with multiple sequences or joined with inflammation regression score provided the best classification result for inflammation and fibrosis. The sensitivity and specificity of the multi-sequence model offered outstanding predictive performances and generalization in both the training and testing sets.

Our previous work has demonstrated that the diffusion parameters fitted by Bayesian were associated with fibrosis grades. (Huang et al., 2023). These previous results are consistent with ours in this present study where diagnostic performances of the models increased when radiomics features extracted from diffusion parameters map where included.

Table 5-4 The Performance of Multiple Sequences

target	cohort	Sequence	AUC (%)	Acc(%)	Preci (%)	Sen(%)	Spe(%)	F1	Cut-off(%)
Inflammation	Training	Tow sequences (CSE+Diffusion)	100 (100-100)	98 (96-100)	99 (97-100)	98 (93-100)	98 (97-100)	98 (96-100)	54 (42-65)
		Three sequences (T2+CSE+Diffusion)	99 (98-100)	96 (93-98)	92 (87-97)	98 (95-100)	95 (86-98)	96 (93-98)	50 (35-70)

		Four sequences (T2+CSE+ Diffusion+Inflam)	100 (100-100)	**99 (99-100)**	**100 (98-100)**	**99 (97-100)**	**100 (98-100)**	**99 (99-100)**	54 (45-65)
	Test	Tow sequences (CSE+Diffusion)	98 (96-100)	91 (81-96)	94 (87-100)	89 (71-100)	94(85-100)	91 (80-97)	-
		Three sequences (T2+CSE+Diffusion)	96 (94-97)	84 (79-96)	85 (70-100)	87 (57-100)	80 (57-100)	84 (73-96)	-
		Four sequences (T2+CSE+ Diffusion+Inflam)	**100 (98-100)**	**96 (89-100)**	**95 (82-100)**	**99 (93-100)**	94 (79-100)	**97(90-100)**	-
	Training	Tow sequences (CSE+Diffusion)	99 (98-100)	**97 (95-98)**	94 (90-96)	99 (96-100)	95 (90-97)	**97 (95-98)**	45 (39-51)
		Three sequences (T2+CSE+Diffusion)	99 (99-100)	95 (93-96)	92 (87-93)	99 (96-100)	92 (87-93)	95 (93-96)	42 (37-50)
Fibrosis		Four sequences (T2+CSE +Diffusion+Inflam)	99 (98-100)	96 (93-100)	**95 (87-100)**	98 (89-100)	95 (87-100)	96 (93-100)	48 (40-55)
	Test	Tow sequences (CSE+Diffusion)	85 (78-90)	76 (65-85)	69 (56-75)	89 (67-100)	65 (36-82)	77 (71-86)	-
		Three sequences (T2+CSE+Diffusion)	89 (80-95)	81 (75-90)	73 (67-82)	**91 (78-100)**	73 (64-82)	81 (74-90)	-

Four sequences (T2+CSE+ Diffusion+Inflam)	**97 (94-100)**	**83 (75-90)**	**85 (67-100)**	80 (67-89)	**85 (64-100)**	81 (76-88)	-

Recently, MRI imaging of inflammation in the liver has been studied. To detect the inflammation at the microscopic level, targeting of immune cells was mostly done with magnetic nanoparticles with T2 MRI applications (Hammoud, 2016). More recently, T1WI and T2WI with a high magnetic field (7 Tesla) presented a significant correlation with inflammation in animal study (Arihara et al., 2022). So far, there is still a lack of validated diagnostic imaging criteria for inflammation in human studies. In this study, the classifiers trained from the combination of T1WI, T2WI, PDFF, T2*, and Diffusion maps, have demonstrated promising performances to classify key histological features such as fibrosis and inflammation. By comparing the different performances of the models, an RFC built with diffusion parameters provided 93% AUC although it has been shown in previous studies that diffusion parameters were not correlated with inflammation. This result may indicate that the radiomics features could capture the histological heterogeneity at microstructure texture. (usually less than 1 cm, (Ros, 2018)). To our knowledge, it is the first study that successfully classified the liver inflammation grade in patients with multiple etiologies.

In general, the AUC of almost all classifiers built from MRI-only sequences constructed for inflammation was higher than for liver fibrosis classification. The reason could be that fibrosis is a pathology process synergized by multifactorial effects. Mostly, inflammation represented a prominent predisposing factor that trigged an aberrant healing process (de Boer et al., 2019). However, fibrosis triggered by inflammation is a classical fibrosis development assumption. In literature, fibrosis has been demonstrated that it is also concomitant with iron deposition, steatosis (Oeda et al., 2020; Shendge, Panja, Basu, Ghate, & Mandal, 2021).. As a result, the feature sizes were adaptively set to 15 for inflammation and to 20 for fibrosis to adapt to the problem's complexity. More specifically, the lipotoxicity caused by inflammation and steatosis activates hepatic stellate cells that promote the fibrogenic phenotype and fibrosis (Gaul et al., 2021; B. Leporq, Lambert, Ronot, Vilgrain, & Van Beers, 2017). When the liver attempts to regenerate the damaged cells, stellate cells are activated to differentiate into myofibroblasts (Gressner, 1996). Myofibroblasts secreted some

proteins to the extracellular environment. With the accumulation of extracellular matrix, scarring tissue begins and replaces the normal tissue in some populations. The process of fibrosis may continue for decades, 10% to 30% of people may have some degree of iron overload (Kowdley, 2016). On top of that, it is known that iron overload is an important factor that contributes to fibrosis and could be interesting to take into account in fibrosis classification. Therefore, these complex mechanisms inspired us to build a non-end-to-end model. This cascade classification built with {T2WI, PDFF, T2*, Diffusion sequence, inflammation} obviously improved classifier performance. This combination can be interpreted as follows. T2* could probe iron overload (Positano et al., 2009). As the presence of steatosis is a confounding factor for fibrosis evaluation using diffusion MRI, adding its measurement thanks to CSE-derived PDFF (a nowadays recognized imaging marker of steatosis (Caussy et al., 2018)) to diffusion-related parameters could help fibrosis classification. Moreover, evaluated T2WI with liver fibrosis may be associated with an elevated inflammatory component which has been seen in chronic hepatitis and steatohepatitis. The inflammation likelihood offered complementary information. The combination of T2WI feature and inflammation index making it beneficial for fibrosis identification (Guimaraes et al., 2016). Overall, the final joint model has used all known fibrosis-related features.

There were some limitations to our study. First, the dataset was not fully balanced for both inflammation and fibrosis. Especially for inflammation, we had to resample the data for inflammation, that could result in overly optimistic classification results. Second, if the pan-etiologies aspect of our cohort is interesting since it may increase the model robustness regarding chronic liver disease heterogeneity, the population size for each etiology in our cohort remains modest. It is known that there is a topography difference in fibrosis deposition between NASH and viral hepatitis. Model inferences in several validation cohorts including only NASH and only viral hepatitis are mandatory to evaluate models' stabilities. Third, the MRI protocol acquisition used in the study is not conventional, particularly for the use of chemical shift encoded MRI and multiple b-value acquisition. We acknowledge that it may constitute an additional limitation for dissemination purposes and require a standardization initiative. However, to date, CSE-MRI and multiple b-values pulse sequences are available in numerous MR systems.

Chapter 6 Conclusion and perspectives

Contents

6.1 Conclusions

In this thesis, we aimed to investigate the relationship between fibrosis and inflammation in CLD and multiparametric MR images and to classify CLD features based on radiomics. All this work benefited from MRI acquisitions carried out prior to the thesis to provide a data base that, while limited in number, still enabled sufficient classification tests, as presented in the two major contributions of this research work. In order to study the CLD disease process and further link the multiparametric maps and CLD features, we first theoretically introduced the description of CLD physiopathology and histology and the multiparametric MRI sequence and principle. With quantitative DWI only methods, we have demonstrated that it is possible to classify liver fibrosis into severe and mild groups. To avoid the effect of the confounding effect of fat in molecular diffusion, multiple parametric maps were then used to build more robust classifiers for both inflammation and fibrosis.

Our main contributions are in the following areas:

a. A comparative study between different fitting approaches and diffusion models

The methodology presented in this manuscript, the main results of which are summarized below, is the result of a long process of comparison and questioning linked to several difficulties specific to this thesis topic; parameter adjustment, signal modeling, simulated vs in vivo data, limited data base (particularly in this field since MRI is only indicated for the follow up of hepatocellular carcinoma, in cirrhotic patients).

The development of parametric adjustment methods for diffusion signals required initial work on simulated data, followed by comparison with real data. Indeed diffusion signal decay can be modeled in different ways and several models statistical models (Stat_D), stretched exponential model (SEM), and intravoxel incoherent motion (IVIM) were studied. The corresponding parameters (Ds, σ, DDC, α, f, D, D*) were estimated on simulation and in vivo data using the nonlinear least squares (NLS), segmented NLS, and Bayesian methods. Given the model can be rather complex, the fitting strategy becomes highly significant. The fitting accuracy was analyzed on simulated Rician noised DWI. *In vivo*, the parameters were averaged from five central slices of the entire segmented liver to compare correlations with histological features

(inflammation, fibrosis, and steatosis). Then, the differences between mild (F0-F2) or severe (F3-F6) groups were compared respecting to statistics and classification. 75.3% of patients were used to build various classifiers (stratified split strategy and 10-folders cross-validation) and the remaining for testing. In simulation, the Bayesian method provided the most accurate parameters. *In vivo*, the highest negative significant correlation (Ds, steatosis: r=-0.46, D*, fibrosis: r=-0.24) and significant differences (Ds, σ, D*, f) were observed for Bayesian fitted parameters. Fibrosis classification was performed with an AUC of 0.92 (0.91 sensitivity and 0.70 specificity) with the aforementioned diffusion parameters based on the decision tree method. Thus, our conclusions are based on both simulation and in vivo data and are consistent in saying that Bayesian they indicate that Bayesian fitted parameters applied to diffusion data and associated to decision tree offers good properties to provide noninvasive diagnostic indicator of the degree of liver fibrosis.

b. MRI Virtual Liver Biopsy Using Radiomics Analysis for the Assessment of Chronic Liver Disease

Our objective was to investigate whether radiomics features extracted from individual or combined magnetic resonance imaging (MRI) contrasts, such as T1-weighted imaging, T2-weighted imaging, and quantitative maps from chemical shift encoded, and diffusion-weighted imaging, can effectively classify CLD's characteristics, specifically targeting inflammation and fibrosis. Seventy-seven patients with CLD were respectively enrolled in this study. Each participant underwent both MRI examinations and liver biopsy. Radiomic features were extracted, selected and reduced to reduce curse of dimensionality effect, and used to train the inflammation and fibrosis classification models. The performances of all classifiers were evaluated by the receiver operating characteristic curve (ROC), accuracy, precision, sensitivity, specificity. Comparisons between the different models were done by comparing their AUROC using the DeLong test. The model built using a random forest classifier trained from features selected from all the above-mentioned MRI sequences achieved the best area under the curve (AUC) for inflammation (training:1.00, test 1.00). The best model for fibrosis (training: 0.99, test 0.97) was obtained by a model combining the inflammation prediction score and radiomics extracted from three MRI sequences. This study demonstrated that the MRI-based radiomics features hold potential in the

inflammation and fibrosis classification on CLD's patients, independently of the etiology of the disease.

6.2 Perspectives

In the work aiming to compare different estimation approaches and diffusion function models for liver fibrosis assessment, we haven't presented the effect of b-values on the fitting results while some work has been conducted on this during this PhD thesis. First, DKI and full model were excluded due to the b-values range. In clinical trials, kurtosis-related parameters are typically recommended to fit with b-values of 1200 or higher (Zhou et al., 2019). However, there is no direct evidence to demonstrate the kurtosis effect can not be decomposed with lower b values (0-800 in our study). We found that kurtosis-related parameters were overestimated with more than 20% error in simulation. The amplitude changes in high b-values due to gradient or noise caused the signal to asymptotically approach zero more slowly than kurtosis. Secondly, a more appropriate b-value scheme and correction of T2 effect on the perfusion fraction f and partial volume effect of large vessel might allow more acccurate analysis of the different pools the different pools in the tissues. In general, the overall results depend on the data and MRI protocol achieved on the patients. With improvements in MRI techniques and acquisition parameters, we are confident that the results presented here can be further improved.

Moreover, we mentioned that MR elastography is an important diagnostic tool for fibrosis: we did not compare the effectiveness of MR elastography or even other MRI technique, because not available (MRE) or due to exam duration limitation. The development and deployment of MR elastography at clinical level could certainly be a plus in the multiparametric approach to CLD diagnosis. Additionally, some serum markers (Alanine transaminase, Aspartate transaminase, etc…) may hold the potential to distinguish between the progression of fibrosis and inflammation. By incorporating these additional insights, there is undoubtedly potential to devise a more cost-effective and efficient diagnostic protocol for CLD diagnosis. Serum tests and MRIs were performed, but serum biomarkers were excluded from the construction of the classifier given their insignificant correlation with CLD, and their nonsensitivity. Within the confines of this study, the dataset under consideration may be deemed modest in scale and may have the risk of reducing the model's credibility. The interpretability and reproducibility of the study for small samples are still in doubt. Nevertheless, its

intrinsic value is about validating MRI models in CLD applications. The paucity of available data emanates from the non-routine integration of Magnetic Resonance Imaging (MRI) in the clinical evaluation of CLD, a circumstance further exacerbated by the infrequency of liver biopsies due to their invasive nature. This scarcity of data imparts a heightened significance to the study, the uses of MRI in CLD were validated. Recognizing the inherent challenges associated with limited data, a methodologically rigorous approach was adopted to address this constraint. A meticulous stratification strategy was implemented to ensure comparability in data distributions between the primary dataset and the validation set. Concurrently, deliberate adjustments to model hyperparameters, encompassing the minimum number of trees, maximum tree layers, and branch reduction within the context of the random forest framework, were undertaken. These methodical interventions were orchestrated to preserve model simplicity while concurrently avoiding overfitting problems. Thus, the undertaken measures reflect a steadfast commitment to glean meaningful insights from the constrained yet invaluable dataset in question.

Returning to the original question, is liver biopsy destined to remain the undisputed gold standard? It's conceivable that in the future, MRI could surpass liver biopsy in diagnostic efficacy. This potential shift could be attributed to MRI's capability to examine each liver slice with enhanced precision. Unlike liver biopsy, which has inherent limitations such as invasiveness and potential complications, MRI offers the advantage of non-invasiveness and the ability to provide a comprehensive and detailed view of the liver's internal structure. This contrast in approach may lead to MRI becoming a preferred diagnostic tool, particularly as technology continues to advance.

Author's publications

Articles in peer-reviewed international journals

[1] Jiqing Huang, Benjamin Leporq, Valérie Hervieu, Jérôme Dumortier, Olivier Beuf, and Hélène Ratiney. "Diffusion-Weighted MRI of the Liver in Patients With Chronic Liver Disease: A Comparative Study Between Different Fitting Approaches and Diffusion Models." *Journal of Magnetic Resonance Imaging* (2023).

[2] Jiqing Huang, Benjamin Leporq, Valérie Hervieu, Sophie Gaillard, Jérôme Dumortier, Olivier Beuf, and Hélène Ratiney. "MRI Virtual Liver Biopsy Using Radiomics Analysis for the Assessment of Chronic Liver Disease, submitted in Journal of Biomedical and Health Informatics

Oral or poster presentations at conferences

[1] Jiqing Huang, Benjamin Leporq, Olivier Beuf, Hélène Ratiney "Chronic liver disease: The role of multiple diffusion-weighted models using the Bayesian shrinkage method for liver fibrosis assessment", ISMRM, Conference, Toronto, Canada，(2023)

[2] Jiqing Huang, Benjamin Leporq, Olivier Beuf, Hélène Ratiney "Optimization of b-values sampling scheme for several diffusion-weighted MRI models in the liver", ISMRM, Conference, Vancouver, Canada， (2021)

[3] Jiqing Huang, Hélène Ratiney，Benjamin Leporq, Olivier Beuf "Méthodes destimation et modèles de diffusion avancés pour l'évaluation de la fibrose hépatique dans les maladies chroniques du foie", SFRMBM, Paris, France, (2023)

[4] Jiqing Huang, Hélène Ratiney，Benjamin Leporq, Olivier Beuf "Comparison of Fitting Approaches for Diffusion-weighted MRI Models in Liver Simulation", SFRMBM, Lyon, France, (2021)

[5] Jiqing Huang, Benjamin Leporq, Olivier Beuf, Hélène Ratiney "Estimation of intravoxel incoherent motion (IVIM)- Kurtosis diffusion-weighted imaging and its application in liver", Journées RMN du Grand Sud, Clermont-Ferrand, France, (2021)

Bibliographies

Abd El Rihim, A. Y., Omar, R. F., Fathalah, W., El Attar, I., Hafez, H. A., & Ibrahim, W. (2013). Role of fibroscan and APRI in detection of liver fibrosis: a systematic review and meta-analysis. *Arab Journal of Gastroenterology*, *14*(2), 44–50.

Afdhal, N. H. (2012). Fibroscan (transient elastography) for the measurement of liver fibrosis. *Gastroenterology & Hepatology*, *8*(9), 605.

Alberti, K. G. (2009). International diabetes federation task force on epidemiology and prevention; hational heart, lung, and blood institute; American heart association; world heart federation; international atherosclerosis society; international association for the study of o. *Circulation*, *120*, 1640–1645.

Anderson, S. W., Barry, B., Soto, J., Ozonoff, A., O'Brien, M., & Jara, H. (2014). Characterizing non-gaussian, high b-value diffusion in liver fibrosis: Stretched exponential and diffusional kurtosis modeling. *Journal of Magnetic Resonance Imaging*, *39*(4), 827–834.

Angulo, P., Hui, J. M., Marchesini, G., Bugianesi, E., George, J., Farrell, G. C., … Bida, J. P. (2007). The NAFLD fibrosis score: a noninvasive system that identifies liver fibrosis in patients with NAFLD. *Hepatology*, *45*(4), 846–854.

Angulo, P., Kleiner, D. E., Dam-Larsen, S., Adams, L. A., Bjornsson, E. S., Charatcharoenwitthaya, P., … Stahler, A. (2015). Liver fibrosis, but no other histologic features, is associated with long-term outcomes of patients with nonalcoholic fatty liver disease. *Gastroenterology*, *149*(2), 389–397.

Annet, L., Peeters, F., Abarca-Quinones, J., Leclercq, I., Moulin, P., & Van Beers, B. E. (2007). Assessment of diffusion-weighted MR imaging in liver fibrosis. *Journal of Magnetic Resonance Imaging: An Official Journal of the International Society for Magnetic Resonance in Medicine*, *25*(1), 122–128.

Arihara, N., Saito, S., Sawaya, R., Onishi, R., Tsuji, K., Ohki, A., … Morimoto-Ishiwaka, D. (2022). Evaluation of liver T1rho and T2 values in acute liver inflammation models using 7T-MRI. *Magnetic Resonance Imaging*, *88*, 20–24. https://doi.org/https://doi.org/10.1016/j.mri.2022.01.010

Arjmand, A., Tsipouras, M. G., Tzallas, A. T., Forlano, R., Manousou, P., & Giannakeas, N. (2020). Quantification of liver fibrosis—A comparative study. *Applied Sciences*, *10*(2), 447.

Artz, N. S., Hines, C. D. G., Brunner, S. T., Agni, R. M., Kühn, J.-P., Roldan-Alzate, A., … Reeder, S. B. (2012). Quantification of hepatic steatosis with dual-energy computed tomography: comparison with tissue reference standards and quantitative magnetic resonance imaging in the ob/ob mouse. *Investigative Radiology*, *47*(10), 603.

Bataller, R., & Brenner, D. A. (2005). Liver fibrosis. *The Journal of Clinical Investigation*, *115*(2), 209–218.

Bedogni, G., Bellentani, S., Miglioli, L., Masutti, F., Passalacqua, M., Castiglione, A., & Tiribelli, C. (2006). The Fatty Liver Index: a simple and accurate predictor of hepatic steatosis in the general population. *BMC Gastroenterology*, *6*(1), 1–7.

Bedossa, P., & Poynard, T. (1996). An algorithm for the grading of activity in chronic hepatitis C. *Hepatology*, *24*(2), 289–293.

Bennett, K. M., Schmainda, K. M., Bennett, R., Rowe, D. B., Lu, H., & Hyde, J. S. (2003). Characterization of continuously distributed cortical water diffusion rates with a stretched-exponential model. *Magnetic Resonance in Medicine*, *50*(4), 727–734. https://doi.org/10.1002/mrm.10581

Besheer, T., Razek, A., El Bendary, M., Abd El Maksoud, M., Elalfy, H., Zalata, K., … El Gilany, A.-H. (2017). Does steatosis affect the performance of diffusion-weighted MRI values for fibrosis evaluation in patients with chronic hepatitis C genotype 4. *Turk J Gastroenterol*, *28*(4), 283–288.

Bharwani, N., & Koh, D. M. (2013). Diffusion-weighted imaging of the liver: an update. *Cancer Imaging*, *13*(2), 171.

Blachier, M., Leleu, H., Peck-Radosavljevic, M., Valla, D.-C., & Roudot-Thoraval, F. (2013). The burden of liver disease in Europe: a review of available epidemiological data. *Journal of Hepatology*, *58*(3), 593–608.

Bouhrara, M., Reiter, D. A., & Spencer, R. G. (2015). Bayesian analysis of transverse signal decay with application to human brain. *Magnetic Resonance in Medicine*, *74*(3), 785–802.

Brown, R. (1828). XXVII. A brief account of microscopical observations made in the months of June, July and August 1827, on the particles contained in the pollen of plants; and on the general existence of active molecules in organic and inorganic bodies. *The Philosophical Magazine*, *4*(21), 161–173.

Brunt, E. M., Clouston, A. D., Goodman, Z., Guy, C., Kleiner, D. E., Lackner, C., … Leow, W. Q. (2022). Complexity of ballooned hepatocyte feature recognition: Defining a training atlas for artificial intelligence-based imaging in NAFLD. *Journal of Hepatology*, *76*(5), 1030–1041.

Bugianesi, E., McCullough, A. J., & Marchesini, G. (2005). Insulin resistance: a metabolic pathway to chronic liver disease. *Hepatology*, *42*(5), 987–1000.

Caballero, F., Fernández, A., Matías, N., Martínez, L., Fucho, R., Elena, M., … García-Ruiz, C. (2010). Specific contribution of methionine and choline in nutritional nonalcoholic steatohepatitis: impact on mitochondrial S-adenosyl-L-methionine and glutathione. *Journal of Biological Chemistry*, *285*(24), 18528–18536.

Caldwell, S., Ikura, Y., Dias, D., Isomoto, K., Yabu, A., Moskaluk, C., … Rosenbaum, N. (2010). Hepatocellular ballooning in NASH. *Journal of Hepatology*, *53*(4), 719–723.

Caussy, C., Alquiraish, M. H., Nguyen, P., Hernandez, C., Cepin, S., Fortney, L. E., … Hooker, J. (2018). Optimal threshold of controlled attenuation parameter with MRI-PDFF as the gold standard for the detection of hepatic steatosis. *Hepatology*, *67*(4), 1348–1359.

Chalasani, N., Younossi, Z., Lavine, J. E., Diehl, A. M., Brunt, E. M., Cusi, K., … Sanyal, A. J. (2012). The diagnosis and management of non-alcoholic fatty liver disease: practice guideline by the American Gastroenterological Association, American Association for the Study of Liver Diseases, and American College of Gastroenterology. *Gastroenterology*, *142*(7), 1592–1609.

Chandarana, H., Do, R. K. G., Mussi, T. C., Jensen, J. H., Hajdu, C. H., Babb, J. S., & Taouli, B. (2012). The effect of liver iron deposition on hepatic apparent diffusion coefficient values in cirrhosis. *American Journal of Roentgenology*, *199*(4), 803–808.

Chandarana, H., & Taouli, B. (2010). Diffusion and perfusion imaging of the liver.

European Journal of Radiology, *76*(3), 348–358.

Chang, P. E., Goh, G. B.-B., Ngu, J. H., Tan, H. K., & Tan, C. K. (2016). Clinical applications, limitations and future role of transient elastography in the management of liver disease. *World Journal of Gastrointestinal Pharmacology and Therapeutics*, *7*(1), 91.

Cheemerla, S., & Balakrishnan, M. (2021). Global epidemiology of chronic liver disease. *Clinical Liver Disease*, *17*(5), 365.

Chen, S., Zhu, J., Zang, X., & Zhai, Y. (2021). The Emerging Role of Ferroptosis in Liver Diseases. *Frontiers in Cell and Developmental Biology*, *9*.

Chevallier, O., Zhou, N., Cercueil, J., He, J., Loffroy, R., & Wáng, Y. X. J. (2019). Comparison of tri-exponential decay versus bi-exponential decay and full fitting versus segmented fitting for modeling liver intravoxel incoherent motion diffusion MRI. *NMR in Biomedicine*, *32*(11), e4155.

Chowdhury, A. B., & Mehta, K. J. (2022). Liver biopsy for assessment of chronic liver diseases: a synopsis. *Clinical and Experimental Medicine*, 1–13.

Cohen, A. D., Schieke, M. C., Hohenwalter, M. D., & Schmainda, K. M. (2015). The effect of low b-values on the intravoxel incoherent motion derived pseudodiffusion parameter in liver. *Magnetic Resonance in Medicine*, *73*(1), 306–311.

Coupé, P., Manjón, J. V, Gedamu, E., Arnold, D., Robles, M., & Collins, D. L. (2010). Robust Rician noise estimation for MR images. *Medical Image Analysis*, *14*(4), 483–493.

Dancygier, H., & Schirmacher, P. (2010). Liver Cell Degeneration and Cell Death. In *Clinical Hepatology* (pp. 207–218). Springer.

de Boer, R. A., De Keulenaer, G., Bauersachs, J., Brutsaert, D., Cleland, J. G., Diez, J., … Lipson, K. E. (2019). Towards better definition, quantification and treatment of fibrosis in heart failure. A scientific roadmap by the Committee of Translational Research of the Heart Failure Association (HFA) of the European Society of Cardiology. *European Journal of Heart Failure*, *21*(3), 272–285.

Dominguez, M., Rincón, D., Abraldes, J. G., Miquel, R., Colmenero, J., Bellot, P., … Bañares, R. (2008). A new scoring system for prognostic stratification of patients

with alcoholic hepatitis. *Official Journal of the American College of Gastroenterology| ACG*, *103*(11), 2747–2756.

Einstein, A. (1905). Über die von der molekularkinetischen Theorie der Wärme geforderte Bewegung von in ruhenden Flüssigkeiten suspendierten Teilchen. *Annalen Der Physik*, *4*.

Elbanna, K. Y., Mansoori, B., Mileto, A., Rogalla, P., & S Guimarães, L. (2020). Dual-energy CT in diffuse liver disease: is there a role? *Abdominal Radiology*, *45*(11), 3413–3424.

Everhart, J. E., Wright, E. C., Goodman, Z. D., Dienstag, J. L., Hoefs, J. C., Kleiner, D. E., … Govindarajan, S. (2010). Prognostic value of Ishak fibrosis stage: findings from the hepatitis C antiviral long-term treatment against cirrhosis trial. *Hepatology*, *51*(2), 585–594.

Fedchuk, L., Nascimbeni, F., Pais, R., Charlotte, F., Housset, C., Ratziu, V., & Group, L. S. (2014). Performance and limitations of steatosis biomarkers in patients with nonalcoholic fatty liver disease. *Alimentary Pharmacology & Therapeutics*, *40*(10), 1209–1222.

Finkelstein, A., Cao, X., Liao, C., Schifitto, G., & Zhong, J. (2022). Diffusion Encoding Methods in MRI: Perspectives and Challenges. *Investigative Magnetic Resonance Imaging*, *26*(4), 208–219.

Forrest, E. H., Morris, A. J., Stewart, S., Phillips, M., Oo, Y. H., Fisher, N. C., … Day, C. P. (2007). The Glasgow alcoholic hepatitis score identifies patients who may benefit from corticosteroids. *Gut*, *56*(12), 1743–1746.

Fujima, N., Shimizu, Y., Yoshida, D., Kano, S., Mizumachi, T., Homma, A., … Kudo, K. (2019). Machine-learning-based prediction of treatment outcomes using MR imaging-derived quantitative tumor information in patients with sinonasal squamous cell carcinomas: a preliminary study. *Cancers*, *11*(6), 800.

Fujimoto, K., Noda, Y., Kawai, N., Kajita, K., Akamine, Y., Kawada, H., … Matsuo, M. (2021). Comparison of mono-exponential, bi-exponential, and stretched exponential diffusion-weighted MR imaging models in differentiating hepatic hemangiomas from liver metastases. *European Journal of Radiology*, *141*, 109806.

Furlan, A., Marin, D., Bae, K. T., Lagalla, R., Agnello, F., Bazzocchi, M., & Brancatelli, G. (2009). Focal liver lesions hyperintense on T1-weighted magnetic resonance images. *Seminars in Ultrasound, CT and MRI*, *30*(5), 436–449. Elsevier.

Gambarota, G., Hitti, E., Leporq, B., Saint-Jalmes, H., & Beuf, O. (2017). Eliminating the blood-flow confounding effect in intravoxel incoherent motion (IVIM) using the non-negative least square analysis in liver. *Magnetic Resonance in Medicine*, *77*(1), 310–317. https://doi.org/10.1002/mrm.26085

Gao, B., & Tsukamoto, H. (2016). Inflammation in alcoholic and nonalcoholic fatty liver disease: friend or foe? *Gastroenterology*, *150*(8), 1704–1709.

Garcia-Tsao, G., Bosch, J., Kayali, Z., Harrison, S. A., Abdelmalek, M. F., Lawitz, E., … Younes, Z. H. (2020). Randomized placebo-controlled trial of emricasan for non-alcoholic steatohepatitis-related cirrhosis with severe portal hypertension. *Journal of Hepatology*, *72*(5), 885–895.

Garteiser, P., Pagé, G., d'Assignies, G., Leitao, H. S., Vilgrain, V., Sinkus, R., & Van Beers, B. E. (2021). Necro-inflammatory activity grading in chronic viral hepatitis with three-dimensional multifrequency MR elastography. *Scientific Reports*, *11*(1), 19386.

Gaul, S., Leszczynska, A., Alegre, F., Kaufmann, B., Johnson, C. D., Adams, L. A., … Calvente, C. J. (2021). Hepatocyte pyroptosis and release of inflammasome particles induce stellate cell activation and liver fibrosis. *Journal of Hepatology*, *74*(1), 156–167.

Gautheron, J., Vucur, M., Reisinger, F., Cardenas, D. V., Roderburg, C., Koppe, C., … Neumann, U. P. (2014). A positive feedback loop between RIP 3 and JNK controls non-alcoholic steatohepatitis. *EMBO Molecular Medicine*, *6*(8), 1062–1074.

Germain, T., Favelier, S., Cercueil, J.-P., Denys, A., Krausé, D., & Guiu, B. (2014). Liver segmentation: practical tips. *Diagnostic and Interventional Imaging*, *95*(11), 1003–1016.

Gerstenmaier, J. F., & Gibson, R. N. (2014). Ultrasound in chronic liver disease. *Insights into Imaging*, *5*(4), 441–455.

Gilbert, R. (2009). *Physical biology of the cell, by Rob Phillips, Jane Kondev and Julie*

Theriot. Taylor & Francis.

Graupera, I., Thiele, M., Ma, A. T., Serra-Burriel, M., Pich, J., Fabrellas, N., … Reichert, M. (2022). LiverScreen project: study protocol for screening for liver fibrosis in the general population in European countries. *BMC Public Health*, *22*(1), 1–10.

Greaves, P. (2012). Female genital tract. *Histopathology of Preclinical Toxicity Studies. 4th Ed. Elsevier, Amsterdam*, 667–723.

Gressner, A. M. (1996). Transdifferentiation of hepatic stellate cells (Ito cells) to myofibroblasts: a key event in hepatic fibrogenesis. *Kidney International Supplement*, (54).

Grootjans, S., Vanden Berghe, T., & Vandenabeele, P. (2017). Initiation and execution mechanisms of necroptosis: an overview. *Cell Death & Differentiation*, *24*(7), 1184–1195.

Gu, J., Liu, S., Du, S., Zhang, Q., Xiao, J., Dong, Q., & Xin, Y. (2019). Diagnostic value of MRI-PDFF for hepatic steatosis in patients with non-alcoholic fatty liver disease: a meta-analysis. *European Radiology*, *29*, 3564–3573.

Guimaraes, A. R., Siqueira, L., Uppal, R., Alford, J., Fuchs, B. C., Yamada, S., … Chew, M. L. (2016). T2 relaxation time is related to liver fibrosis severity. *Quantitative Imaging in Medicine and Surgery*, *6*(2), 103.

Gustafsson, O., Montelius, M., Starck, G., & Ljungberg, M. (2018). Impact of prior distributions and central tendency measures on Bayesian intravoxel incoherent motion model fitting. *Magnetic Resonance in Medicine*, *79*(3), 1674–1683. https://doi.org/10.1002/mrm.26783

Hammoud, D. A. (2016). Molecular Imaging of Inflammation: Current Status. *Journal of Nuclear Medicine : Official Publication, Society of Nuclear Medicine*, *57*(8), 1161–1165. https://doi.org/10.2967/jnumed.115.161182

Hanahan, D., & Weinberg, R. A. (2011). Hallmarks of cancer: the next generation. *Cell*, *144*(5), 646–674.

Harrison, S. A., Goodman, Z., Jabbar, A., Vemulapalli, R., Younes, Z. H., Freilich, B., … Zivony, A. (2020). A randomized, placebo-controlled trial of emricasan in patients with NASH and F1-F3 fibrosis. *Journal of Hepatology*, *72*(5), 816–827.

Harrison, S. A., Oliver, D., Arnold, H. L., Gogia, S., & Neuschwander-Tetri, B. A. (2008).

Development and validation of a simple NAFLD clinical scoring system for identifying patients without advanced disease. *Gut*, *57*(10), 1441–1447.

Heris, H. K., Nejati, B., Rezazadeh, K., Sate, H., Dolatkhah, R., Ghoreishi, Z., & Esfahani, A. (2021). Evaluation of iron overload by cardiac and liver T2* in β-thalassemia: Correlation with serum ferritin, heart function and liver enzymes. *Journal of Cardiovascular and Thoracic Research*, *13*(1), 54.

Hirooka, M., Koizumi, Y., Sunago, K., Nakamura, Y., Hirooka, K., Watanabe, T., … Hiasa, Y. (2022). Efficacy of B-mode ultrasound-based attenuation for the diagnosis of hepatic steatosis: a systematic review/meta-analysis. *Journal of Medical Ultrasonics*, *49*(2), 199–210.

Hoffman, D. H., Ayoola, A., Nickel, D., Han, F., Chandarana, H., & Shanbhogue, K. P. (2020). T1 mapping, T2 mapping and MR elastography of the liver for detection and staging of liver fibrosis. *Abdominal Radiology*, *45*, 692–700.

Huang, J., Leporq, B., Hervieu, V., Dumortier, J., Beuf, O., & Ratiney, H. (2023). Diffusion-Weighted MRI of the Liver in Patients With Chronic Liver Disease: A Comparative Study Between Different Fitting Approaches and Diffusion Models. *Journal of Magnetic Resonance Imaging*.

Ibrahim, M., Singh, C., Ganie, M. A., & Alsayari, K. (2009). NASH: the hepatic injury of metabolic syndrome: a brief update. *International Journal of Health Sciences*, *3*(2), 265.

Jalnefjord, O., Andersson, M., Montelius, M., Starck, G., Elf, A.-K., Johanson, V., … Ljungberg, M. (2018). Comparison of methods for estimation of the intravoxel incoherent motion (IVIM) diffusion coefficient (D) and perfusion fraction (f). *Magnetic Resonance Materials in Physics, Biology and Medicine*, *31*(6), 715–723.

Jensen, J. H., Helpern, J. A., Ramani, A., Lu, H., & Kaczynski, K. (2005). Diffusional kurtosis imaging: the quantification of non-gaussian water diffusion by means of magnetic resonance imaging. *Magnetic Resonance in Medicine: An Official Journal of the International Society for Magnetic Resonance in Medicine*, *53*(6), 1432–1440.

Kim, J., Yoon, H., Lee, M.-J., Kim, M.-J., Han, K., Han, S. J., … Shin, H. J. (2019). Clinical

utility of mono-exponential model diffusion weighted imaging using two b-values compared to the bi-or stretched exponential model for the diagnosis of biliary atresia in infant liver MRI. *PloS One*, *14*(12), e0226627.

King, G. S. (2002). Handbook of Toxicologic Pathology. *Archives of Pathology & Laboratory Medicine*, *126*(9), 1138–1140.

Kowdley, K. V. (2016). Iron overload in patients with chronic liver disease. *Gastroenterology & Hepatology*, *12*(11), 695.

Laroia, S. T., Yadav, K., Kumar, S., Rastogi, A., Kumar, G., & Sarin, S. K. (2021). Material decomposition using iodine quantification on spectral CT for characterising nodules in the cirrhotic liver: a retrospective study. *European Radiology Experimental*, *5*(1), 1–13.

Le Bihan, D. (1988). Intravoxel incoherent motion imaging using steady-state free precession. *Magnetic Resonance in Medicine*, *7*(3), 346–351.

Le Bihan, D. (2019). What can we see with IVIM MRI? *Neuroimage*, *187*, 56–67.

Le Bihan, D., Breton, E., Lallemand, D., Grenier, P., Cabanis, E., & Laval-Jeantet, M. (1986). MR imaging of intravoxel incoherent motions: application to diffusion and perfusion in neurologic disorders. *Radiology*, *161*(2), 401–407.

Lee, J.-H., Kim, D., Kim, H. J., Lee, C.-H., Yang, J. I., Kim, W., … Sung, M.-W. (2010). Hepatic steatosis index: a simple screening tool reflecting nonalcoholic fatty liver disease. *Digestive and Liver Disease*, *42*(7), 503–508.

Lefebvre, T., Hébert, M., Bilodeau, L., Sebastiani, G., Cerny, M., Olivié, D., … Nguyen, B. N. (2021). Intravoxel incoherent motion diffusion-weighted MRI for the characterization of inflammation in chronic liver disease. *European Radiology*, *31*(3), 1347–1358.

Leitão, H. S., Doblas, S., d'Assignies, G., Garteiser, P., Daire, J.-L., Paradis, V., … Van Beers, B. E. (2013). Fat deposition decreases diffusion parameters at MRI: a study in phantoms and patients with liver steatosis. *European Radiology*, *23*(2), 461–467.

Leporq, B., Lambert, S. A., Ronot, M., Vilgrain, V., & Van Beers, B. E. (2017). Simultaneous MR quantification of hepatic fat content, fatty acid composition, transverse relaxation time and magnetic susceptibility for the diagnosis of non-

alcoholic steatohepatitis. *NMR in Biomedicine*, *30*(10), 1–8. https://doi.org/10.1002/nbm.3766

Leporq, Benjamin, Ratiney, H., Pilleul, F., & Beuf, O. (2013). Liver fat volume fraction quantification with fat and water T 1 and T 2* estimation and accounting for NMR multiple components in patients with chronic liver disease at 1.5 and 3.0 T. *European Radiology*, *23*, 2175–2186.

Leporq, Benjamin, Saint‐Jalmes, H., Rabrait, C., Pilleul, F., Guillaud, O., Dumortier, J., ⋯ Beuf, O. (2015). Optimization of intra-voxel incoherent motion imaging at 3.0 Tesla for fast liver examination. *Journal of Magnetic Resonance Imaging*, *41*(5), 1209–1217.

Lewis, S., Dyvorne, H., Cui, Y., & Taouli, B. (2014). Diffusion-weighted imaging of the liver: techniques and applications. *Magnetic Resonance Imaging Clinics*, *22*(3), 373–395.

Li, Q., Dhyani, M., Grajo, J. R., Sirlin, C., & Samir, A. E. (2018). Current status of imaging in nonalcoholic fatty liver disease. *World Journal of Hepatology*, *10*(8), 530.

Li, T., Che-Nordin, N., Wáng, Y. X. J., Rong, P.-F., Qiu, S.-W., Zhang, S.-W., … Zhao, F. (2019). Intravoxel incoherent motion derived liver perfusion/diffusion readouts can be reliable biomarker for the detection of viral hepatitis B induced liver fibrosis. *Quantitative Imaging in Medicine and Surgery*, *9*(3), 371.

Li, Y. T., Cercueil, J.-P., Yuan, J., Chen, W., Loffroy, R., & Wáng, Y. X. J. (2017). Liver intravoxel incoherent motion (IVIM) magnetic resonance imaging: a comprehensive review of published data on normal values and applications for fibrosis and tumor evaluation. *Quantitative Imaging in Medicine and Surgery*, *7*(1), 59.

Liang, J., Song, X., Xiao, Z., Chen, H., Shi, C., & Luo, L. (2018). Using IVIM-MRI and R2∗ Mapping to Differentiate Early Stage Liver Fibrosis in a Rat Model of Radiation-Induced Liver Fibrosis. *BioMed Research International*, *2018*.

Liu, J., Gambarota, G., Shu, H., Jiang, L., Leporq, B., Beuf, O., & Karfoul, A. (2020). On the identification of the blood vessel confounding effect in intravoxel incoherent motion (IVIM) Diffusion-Weighted (DW)-MRI in liver: An efficient

sparsity based algorithm. *Medical Image Analysis*, *61*, 101637.

Lo, R. C., & Kim, H. (2017). Histopathological evaluation of liver fibrosis and cirrhosis regression. *Clinical and Molecular Hepatology*, *23*(4), 302.

Lok, A. S., Seeff, L. B., Morgan, T. R., Di Bisceglie, A. M., Sterling, R. K., Curto, T. M., … Bonkovsky, H. L. (2009). Incidence of hepatocellular carcinoma and associated risk factors in hepatitis C-related advanced liver disease. *Gastroenterology*, *136*(1), 138–148.

Lu, P.-X., Huang, H., Yuan, J., Zhao, F., Chen, Z.-Y., Zhang, Q., … Wáng, Y.-X. J. (2014). Decreases in molecular diffusion, perfusion fraction and perfusion-related diffusion in fibrotic livers: a prospective clinical intravoxel incoherent motion MR imaging study. *PLoS One*, *9*(12), e113846.

Lu, X., Zhou, H., Wang, K., Jin, J., Meng, F., Mu, X., … Tian, J. (2021). Comparing radiomics models with different inputs for accurate diagnosis of significant fibrosis in chronic liver disease. *European Radiology*, *31*, 8743–8754.

Luciani, A., Vignaud, A., Cavet, M., Tran Van Nhieu, J., Mallat, A., Ruel, L., … Rahmouni, A. (2008). Liver cirrhosis: intravoxel incoherent motion MR imaging—pilot study. *Radiology*, *249*(3), 891–899.

Lv, P., Lin, X., Gao, J., & Chen, K. (2012). Spectral CT: preliminary studies in the liver cirrhosis. *Korean Journal of Radiology*, *13*(4), 434–442.

Makhija, N., Vikram, N. K., Srivastava, D. N., & Madhusudhan, K. S. (2021). Role of Diffusion-Weighted Magnetic Resonance Imaging in the Diagnosis and Grading of Hepatic Steatosis in Patients With Non-alcoholic Fatty Liver Disease: Comparison With Ultrasonography and Magnetic Resonance Spectroscopy. *Journal of Clinical and Experimental Hepatology*, *11*(6), 654–660.

Manduca, A., Bayly, P. V, Ehman, R. L., Kolipaka, A., Royston, T. J., Sack, I., … Van Beers, B. E. (2021). MR elastography: Principles, guidelines, and terminology. *Magnetic Resonance in Medicine*, *85*(5), 2377–2390.

Matos, A. P., Velloni, F., Ramalho, M., AlObaidy, M., Rajapaksha, A., & Semelka, R. C. (2015). Focal liver lesions: Practical magnetic resonance imaging approach. *World Journal of Hepatology*, *7*(16), 1987.

Meeus, E. M., Novak, J., Withey, S. B., Zarinabad, N., Dehghani, H., & Peet, A. C.

(2017). Evaluation of intravoxel incoherent motion fitting methods in low-perfused tissue. *Journal of Magnetic Resonance Imaging*, *45*(5), 1325–1334.

Mendler, M.-H., Bouillet, P., Le Sidaner, A., Lavoine, E., Labrousse, F., Sautereau, D., & Pillegand, B. (1998). Dual-energy CT in the diagnosis and quantification of fatty liver: limited clinical value in comparison to ultrasound scan and single-energy CT, with special reference to iron overload. *Journal of Hepatology*, *28*(5), 785–794.

Mesropyan, N., Kupczyk, P., Dold, L., Weismüller, T. J., Sprinkart, A. M., Mädler, B., … Attenberger, U. (2021). Non-invasive assessment of liver fibrosis in autoimmune hepatitis: Diagnostic value of liver magnetic resonance parametric mapping including extracellular volume fraction. *Abdominal Radiology*, *46*, 2458–2466.

Montaño-Loza, A. J. (2022). Evaluation of fibrosis in patients with nonalcoholic fatty liver disease. *Revista de Gastroenterologia de Mexico (English)*, Vol. 87, pp. 1–3.

Morozov, S., Sergunova, K., Petraikin, A., Akhmad, E., Kivasev, S., Semenov, D., … Morozov, A. (2020). Diffusion processes modeling in magnetic resonance imaging. *Insights into Imaging*, *11*(1), 1–9.

Moura Cunha, G., Navin, P. J., Fowler, K. J., Venkatesh, S. K., Ehman, R. L., & Sirlin, C. B. (2021). Quantitative magnetic resonance imaging for chronic liver disease. *The British Journal of Radiology*, *94*(1121), 20201377.

Nalbantoglu, Ilk., & Brunt, E. M. (2014). Role of liver biopsy in nonalcoholic fatty liver disease. *World Journal of Gastroenterology: WJG*, *20*(27), 9026.

Narayanan, A. S., Engel, L. D., & Page, R. C. (1983). The effect of chronic inflammation on the composition of collagen types in human connective tissue. *Collagen and Related Research*, *3*(4), 323–334.

Nassir, F., Rector, R. S., Hammoud, G. M., & Ibdah, J. A. (2015). Pathogenesis and prevention of hepatic steatosis. *Gastroenterology & Hepatology*, *11*(3), 167.

Neuberger, J., Patel, J., Caldwell, H., Davies, S., Hebditch, V., Hollywood, C., … Roslund, N. (2020). Guidelines on the use of liver biopsy in clinical practice from the British Society of Gastroenterology, the Royal College of Radiologists and the Royal College of Pathology. *Gut*, *69*(8), 1382–1403.

Oeda, S., Takahashi, H., Imajo, K., Seko, Y., Ogawa, Y., Moriguchi, M., … Kage, M.

(2020). Accuracy of liver stiffness measurement and controlled attenuation parameter using FibroScan® M/XL probes to diagnose liver fibrosis and steatosis in patients with nonalcoholic fatty liver disease: a multicenter prospective study. *Journal of Gastroenterology*, *55*, 428–440.

Paradis, V., & Beaufrère, A. (2022). Regenerative Nodules and Liver Tumors in Vascular Liver Diseases. In *Vascular Disorders of the Liver* (pp. 215–236). Springer.

Park, J. H., Seo, N., Chung, Y. E., Kim, S. U., Park, Y. N., Choi, J.-Y., … Kim, M.-J. (2021). Noninvasive evaluation of liver fibrosis: comparison of the stretched exponential diffusion-weighted model to other diffusion-weighted MRI models and transient elastography. *European Radiology*, *31*(7), 4813–4823.

Peng, J.-K., Hepgul, N., Higginson, I. J., & Gao, W. (2019). Symptom prevalence and quality of life of patients with end-stage liver disease: a systematic review and meta-analysis. *Palliative Medicine*, *33*(1), 24–36.

Perisetti, A., Goyal, H., Yendala, R., Thandassery, R. B., & Giorgakis, E. (2021). Non-cirrhotic hepatocellular carcinoma in chronic viral hepatitis: Current insights and advancements. *World Journal of Gastroenterology*, *27*(24), 3466.

Piscaglia, F., Marinelli, S., Bota, S., Serra, C., Venerandi, L., Leoni, S., & Salvatore, V. (2014). The role of ultrasound elastographic techniques in chronic liver disease: current status and future perspectives. *European Journal of Radiology*, *83*(3), 450–455.

Positano, V., Salani, B., Pepe, A., Santarelli, M. F., De Marchi, D., Ramazzotti, A., … Cianciulli, P. (2009). Improved T2* assessment in liver iron overload by magnetic resonance imaging. *Magnetic Resonance Imaging*, *27*(2), 188–197.

Poynard, T., Peta, V., Munteanu, M., Charlotte, F., Ngo, Y., Ngo, A., … Mathurin, P. (2019). The diagnostic performance of a simplified blood test (SteatoTest-2) for the prediction of liver steatosis. *European Journal of Gastroenterology & Hepatology*, *31*(3), 393.

Poynard, T., Ratziu, V., Naveau, S., Thabut, D., Charlotte, F., Messous, D., … Ngo, Y. (2005). The diagnostic value of biomarkers (SteatoTest) for the prediction of liver steatosis. *Comparative Hepatology*, *4*(1), 1–14.

Rodrigues, S. G., Montani, M., Guixé-Muntet, S., De Gottardi, A., Berzigotti, A., & Bosch, J. (2019). Patients with signs of advanced liver disease and clinically significant portal hypertension do not necessarily have cirrhosis. *Clinical Gastroenterology and Hepatology*, *17*(10), 2101–2109.

Roehlen, N., Crouchet, E., & Baumert, T. F. (2020). Liver fibrosis: mechanistic concepts and therapeutic perspectives. *Cells*, *9*(4), 875.

Ros, P. R. (2018). Imaging of diffuse and inflammatory liver disease. *Diseases of the Abdomen and Pelvis 2018-2021: Diagnostic Imaging-IDKD Book*, *ch. 22*, 237–246.

Ruffillo, G., Fassio, E., Alvarez, E., Landeira, G., Longo, C., Domínguez, N., & Gualano, G. (2011). Comparison of NAFLD fibrosis score and BARD score in predicting fibrosis in nonalcoholic fatty liver disease. *Journal of Hepatology*, *54*(1), 160–163.

Salkic, N. N., Jovanovic, P., Hauser, G., & Brcic, M. (2014). FibroTest/Fibrosure for significant liver fibrosis and cirrhosis in chronic hepatitis B: a meta-analysis. *Official Journal of the American College of Gastroenterology| ACG*, *109*(6), 796–809.

Sandrasegaran, K., Territo, P., Elkady, R. M., Lin, Y., Gasparis, P., Borthakur, G., & Lin, C. (2018). Does intravoxel incoherent motion reliably stage hepatic fibrosis, steatosis, and inflammation? *Abdominal Radiology*, *43*(3), 600–606.

Satapathy, S. K., & Sanyal, A. J. (2015). Epidemiology and natural history of nonalcoholic fatty liver disease. *Seminars in Liver Disease*, *35*(03), 221–235. Thieme Medical Publishers.

Schlageter, M., Terracciano, L. M., D'Angelo, S., & Sorrentino, P. (2014). Histopathology of hepatocellular carcinoma. *World Journal of Gastroenterology: WJG*, *20*(43), 15955.

Schuppan, D., & Afdhal, N. H. (2008). Liver cirrhosis. *The Lancet*, *371*(9615), 838–851.

Schwabe, R. F., & Luedde, T. (2018). Apoptosis and necroptosis in the liver: a matter of life and death. *Nature Reviews Gastroenterology & Hepatology*, *15*(12), 738–752.

Seo, N., Chung, Y. E., Park, Y. N., Kim, E., Hwang, J., & Kim, M.-J. (2018). Liver fibrosis:

stretched exponential model outperforms mono-exponential and bi-exponential models of diffusion-weighted MRI. *European Radiology*, *28*(7), 2812–2822.

Sharma, A., & Nagalli, S. (2022). Chronic liver disease. In *StatPearls [Internet]*. StatPearls Publishing.

Shendge, A. K., Panja, S., Basu, T., Ghate, N. B., & Mandal, N. (2021). Ameliorating effects of white mulberry on iron-overload-induced oxidative stress and liver fibrosis in Swiss albino mice. *Food and Chemical Toxicology*, *156*, 112520.

Shin, M. K., Song, J. S., Hwang, S. B., Hwang, H. P., Kim, Y. J., & Moon, W. S. (2019). Liver fibrosis assessment with diffusion-weighted imaging: value of liver apparent diffusion coefficient normalization using the spleen as a reference organ. *Diagnostics*, *9*(3), 107.

Shojaie, L., Iorga, A., & Dara, L. (2020). Cell death in liver diseases: a review. *International Journal of Molecular Sciences*, *21*(24), 9682.

Sigmund, E. E., Cho, G. Y., Kim, S., Finn, M., Moccaldi, M., Jensen, J. H., … Moy, L. (2011). Intravoxel incoherent motion imaging of tumor microenvironment in locally advanced breast cancer. *Magnetic Resonance in Medicine*, *65*(5), 1437–1447.

Sofue, K., Onoda, M., Tsurusaki, M., Morimoto, D., Yada, N., Kudo, M., & Murakami, T. (2020). Dual-frequency MR elastography to differentiate between inflammation and fibrosis of the liver: Comparison with histopathology. *Journal of Magnetic Resonance Imaging*, *51*(4), 1053–1064.

Song, J., Yu, X., Song, W., Guo, D., Li, C., Liu, H., … Liu, Y. (2020). MRI-Based Radiomics Models Developed With Features of the Whole Liver and Right Liver Lobe: Assessment of Hepatic Inflammatory Activity in Chronic Hepatic Disease. *Journal of Magnetic Resonance Imaging*, *52*(6), 1668–1678.

Soto-Gutierrez, A., Gough, A., Vernetti, L. A., Taylor, D. L., & Monga, S. P. (2017). Pre-clinical and clinical investigations of metabolic zonation in liver diseases: the potential of microphysiology systems. *Experimental Biology and Medicine*, *242*(16), 1605–1616.

Springer, F., Machann, J., Claussen, C. D., Schick, F., & Schwenzer, N. F. (2010). Liver

fat content determined by magnetic resonance imaging and spectroscopy. *World Journal of Gastroenterology: WJG*, *16*(13), 1560.

Starley, B. Q., Calcagno, C. J., & Harrison, S. A. (2010). Nonalcoholic fatty liver disease and hepatocellular carcinoma: a weighty connection. *Hepatology*, *51*(5), 1820–1832.

Stejskal, E. O., & Tanner, J. E. (1965). Spin diffusion measurements: spin echoes in the presence of a time-dependent field gradient. *The Journal of Chemical Physics*, *42*(1), 288–292.

Sterling, R. K., Lissen, E., Clumeck, N., Sola, R., Correa, M. C., Montaner, J., … Thomas, D. L. (2006). Development of a simple noninvasive index to predict significant fibrosis in patients with HIV/HCV coinfection. *Hepatology*, *43*(6), 1317–1325.

Stokes, G. G. (1851). *On the effect of the internal friction of fluids on the motion of pendulums*.

Sutherland, T., Watts, J., Ryan, M., Galvin, A., Temple, F., Vuong, J., & Little, A. F. (2017). Diffusion-weighted MRI for hepatocellular carcinoma screening in chronic liver disease: direct comparison with ultrasound screening. *Journal of Medical Imaging and Radiation Oncology*, *61*(1), 34–39.

Tang, A. N., Tan, J., Sun, M., Hamilton, G., Bydder, M., Wolfson, T., … Loomba, R. (2013). Nonalcoholic fatty liver disease: MR imaging of liver proton density fat fraction to assess hepatic steatosis. *Radiology*, *267*(2), 422.

Taouli, B., Chouli, M., Martin, A. J., Qayyum, A., Coakley, F. V, & Vilgrain, V. (2008). Chronic hepatitis: role of diffusion-weighted imaging and diffusion tensor imaging for the diagnosis of liver fibrosis and inflammation. *Journal of Magnetic Resonance Imaging: An Official Journal of the International Society for Magnetic Resonance in Medicine*, *28*(1), 89–95.

Taouli, B., Ehman, R. L., & Reeder, S. B. (2009). Advanced MRI methods for assessment of chronic liver disease. *AJR. American Journal of Roentgenology*, *193*(1), 14.

Taouli, B., Tolia, A. J., Losada, M., Babb, J. S., Chan, E. S., Bannan, M. A., & Tobias, H. (2007). Diffusion-weighted MRI for quantification of liver fibrosis: preliminary experience. *American Journal of Roentgenology*, *189*(4), 799–806.

Thomaides-Brears, H. B., Alkhouri, N., Allende, D., Harisinghani, M., Noureddin, M., Reau, N. S., … Cryer, D. R. H. (2022). Incidence of complications from percutaneous biopsy in chronic liver disease: a systematic review and meta-analysis. *Digestive Diseases and Sciences*, *67*(7), 3366–3394.

Tilg, H, & Kaser, A. (2005). Predicting mortality by the Glasgow alcoholic hepatitis score: the long awaited progress? *Gut*, *54*(8), 1057–1059.

Tilg, Herbert, & Moschen, A. R. (2010). Evolution of inflammation in nonalcoholic fatty liver disease: the multiple parallel hits hypothesis. *Hepatology*, *52*(5), 1836–1846.

Torrey, H. C. (1956). Bloch equations with diffusion terms. *Physical Review*, *104*(3), 563.

Van Griethuysen, J. J. M., Fedorov, A., Parmar, C., Hosny, A., Aucoin, N., Narayan, V., … Aerts, H. J. W. L. (2017). Computational radiomics system to decode the radiographic phenotype. *Cancer Research*, *77*(21), e104–e107.

Vernuccio, F., Cannella, R., Bartolotta, T. V., Galia, M., Tang, A., & Brancatelli, G. (2021). Advances in liver US, CT, and MRI: moving toward the future. *European Radiology Experimental*, *5*(1), 1–16.

Wang, X., Song, J., Zhou, S., Lu, Y., Lin, W., Koh, T. S., … Yan, Z. (2021). A comparative study of methods for determining Intravoxel incoherent motion parameters in cervix cancer. *Cancer Imaging*, *21*(1), 1–11.

Wang, Y. X. J., Huang, H., Zheng, C.-J., Xiao, B.-H., Chevallier, O., & Wang, W. (2021). Diffusion-weighted MRI of the liver: challenges and some solutions for the quantification of apparent diffusion coefficient and intravoxel incoherent motion. *American Journal of Nuclear Medicine and Molecular Imaging*, *11*(2), 107.

While, P. T. (2017). A comparative simulation study of bayesian fitting approaches to intravoxel incoherent motion modeling in diffusion-weighted MRI. *Magnetic Resonance in Medicine*, *78*(6), 2373–2387.

Witek, R. P., Stone, W. C., Karaca, F. G., Syn, W., Pereira, T. A., Agboola, K. M., … Choi, S. S. (2009). Pan-caspase inhibitor VX-166 reduces fibrosis in an animal model of nonalcoholic steatohepatitis. *Hepatology*, *50*(5), 1421–1430.

Wu, W.-C., Yang, S.-C., Chen, Y.-F., Tseng, H.-M., & My, P.-C. (2017). Simultaneous assessment of cerebral blood volume and diffusion heterogeneity using hybrid IVIM and DK MR imaging: initial experience with brain tumors. *European Radiology*, *27*(1), 306–314.

Yablonskiy, D. A., Bretthorst, G. L., & Ackerman, J. J. H. (2003a). Statistical model for diffusion attenuated MR signal. *Magnetic Resonance in Medicine: An Official Journal of the International Society for Magnetic Resonance in Medicine*, *50*(4), 664–669.

Yang, L., Rao, S., Wang, W., Chen, C., Ding, Y., Yang, C., … Zeng, M. (2018). Staging liver fibrosis with DWI: is there an added value for diffusion kurtosis imaging? *European Radiology*, *28*(7), 3041–3049.

Ye, J., Wu, Y., Li, F., Wu, T., Shao, C., Lin, Y., … Zhong, B. (2019). Effect of orlistat on liver fat content in patients with nonalcoholic fatty liver disease with obesity: assessment using magnetic resonance imaging-derived proton density fat fraction. *Therapeutic Advances in Gastroenterology*, *12*, 1756284819879047.

Yeh, B. M., FitzGerald, P. F., Edic, P. M., Lambert, J. W., Colborn, R. E., Marino, M. E., … Wong, M. J. (2017). Opportunities for new CT contrast agents to maximize the diagnostic potential of emerging spectral CT technologies. *Advanced Drug Delivery Reviews*, *113*, 201–222.

Yin, Z., Murphy, M. C., Li, J., Glaser, K. J., Mauer, A. S., Mounajjed, T., … Manduca, A. (2019). Prediction of nonalcoholic fatty liver disease (NAFLD) activity score (NAS) with multiparametric hepatic magnetic resonance imaging and elastography. *European Radiology*, *29*, 5823–5831.

Yoshikawa, M., Kudo, K., Harada, T., Harashima, K., Suzuki, J., Ogawa, K., … Shirai, T. (2021). Quantitative Susceptibility Mapping versus R2*-based Histogram Analysis for Evaluating Liver Fibrosis: Preliminary Results. *Magnetic Resonance in Medical Sciences*, mp-2020.

Yoshimaru, D., Takatsu, Y., Suzuki, Y., Miyati, T., Hamada, Y., Funaki, A., … Tobari, M. (2019). Diffusion kurtosis imaging in the assessment of liver function: Its potential as an effective predictor of liver function. *The British Journal of Radiology*, *92*(1094), 20170608.

Yu, J., & Wang, J. (2021). Research mechanisms of and pharmaceutical treatments for ferroptosis in liver diseases. *Biochimie*, *180*, 149–157.

Zhang, Y. N., Fowler, K. J., Boehringer, A. S., Montes, V., Schlein, A. N., Covarrubias, Y., … Andre, M. P. (2022). Comparative diagnostic performance of ultrasound shear wave elastography and magnetic resonance elastography for classifying fibrosis stage in adults with biopsy-proven nonalcoholic fatty liver disease. *European Radiology*, 1–13.

Zhao, X., Yang, L., Chang, N., Hou, L., Zhou, X., Yang, L., & Li, L. (2020). Neutrophils undergo switch of apoptosis to NETosis during murine fatty liver injury via S1P receptor 2 signaling. *Cell Death & Disease*, *11*(5), 1–14.

Zhou, Y., Zhang, H.-X., Zhang, X.-S., Sun, Y.-F., He, K.-B., Sang, X.-Q., … Kuai, Z.-X. (2019a). Non-mono-exponential diffusion models for assessing early response of liver metastases to chemotherapy in colorectal Cancer. *Cancer Imaging*, *19*(1), 1–11.

FOLIO ADMINISTRATIF

THESE DE L'INSA LYON, MEMBRE DE L'UNIVERSITE DE LYON

NOM : HUANG
(avec précision du nom de jeune fille, le cas échéant)

DATE de SOUTENANCE : 24/10/2023

Prénoms : Jiqing

TITRE : Virtual liver biopsy for Chronic liver disease monitoring by using mpMRI-based radiomic

NATURE : Doctorat

Numéro d'ordre : 2023ISAL0078

Ecole doctorale : EDISS

Spécialité :Ingénierie biomédicale

RESUME : Chronic liver disease (CLD) represents a broad spectrum of diseases involving different etiologies. These diseases are characterized by histological features such as inflammation, fibrosis, steatosis, ballooning, or iron overload. Among them, inflammation plays a critical role in the early liver fibrosis process, and fibrosis affects the CLD prognosis and treatment strategy. Although liver biopsy is the gold standard for the diagnosis of CLD, Its invasiveness limits its clinical use. Therefore, an alternative noninvasive, sensitive, and specific remains an unmet medical need.
Magnetic resonance imaging (MRI), especially with diffusion-weighted imaging (DWI) appears currently as an interesting imaging technique to detect CLD-related features. The objective of this thesis is to develop the concept of virtual biopsy to grade inflammation and fibrosis in CLD. To achieve this, the thesis is divided into two parts.
Firstly, using IVIM single sequence study, we studied the standard and advanced DWI's parameters with different fitting approaches and diffusion models, and then the relationship between CLD-related features and DWI parameters were investigated. Significant differences were found between the groups with different degrees of fibrosis. The top four significant differences parameters were selected to build classifiers to characterize fibrosis.
Secondly, from multiple MRI sequences, a radiomics approach involving extraction of several feature combinations from conventional T1w or T2w images as well as proton density fat fraction, T2* and diffusion parameter maps was investigated. The best combinations were then searched to classify inflammation and fibrosis using random forest.
This study validated the utilization of multiparametric MRI for fibrosis and inflammation severity grading and proposed two effective classifiers for them.

MOTS-CLÉS : Chronic liver disease, Diffusion-weighted Image, Machine Learning, Magnetic Resonance Imaging, Radiomics

Laboratoire (s) de recherche : CREATIS

Directeur de thèse: Olivier BEUF

Président de jury : Denis FRIBOULET

Composition du jury :
Olivier BEUF, Hélène RATINEY, Benjamin LEPORQ, Lihui WANG, Johanne BEZY-WENDLING, Jean-Marie BONNY, Antoine VACAVANT, Denis FRIBOULET